Large Wood Dynamics in Sharp River Bends: Experimental and Numerical Investigations

Dissertation

submitted to and approved by the

Faculty of Architecture, Civil Engineering and Environmental Sciences
Technische Universität Braunschweig

and the

Department of Civil and Environmental Engineering
University of Florence

in candidacy for the degree of a
Doktor-Ingenieur (Dr.-Ing.) /
Dottore di Ricerca Civil and Environmental Engineering *)

by
Lorenzo Innocenti
born 11th July 1990
from Firenze, Italy

Submitted on	09 September 2021
Oral examination on	28 October 2021
Professorial advisors	Prof. Dr.-Ing. Jochen Aberle
	Prof. Dr.-Ing. Luca Solari

2022

*) Either the German or the Italian form of the title may be used.

Abstract

In last decades, the role of large wood (LW) in rivers was largely investigated due to the ecological importance for river habitats, and due to the associated potential hazards to humans and infrastructures, resulting an additional component of fluvial hydraulics. Despite recent research, knowledge of the dynamics of transported wood elements is still incomplete, particularly in modelling the effect of secondary currents on the LW dynamics.

The present PhD research aims to enhance the knowledge on the transport of LW in sharp river bends by finding answers to the two main research questions: the identification of the main variables that influence the phenomenon, and assessing the capability of 2D depth-averaged models in reproducing effects of secondary currents on wood trajectories. A combined physical and numerical approach is used for this purpose.

Physical model tests were performed in order to investigate the influence of (i) LW element dimensions, (ii) the approaching position of LW to the curve, and (iii) the initial orientation of LW, on the wood trajectories in a sharp bend. The analysis of experiments was conducted by considering the trajectories of wood pieces along the bend and providing statistical results. Moreover, experiments were analyzed by applying a mathematical model in order to provide the drag coefficient for floating LW subjected to a helical flow. For the simulation of secondary current effects, the 2D depth-averaged model "Iber-Wood" was enhanced and tested by simulating two experimental setups and a river-scale case study.

The main results of the present work include the individuation of the main variables that influenced the LW trajectories in sharp river bends, the calculation of drag coefficients for a floating LW, and the improvement of the Iber-Wood model in simulating secondary current effects. In addition, two nondimensional coefficients are provided: the coefficient of variation for expressing the trajectory deviation along a bend, and the coefficient of similarity for expressing the similarity between two trajectories.

Laboratory experiments particularly highlighted the influence of the wood length which is the main variable determining the trajectory of single wood pieces. Moreover, the approaching position of LW to the curve determined the impact of the wood against the outer bank towards which the wood pieces are pushed by the secondary current. The mathematical model defined for calculating the drag coefficient provides values ranging between 0.3 and 1.2 dependent on the orientation of the wood pieces with respect to the flow direction. Finally, the enhanced Iber-Wood model allowed to simulate the drift to which LW is subjected while transported along a river bend due to the presence of the helical flow.

Acknowledgments

The present PhD research has been conducted thanks to a PhD scholarship given by the Regione Toscana (Italy) which is greatly acknowledged. Moreover, I would thank the Erasmus project for providing founds during my stay abroad in Europe.

My gratitude goes firstly to my supervisors for their guidance and support during the research activities. The Prof. Luca Solari allowed me to carry out the PhD research at the Department of Civil and Environmental Engineering (DICeA) of the University of Florence, Italy. The Prof. Jochen Aberle accepted me as a PhD student at the Leichtweiß Institute for Hydraulic Engineering and Water Resources (LWI) of the Technical University of Braunschweig, Germany.

A special thank goes to Dr. Virginia Ruiz-Villanueva for sharing her knowledge and experience with me, and for introducing me at the Flumen Institute of the Polytechnic University of Barcelona (UPC), Spain, where the Prof. Ernest Bladé accepted me as a visiting PhD student.

My sincere thanks to Marcos Sanz-Ramos for helping me a lot in working with Iber during my stay in Barcelona and for being available every time I need his suggestions.

I wish to thank all the people met in these three years of research, the entire staff and colleagues of the DICeA with which I spent a lot of time in the office, the people of the LWI who welcomed me in Braunschweig, and the guys of the Flumen Institute.

Finally, I would like to thank my partner, my family, and my sincere friends.

Contents

List of Figures

List of Tables

List of Symbols

A_f	projected area in the direction of motion	m^2
A_{obs}	observed area for the coefficient of similarity	m^2
A_{sim}	simulated area for the coefficient of similarity	m^2
A_{sub}	submerged area	m^2
A_{tot}	total area for the coefficient of similarity	m^2
A_δ	coefficient for the deviation angle	-
a_w	water acceleration	$m\ s^{-2}$
a_{wood}	wood acceleration	$m\ s^{-2}$
A_{wood}	area perpendicular to the length of the wood piece	m^2
B	channel width	m
c	correction term for the deviation angle	-
C	Chezy coefficient	$m^{1/2}\ s^{-1}$
C_D	drag coefficient	-
$C_D A_f$	drag area	m^2
C_L	lift coefficient	-
c_m	minimum correction term	-
C_M	inertia coefficient	-
C_s	side coefficient	-
C_{sim}	coefficient of similarity	-
C_v	coefficient of variation	-
d	distance between mesh cells	m
D	horizontal shear stress term in curvilinear coordinates	$m^2\ s^{-2}$
D_{wood}	wood diameter	m
F_D	drag force	N

$F_{D,n}$	parallel component of drag force	N
$F_{D,s}$	perpendicular component of drag force	N
F_I	inertial force	N
F_L	lift force	N
F_s	Saffman lift force or side force	m s^{-2}
F_{sx} , F_{sy}	dispersion terms	m s^{-2}
g	gravitational acceleration	m s^{-2}
h	water depth	m
I	secondary flow intensity	m s^{-1}
I_{FD}	secondary flow intensity for a fully developed constant radius curve	m s^{-1}
k	von Karman constant	-
k_s	roughness height	m
L_{wood}	wood length	m
m	velocity-profile exponent	-
m_d	mass of the dowel	kg
n	Manning coefficient	s $m^{-1/3}$
Q_{flow}	flow discharge	m^3 s^{-1}
Q_{wood}	volumetric wood input rate	m^3 s^{-1}
r	hydraulic radius	m
R_s	effective radius of curvature	m
S	source term for secondary flow intensity	m s^{-1}
t	time	s
T	horizontal shear stress term in cartesian coordinates	m^2 s^{-2}
u_w	water velocity	m s^{-1}
u_{wood}	wood velocity	m s^{-1}
u_*	shear velocity	m s^{-1}

U	depth-averaged velocity	m s^{-1}
U_w	depth-averaged water velocity	m s^{-1}
U_{wood}	depth-averaged wood velocity	m s^{-1}
V_{sub}	submerged volume	m^3
W_{eff}	effective weight force	N
y_{wood}	submerged diameter	m
z_b	bed elevation	m
α	coefficient for secondary flow	-
α_n	angle of water surface in transverse direction	°
α_s	angle of water surface in streamwise direction	°
β	nondimensional coefficient for dispersion terms	-
β_c	nondimensional coefficient	-
β^*	nondimensional coefficient	-
γ	angle between coordinate systems	°
δ	deviation angle	°
Δc	gradient of the correction term	m^{-1}
θ	angle of the wood relative to the flow direction	°
λ	adaptation length	-
λ_{gen}	generation length	-
λ_{rel}	relaxation length	-
π	pi number	-
ρ_w	water density	kg m^{-3}
ρ_{wood}	wood density	kg m^{-3}
τ_b	shear stress at the bottom	kg s^{-2} m^{-1}

List of Abbreviations

CS	Cross-Section
I_1	Inlet point n° 1
I_2	Inlet point n° 2
I_3	Inlet point n° 3
LW	Large wood
NSE	Nash-Sutcliffe Efficiency coefficient
M1	Method 1
M2	Method 2
M3	Method 3
RANS	Reynolds Averaged Navier-Stokes equations
RMSE	Root Mean Square Error
RSE	Relative Standard Error
SWE	Shallow Water Equations

Chapter 1

Introduction

1.1 Motivation

The perceptions of the presence of wood in river networks have changed significantly during the past years as potential hazards to humans and infrastructures due to flooding hazards has been contrasted by the ecological importance of river habitats. In fact, wood accumulations create storage areas for organic material and this together with the decomposition of wood itself, provides habitat diversity and nutrients for invertebrates, fishes, and other vertebrates (Benke & Wallace, 2003; Bilby, 2003; Gurnell et al., 2002). On the other hand, the transport of large quantities of wood during floods may cause hazards for humans and infrastructures (De Cicco et al., 2018). In addition, the anthropological intervention for favoring the transportation of wood, especially during the Industrial Revolution in the 18th century, altered the river morphology, with negative consequences on the natural river bed equilibrium and the aquatic ecosystems (Comiti, 2012). Figure 1.1 shows some photographs of aspects related with the presence of wood in rivers.

The afforestation in most of the European catchments due to the abandonment of agricultural lands occurred in the last decades and has resulted in a rising amount of in-channel wood in rivers (Comiti, 2012). For this reason, several processes connected with the presence of wood in the river corridor were studied in order to increase the knowledge and prevent hazards. Consequently, management strategies have been improved in order to guarantee the safeguard of fluvial ecosystems and prevent hazards for human and infrastructures. In particular, large surveys were carried out by European States for assessing the ecological integrity of the rivers with respect to the "natural reference conditions" as requested by the Water Framework Directive (European Commission 2000/60/EC, 2000).

Wood dynamics have been investigated in rivers of different size and morphology to improve the knowledge of transport and deposition of wood pieces along river networks. Aspects of transported wood have been extensively studied to characterize transport regimes mainly in straight river reaches as well as wood jam formation processes, while studies related to the transport of wood through bended channels are rare. Field surveys have shown how the presence of bends influence the transport of wood by recognizing wood jams formed at the outer bank of the river (Abbe & Montgomery, 2003; Hickin, 1984). However, as wood pieces are mobilized during floods, filed measurements are difficult to perform, so that only little data are available on this matter. For this reason, the study of the transport of wood in bended rivers is still at its early stages.

The current research contributes to the knowledge on the transport of wood, in particular, focusing on bended channels. The general aim is to derive a predictive model for the trajectories of floating wood considering the effects of the secondary flows that typically develop in curved rivers.

Figure 1.1 Aspects of wood in rivers: importance for riverine ecosystems (a, picture from Google Images), large accumulation at the Comelico Dam after the flood on 3 November 2018, Italy (b, picture from Italian firefighters), and bridge failure by wood Oklahoma, USA, (c, picture from Bradley et al., 2005).

1.2 Objectives and Methodology

The current research has two main objectives:

- Carrying out rather unique series of laboratory experiments in a curved channel in order to highlight the main variables that are influencing the transport of wood through river bends;
- The implementation of a numerical tool for simulating the transport of wood in presence of secondary currents. The new tool was developed within the 2D hydrodynamic depth-averaged model, Iber-Wood (Ruiz-Villanueva et al., 2014a).

The work is carried out by combining experimental and numerical models. The combination of all the different approaches and methods is essential for the successful completion of the work. In order to achieve the first research objective, an experimental campaign was carried out. In particular, experiments were designed to study the influence of the main variables that usually control the transport of wood in rivers, i.e., wood dimensions, wood orientation, and wood position in the river. The wood transport was reproduced in a double-curved channel under a constant inflow. Cylindrical dowels with no branches and no roots were used to reproduce wood pieces. In particular, four different dowels were considered, two dowel orientations, and three dowel inlet points. Experimental results were analyzed qualitatively and statistically, moreover, they were interpreted through a mathematical model in order to provide new values of drag coefficient that are still lacking in the literature for floating wood pieces.

Due to the three-dimensionality of secondary current flows, 3D models are, strictly speaking, required to properly simulate secondary currents in natural rivers. However, applying 3D models to natural river domains is a very time and computational-consuming procedure (Baghlani, 2012; Lane et al., 1999; Song et al., 2012). 2D depth-averaged models can be enhanced to simulate the effect of the secondary currents on the mean flow, that is to consider the additional stresses due to helical flows on the depth averaged velocity field, or to estimate the surface or near bed velocities, with a good compromise between accuracy and feasibility (Baghlani, 2012; Ghamry & Steffler, 2005; Nabi et al., 2016; Rinaldi et al., 2008; Vasquez et al., 2005). In the present research a methodology for simulating the transport of wood along river bends is presented and implemented in the 2D depth-averaged hydrodynamic model Iber (Bladé et al., 2014) in order to then simulate experimental tests using the model Iber-Wood (Ruiz-Villanueva et al., 2014a), an existing module of Iber.

Research questions, aims and the methodology are summarized in Tab. 1.1.

Table 1.1 Summary of the main research questions, aims and methodology of the current research.

Research question	Aim	Methodology
Which are the main variables that are determining the trajectory of LW in a river bend	To highlight the main variables that are influencing the transport of wood through river bends.	Flume experiments with different dowel dimensions, dowel inlet point and initial dowel orientation.
Which is the drag coefficient for a transported floating LW?	To provide values of the drag coefficient for a floating LW that travels through a channel bend.	Definition of a mathematical model for the transport of floating LW and application of the same to experimental results.
How can a 2D depth-averaged model reproduce the effects of secondary currents on the LW transport?	To implement a numerical tool for the simulation of transported LW in presence of secondary currents.	Implementation of secondary currents effects on the 2D depth-averaged model Iber-Wood; then calibration and validation of the model with experimental results. Application of the implemented model to a river-scale study case.

1.3 Thesis structure

The thesis is organized in six main chapters detailed below and schematized in Fig. 1.2:

- Literature review (chapter 2);
- Dynamics of large wood in sharp river bends (chapter 3);
- Two-dimensional modelling of wood transport in bended channels (chapter 4);
- Simulation of a case study (chapter 5);
- Conclusions and recommendations (chapter 6).

Chapter 2 is a review of the literature concerning the transport of wood in bended rivers and its implications for the river system. It provides a comprehensive summary of the recent advances describing the wood transport regimes, in particular along meanders. Moreover, the existing used methodologies for predict the wood trajectories while transported by the flow are reviewed. Finally, a summary of the knowledge gaps is given.

Chapter 3 presents experimental activity carried out in order to highlight the most importance variables influencing floating wood trajectories in river bends. The experimental setup is described together with the mathematical model used for analyzing experiments. Then, results are presented and discussed.

Chapter 4 reports the implementation of three methods for modelling the effects of secondary currents in an existing 2D hydrodynamic depth-averaged model, Iber-Wood (Ruiz-Villanueva et al., 2014a), in particular for reproducing the effects at the water surface. The model is tested comparing it with the experimental results in order to measure the performances in reproducing the transport of wood in bends.

Chapter 5 presents the applicability of the enhanced version of Iber-Wood model to a river-scale geometry. The new methodologies are tested in reproducing the flood event occurred on 19 June 1996 at the Versilia River (Italy) in order to compare numerical large wood trajectories with available observations.

Lastly, chapter 6 summarizes the main findings of the work and proposes outlooks for future studies.

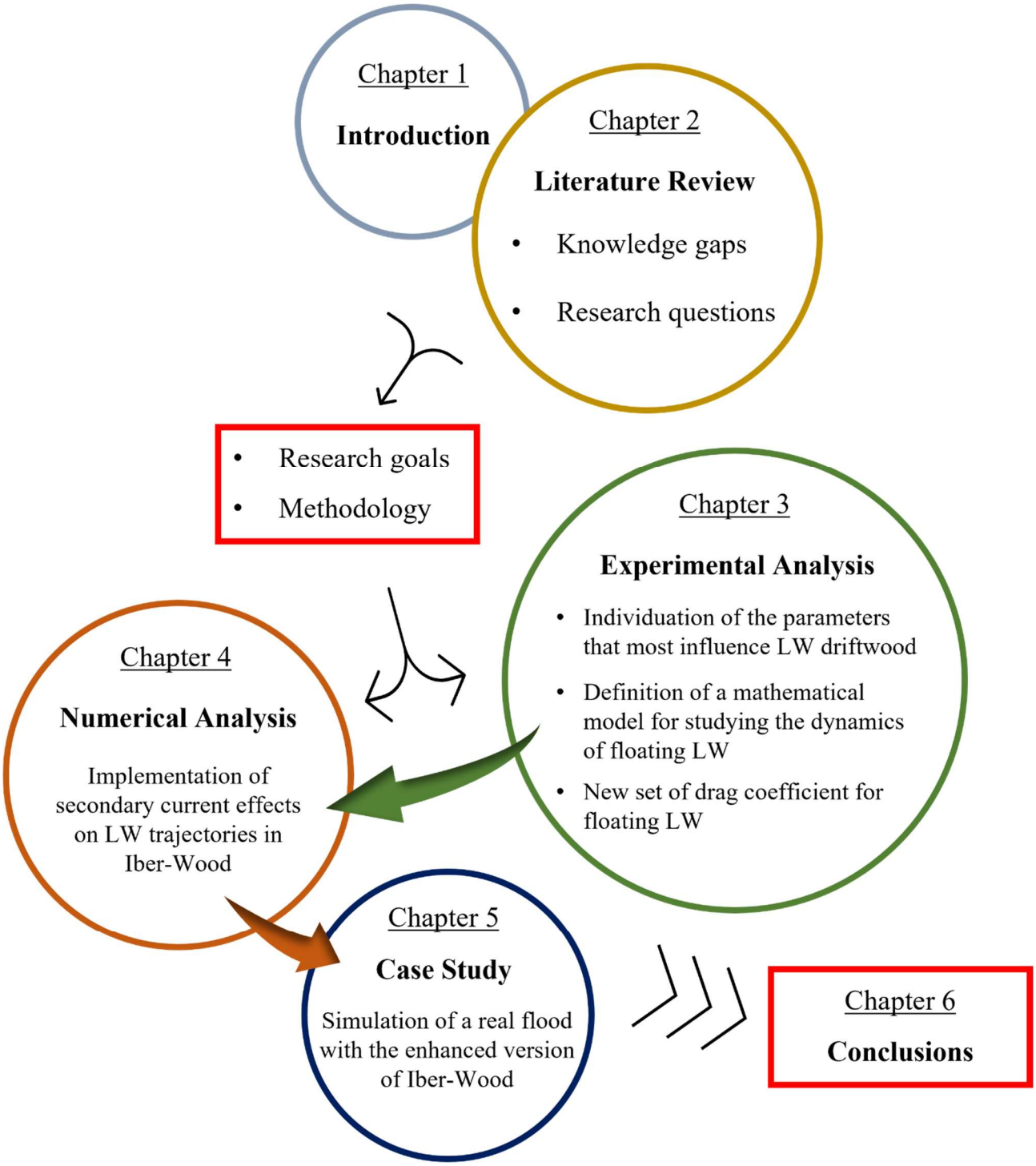

Figure 1.2 Thesis outline.

Chapter 2

Literature review

Large wood (LW) is usually referred to wood pieces longer than 1 m with a diameter larger than 0.1 m that are transported by the flow (Gregory et al., 2003). The study of instream LW has received increasing interest among river scientists in the last decades, and LW is nowadays recognized as one of the crucial drivers of fluvial ecosystems (Gurnell, 2013; Gurnell et al., 2002; Ruiz-Villanueva et al., 2020; Wohl et al., 2016, 2019). However, the presence of instream wood is perceived by a large part of the population as mostly linked to flood hazard or unsafe recreational use of rivers (De Cicco et al., 2018; Wohl et al., 2016).

The dynamics of LW in streams and rivers reflects complex landscape processes that differ by geographic region, time interval, hydrologic regime, basin geology, channel form, network structure, forest composition, disturbance processes, and human influence (Gregory et al., 2003). This is exasperated by the large spatial and temporal variability of wood availability and transport process.

The entrainment of LW into rivers depends on a multitude of different processes (Benda et al., 2003). Natural factors influence the wood entrainment in rivers such as flash flood events which typically affect small basins of temperate climate regions (Comiti et al., 2006), or windstorms and wildfires that are the main factors in coastal areas and wherever large forests exist (Benda et al., 2003), respectively. Another source is the mass movement that may occur in rivers catchments (Benda et al., 2003).

Once entered in river networks, LW is transported by the flow, especially during floods. Long distances can be travelled by wood elements until they are deposited or trapped by engineering structures (De Cicco et al., 2018; Schalko et al., 2018; Wallerstein & Thorne, 1997). Since the transport of LW occurs mainly during floods, corresponding field observations are rather limited as field measurements are difficult to execute during flood situations, so that only little data are available on this matter (Iroumé et al., 2018). For this reason, a complete understanding of instream wood dynamics (especially in terms of transport and deposition) is still lacking.

2.1 Factors influencing wood transport

The transportation of wood in rivers is commonly intermittent, with relatively long periods of stability between episodes of movement (Kramer & Wohl, 2017). Factors influencing wood transport are manifold and distinctive for each river basin (Comiti et al., 2006; Gurnell et al., 2002; Ruiz-Villanueva et al., 2016). The first aspect to consider is the wood availability that is mainly influenced by forest types and stand as well as by the predominant recruitment process (e.g., mass movements on valley sides, fluvial transport from upstream reaches, or bank erosion). The recruited LW may be transported instantly once fallen into the river, or it may be stored in the river corridor (Benda et al., 2003). For example, wood pieces tend to be stable when longer than half their length is outside the channel because less of the piece is exposed to the flow (Lienkaemper & Swanson, 1987). Moreover, the recruitment process determines the LW shape and consequently the mobility of wood pieces, as the presence of branches and roots can anchor LW pieces to the bed, increasing drag and thereby decreasing mobility (Abbe & Montgomery, 2003; Bocchiola et al., 2006; Braudrick & Grant, 2000). Moreover, commonly root systems retain soil causing a strong increase of piece volume and mass (Benda et al., 2003), and an increment of the LW area exposed to the flow, with a consequence in increasing the hydraulic coefficients, drag coefficient (C_d), lift coefficient (C_l), and coefficient of inertia (C_M) (Shields & Alonso, 2012).

Instream wood characteristics are continuously changing in analogy to mineral sediment characteristics due to processes associated with decay, collision, and abrasion. As a result, also the transport dynamics changes. The size of wood pieces relative to channel size strongly influences the process of wood transport (Braudrick & Grant, 2000; Lienkaemper & Swanson, 1987; Wohl, 2011). Ratios of average piece size to channel dimensions, such as average piece length to channel width or average piece diameter to flow depth, may be used to characterize the likelihood of wood mobility (Gurnell, 2003; Gurnell et al., 2002; Lienkaemper & Swanson, 1987). Most mobile pieces are shorter than bankfull width (Nakamura & Swanson, 1994), moreover, the frequency of wood movement increases with increasing channel size (Nakamura & Swanson, 1994).

The flow regime, in terms of magnitude, frequency, and duration of flows, is one of the most important factors influencing wood transport. Recent studies based on i) video tracking of transported wood pieces (MacVicar & Piégay, 2012), ii) monitoring of wood dynamics through repeated photography (Kramer & Wohl, 2014), iii) wood tracking with radio frequency transmitters (Schenk et al., 2014), and iv) numerical modelling (Ruiz-Villanueva et al., 2016), show that wood flux or wood discharge is higher during the rising limb of the hydrograph and lower during the falling limb. This is valid when the main source is in-channel wood or wood entrainment due to bank erosion, while in mountainous basins debris flow and landslides can inject huge amounts of wood also during the falling limb of the hydrograph. Moreover, the recent history of high flows influences mobilization and transport of wood (Wohl et al., 2019). For example, the first significant flood after recruitment can play a disproportionally large role in wood dispersal relative to subsequent flows (Millington & Sear, 2007).

The importance of wood for the development of river morphology was highlighted by field observations (Hickin, 1984; Nanson & Croke, 1992). The presence of floodplains strongly determine the fluvial transport and bank erosion, as they reduce transport of wood and increase its storage, whereas in narrow valley reaches wood tends to be transported downstream (Wyzga & Zawiejska, 2005). A strong relationship between wood dispersal and bed morphology was highlighted in recent years by Bertoldi et al. (2013) and by Welber et al. (2013). This relationship was pointed out in particular for braided channels, in which a small increases of water depth is associated with a major widening of wet area so that, as a consequence, wood dispersion increases and accumulations are smaller (Abbe & Montgomery, 2003). Welber et al. (2013) observed that wood deposition patterns are determined by presence and form of sediment bars. At the bar scale, a large proportion of wood is trapped at bar apex locations, while at reach scale, the first bars downstream of wood input points store the majority of pieces, 30 ÷ 50 % of the wood flux (Welber et al., 2013).

Finally, the presence of in-channel structures generates the entrapment of LW during flood events that may cause hazards to people and infrastructures (Bradley et al., 2005; De Cicco et al., 2018, 2020; Schalko et al., 2018; Schmocker & Hager, 2011, 2013). In fact, LW accumulations at in-channel structures directly reduce the available area for the flow which in turn can cause a backwater rise (Schalko et al., 2018; Schmocker & Hager, 2013), Moreover, large amounts of wood may represent a hazard to the stability of hydraulic structures (Bradley et al., 2005). For these reasons, previous studies investigated the wood blockage probability (De Cicco et al., 2020; Schmocker & Hager, 2011) in order to highlight the effect of the geometry of hydraulic structures, i.e., the bridge deck geometry (Schmocker & Hager, 2011) and the number and shape of bridge piers (De Cicco et al., 2020).

The main characteristics of factors influencing wood transport in rivers described above are classified in Tab. 2.1.

Table 2.1 Classification of the main factors influencing wood transport in rivers.

Classification	*Factors*
Large wood characteristics	• forest type • recruitment process • size: diameter and length • shape: presence of roots and branches • density
Flow regime	• flow hydrograph • recent history of high flows
River morphology	• channel size • channel floodplain-connectivity • local flow width and depth • presence of multithread reaches
In-channel structures	• bridges geometry: number and shape of piers, and decks geometry • retention structures

The main factors controlling the transport of LW are the i) LW characteristics, ii) the flow regime, iii) the river morphology, and iv) the presence of in-channel structures.

2.2 Dynamics of transported wood

LW is mainly mobilized during floods, i.e., for conditions under which field measurements are difficult to execute, so that only little data are available on this matter. Field observations (Abbe & Montgomery, 2003; Hickin, 1984; Nanson & Croke, 1992; Nanson & Hickin, 1986) firstly provided information about the transport of LW in river networks and introduced the concept of wood jams (Abbe & Montgomery, 2003), reporting also the effects of long term storage of wood on locational river morphology (Hickin, 1984; Nanson & Croke, 1992). In addition, flume experiments and numerical modelling have contributed to a better understanding of the processes that are not easily notable in the field, as the entrainment , the transport regimes, and the dynamics of wood jams (Bertoldi et al., 2014; Bocchiola et al., 2006, 2008; Braudrick & Grant, 2000; Braudrick et al., 1997; Meninno et al., 2020; Ruiz-Villanueva et al., 2016, 2020). Also, the interaction between LW and engineering structures was investigated in the last decades for studying possible sources of risks for citizens and infrastructures (De Cicco et al., 2018, 2020; Diehl, 1997; Schalko et al., 2018; Schmocker & Hager, 2011, 2013).

As reported by Diehl (1997), LW is mainly transported in the center of the river in straight reaches (see Fig. 2.1b), occupying only a small fraction of the river width so that the velocity of the wood pieces corresponds approximately to the average flow velocity at the free water surface. In river bends or meanders, the presence of secondary currents induces wood elements to drift to the outer bank (see Fig. 2.1c). The typical helical flow that develops in river bends requires a certain distance, from the beginning of the curve, before reaching the equilibrium (a fully developed secondary current) and a certain distance to decay in the case that the driving force suddenly vanishes (e.g., a bend followed by a straight reach). These distances, highlighted in Fig. 2.1a, are called “generation length” and “relaxation length” (or “adaptation length”), respectively for the generation and the decay of secondary currents (Kalkwijk & Booij, 1986).

Field-observations have shown that LW typically deposits on the outer downstream bank of channel bends or meanders and influences the channel migration and the channel curvature (Abbe & Montgomery, 2003; Hickin, 1984). The obstruction of the flow by LW deposits leads to an increase in water depth upstream of bends which decreases the flow velocities and promotes sediment deposition (Abbe & Montgomery, 2003). These effects are of importance for river ecology as, for example, habitat conditions are altered and nutrients are provided by wood decomposition (Bilby, 2003; Bocchiola, 2011). The element starting wood jam formation is known as “key member”, the smaller pieces are known as “racked members”, and the pieces that occupy the interstitial areas are generally called “loose members” (Abbe & Montgomery, 2003; Curran, 2010; Wallerstein & Thorne, 1997).

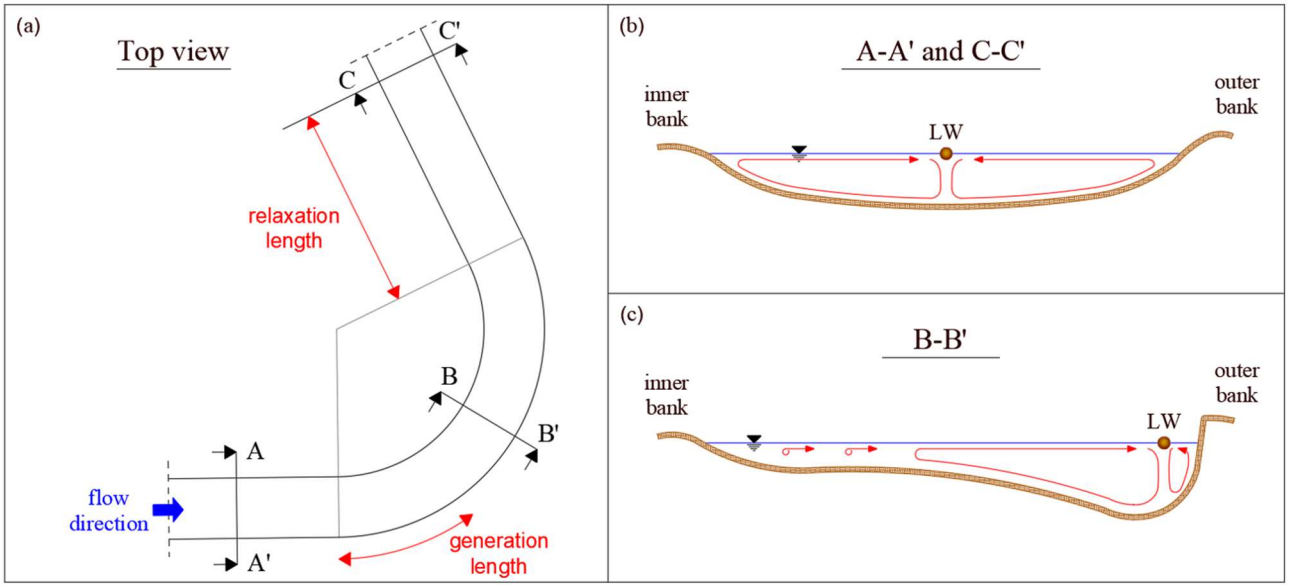

Figure 2.1 Effect of secondary currents on LW. The top view (a) shows the sketch of a river bend in which the generation and the relaxation (or adaptation) lengths are highlighted in red, while panels b and c report respectively the cross-sections of a straight reach and a river bend as described by Diehl (1997).

Instream wood moves downstream in a river as isolated single LW, without interacting with other wood pieces, or as a mass of wood formed by a multitude of wood pieces (Braudrick et al., 1997; Diehl, 1997). Figure 2.2 reports results of the study conducted by Braudrick et al. (1997) that firstly investigated experimentally the wood transport regimes in a straight channel with varying wood input rates (Q_{wood}). They defined three possible conditions: uncongested transport, congested transport, and semi-congested transport. As a function of the ratio between the volumetric wood input rate and the flow discharge (Q_{flow}), the authors defined the uncongested transport for $Q_{wood}/Q_{flow} < 0.015$, in this first case wood pieces are rarely in contact with other pieces. The congested transport was observed for $Q_{wood}/Q_{flow} = 0.07 \div 0.2$, in this case wood pieces move as a single mass, and the semi-congested transport was observed for $Q_{wood}/Q_{flow} = 0.015 \div 0.06$, the latter defines the transition from uncongested to congested transport.

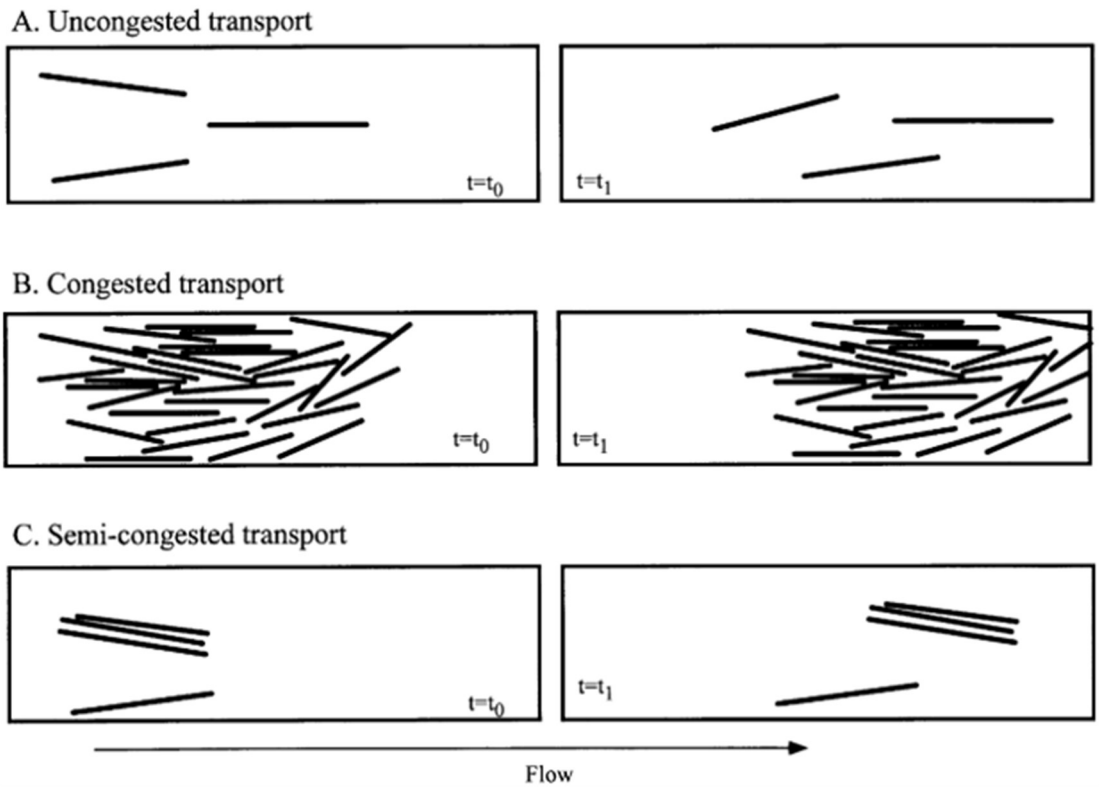

Figure 2.2 Wood transport regimes. Two time-steps are reported for each transport regimes, t_0 means the initial time, while t_1 means a later time step. Source: Braudrick et al. (1997).

The complex interaction of multiple wood pieces among themselves and with the stream environment was in the focus of Alonso (2004) who presented a model for describing the dynamics of a single cylindrical LW by incorporating the effect of transient flow conditions, wood orientation, and interaction with the free surface and the streambanks. Figure 2.3 shows the scheme of the forces acting on a piece of wood used by the author, from which the driving force was expressed, in general, as Eq. 2-1.

$$Driving\ force = W_{eff} + F_D + F_L + F_I \quad (2\text{-}1)$$

in which, forces were defined as:

- *The effective weight of the wood (W_{eff})*

The effective weight of the wood is the weight force minus the buoyant force which is given by Eq. 2-2:

$$W_{eff} = g \cdot \rho_{wood} \cdot L_{wood} \cdot A_{wood} - g \cdot \rho_w \cdot L_{wood} \cdot A_{sub} \quad (2\text{-}2)$$

in which, g is the gravitational acceleration, ρ_{wood} and ρ_w are the density of wood and water, respectively, L_{wood} is the wood length, A_{wood} is the area perpendicular to the length of the wood piece ($A_{wood} = (\pi \cdot D_{wood}^2)/4$, where D_{wood} is the wood diameter), and $A_{sub}$is the submerged area of the wood piece

perpendicular to the length of the wood piece. For a right-circular cylinder A_{sub} depends on the diameter (D_{wood}) and the wood draught (y_{wood}):

$$A_{sub} = \frac{D_{wood}^2}{8}\left\{2 \cdot \cos^{-1}\left(1 - \frac{2 \cdot y_{wood}}{D_{wood}}\right) - \sin\left[2 \cdot \cos^{-1}\left(1 - \frac{2 \cdot y_{wood}}{D_{wood}}\right)\right]\right\} \quad (2\text{-}3)$$

- *The drag force (F_D)*

$$F_D = \frac{1}{2} \cdot \rho_w \cdot C_D \cdot A_f \cdot (u_w - u_{wood})^2 \quad (2\text{-}4)$$

in which C_D is the hydrodynamic drag coefficient of wood in water, A_f is the projected area of the wood in the flow direction, u_w and u_{wood} are the velocities of water and wood. Considering the wood orientation and its influence on the drag coefficient, if θ is the inclination of the wood relative to the flow direction (see Fig. 2.3b), the drag force will be:

$$\overrightarrow{F_D} = \overrightarrow{F_{D,n}} + \overrightarrow{F_{D,s}} \quad (2\text{-}5)$$

which describes the normal and parallel components of the drag force, respectively. Equation (2-5) can be written as:

$$F_D = \frac{1}{2} \cdot \rho_w \cdot C_D \cdot (u_w - u_{wood})^2 \cdot (L_{wood} \cdot y_{wood} \cdot \sin\theta + A_{sub} \cdot \cos\theta) \quad (2\text{-}6)$$

- *The lift force (F_L)*

$$F_L = \frac{1}{2} \cdot \rho_w \cdot C_L \cdot A_f \cdot (u_w - u_{wood})^2 \quad (2\text{-}7)$$

in which C_L is the hydrodynamic lift coefficient of wood in water.

- *The inertia force (F_I)*

$$F_I = \rho_w \cdot C_M \cdot V_{sub} \cdot (a_w - a_{wood}) \quad (2\text{-}8)$$

in which, C_M is the hydrodynamic inertia coefficient, a_w and a_{wood} are the accelerations of water and wood, and V_{sub} is the submerged volume of the wood piece.

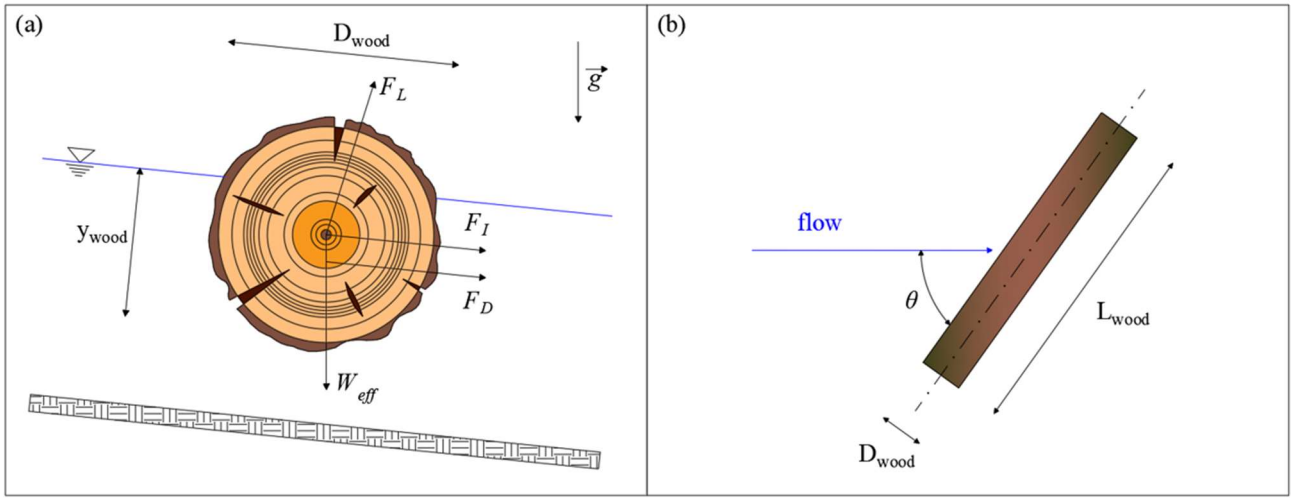

Figure 2.3 Scheme of the forces acting on a piece of wood located in water stream (a) adopted by Alonso (2004) and plan view of the piece lying oblique to the flow (b).

The role of inertia in driving the LW transport was in the focus of the study presented by Persi et al. (2019) that added the effect of the Saffman lift force (Saffman, 1965) to the translation equation (i.e.,, Eq. 2-1), and presented an original formulation for the computation of body rotation on the water surface based on the calculus of the torque acting on the LW piece. The Saffman force or side force ($\overrightarrow{F_S}$) is equal to:

$$\overrightarrow{F_S} = \frac{1}{2} \cdot \rho_w \cdot C_S \cdot A_f \cdot (\overrightarrow{u_w} - \overrightarrow{u_{wood}})^2 \quad (2\text{-}9)$$

in which C_S is the hydrodynamic side coefficient.

The planar rotation equation presented by Persi et al. (2019) was defined as:

$$I \frac{\delta \omega_{wood}}{\delta t} = \sum r \times F + \frac{1}{2} \cdot C_{AI} \cdot I \cdot \left(\frac{d\omega_w}{dt} - \frac{\delta \omega_{wood}}{\delta t} \right) \quad (2\text{-}10)$$

where, I is the cylinder moment of inertia, r is the distance between the body center of mass and the application point of each force F acting on the body, ω_w and ω_{wood} are the angular velocities for water and wood, and C_{AI} is the added inertia coefficient.

The use of Eq. 2-10 allows the computation of the torque with respect to the LW center of mass considering the resistance term (second term on the right-hand side of Eq. 2-10) is named added inertia torque and presents a formulation analogue to the one of the added mass force: the rate of change of the body angular velocity is connected to the difference between the body and the flow angular accelerations, with a proportionality coefficient C_{AI}.

The model proposed by Alonso (2004), as all the models of this type (Braudrick & Grant, 2000; Persi et al., 2019), needs an accurate characterization of all the hydrodynamic forces. Especially the hydrodynamic coefficients, i.e., C_D, C_L, C_S and C_M, must be defined accordingly (Alonso, 2004). Different values for these coefficients can be found in the literature (D'Aoust & Millar, 2000; Gippel et al., 1996; Hygelund & Manga,

2003; Shields & Alonso, 2012, Persi et al., 2019), for example, the drag coefficients vary between 0.3 and 9, which may be associated with LW characteristics such as geometrical dimensions, bark roughness, presence of branches or roots, the orientation with respect to the channel main axis and the flow field geometry. Gippel et al. (1996) firstly provided values of drag coefficients for LW in lowland rivers from a series of experiments in which the drag force was measured using a dynamometer. A similar approach was used by Shields & Alonso (2012), who provided new values of C_D and C_L by applying Alonso's (2004) model in the analysis of their flume experiments. The wood orientation with respect to the flow direction was highlighted as the main parameter that influences the hydrodynamic coefficients. Both Gippel et al. (1996) and Shields & Alonso (2012) derived the hydrodynamic coefficients by analyzing results of a series of flume experiments conducted in straight channels, where wood pieces were mounted on a test stand in order to measure the horizontal and vertical instantaneous forces acting perpendicularly to the piece.

Physical and numerical models are mainly used for studying the transport of wood in rivers as LW is mainly mobilized during floods, i.e. for conditions under which field measurements are difficult to execute.

2.3 Numerical modelling of large wood in rivers

Unlike sediment transport, researchers have been working on modelling wood dynamics only recently by providing numerical models for explicitly simulating wood transport at river reach-scale (Bertoldi & Ruiz-Villanueva, 2017; Kang & Kimura, 2018; Mazzorana et al., 2011, 2018; Persi et al., 2018; Ruiz-Villanueva et al., 2014a, 2020; Zischg et al., 2018). These models generally solve the Shallow Water Equations (SWE) for modelling the water flow hydrodynamics; some of them use different equations for sediment transport modelling; and others propose different approaches to solve the simulation of wood transport. However, only a few fully couple wood transport to hydrodynamics (Kang & Kimura, 2018; Persi et al., 2018; Ruiz-Villanueva et al., 2014a).

One of the first attempts to simulate wood transport in rivers was the model presented by Mazzorana et al. (2011), who considered the whole process chain of LW recruitment, transport and deposition. They calculated LW pathways for a given wood volume and computed the transport conditions using results from a 2D hydrodynamic model. In this case, the flow forces applied on wood elements were considered in order to calculate LW movements, but the influence of wood on the hydrodynamics was neglected. Similarly, Zischg et al. (2018) presented a model for estimating the amount of LW volume at a specific point in a river system. Although the influence of wood on the hydrodynamics was not specifically considered, a simplified approach for considering the retention of LW by bridges was implemented.

The interaction between water flow, wood and morphodynamics was implemented in the more complex models presented by Ruiz-Villanueva et al. (2014a), Persi et al. (2018), and Kang & Kimura (2018). These three two-dimensional models proposed a coupled approach between a Eulerian model used for hydrodynamics and a Lagrangian or discrete element model, for simulating the motion of individual pieces of wood. Moreover, two different approaches were chosen, i.e., kinematic or dynamic method. In the kinematic method, the wood velocity is calculated based on wood density, wood diameter, and water depth, e.g., in floating condition the wood velocity is equal to flow velocity. In the kinematic method, the wood velocity is calculated at each timestep starting from the equations for the wood movement. The latter method was implemented in the models from Persi et al. (2018) and Kang & Kimura (2018), while both methods were implemented in the Ruiz-Villanueva's model (Ruiz-Villanueva et al., 2014a).

The model presented by Ruiz-Villanueva et al. (2014a), Iber-Wood, has been used to model the dynamics of LW elements with and without roots and applied to actual rivers. Iber-Wood is based on the two-dimensional model Iber (Bladé et al., 2014), in which the hydrodynamics is computed by solving the 2D Saint Venant or SWE, with or without considering turbulence (using several turbulence models). The model uses the finite volume method with a time explicit second order and non-oscillatory extension of Roe's upwind scheme on non-structured meshes (see Bladé et al., 2014 for details). Iber-Wood has been extensively applied to study a varied set of aspects related to wood dynamics in rivers with different morphologies (e.g., Ruiz-Villanueva et al., 2014b, 2016, 2017); for further details about Iber-Wood see Appendix C. Persi et al. (2018) proposed an

original formulation for the computation of body rotation on the water surface based on the calculus of the torque acting on the LW piece. In this case, the authors introduced the inertia effect in the planar rotation equation. Moreover, Persi's model differs from Iber-Wood also in the characterization of forces acting on the wood, particularly with considering the presence of the Saffman force (Eq. 2-9). Finally, the model proposed by Kang & Kimura (2018) is similar to Iber-Wood, while allows to a better characterization of the root structure, and consequently simulates the root effects on the flow hydrodynamics.

The main characteristics of the numerical models described above are listed in Tab. 2.2.

Table 2.2 Characteristics of the numerical models on wood transport.

References	*Model dimension*	*Software*	*Model effects*
Mazzorana et al. (2011)	2D + raster data	Sobek ArcGIS Esri	• Using the output hydraulic parameters of numerical simulation into the force balance equation for log movement
Ruiz-Villanueva et al. (2014)	2D	Iber-Wood	• Force balance equation and additional drag term implemented into the 2D Shallow Water Equations (Finite Volume Method with II order Roe scheme) • LW motion: both kinematic and dynamic method • Interaction between logs and boundaries and between logs • Simulation of roots effect
Persi et al. (2018)	2D	ORSA2D	• Force balance equation into the 2D Shallow Water Equations (Finite Volume Method with I order Roe scheme) • LW motion: dynamic method • Interaction between logs and boundaries and between logs
Kang & Kimura (2018)	2D	Nays2DH	• Force balance equation into the 2D Shallow Water Equations (Finite Volume Method with II order TVD-MacCormack scheme) • LW motion: dynamic method • Simulation of roots

The numerical modelling of large wood in rivers has been attempted only recently, nevertheless the model Iber-Wood is widely used for many research studies and engineering applications.

2.4 Two-dimensional modelling of curvature driven secondary flows

At river bends the change in curvature induces an imbalance of the local pressure gradient and the centrifugal force followed by the establishment of a secondary current, also called spiral flow or helical flow (Rozovskii, 1957). This mechanism, that occurs mainly in sharply river curves (curves which are characterized by a curvature ratio less than 2, Blanckaert et al., 2013), results in a three-dimensional flow that induces a redistribution of velocities (see Figs 2.4 and 2.5) and a deviation of boundary shear stress directions (Blanckaert & De Vriend, 2003). Figure 2.4 shows results presented by Rozovskii (1957) in which the velocity profile along a 180° curve is reported for a rectangular cross-sectional channel. In a constant curvature channel (as in the case of Rozovskii's experiment) the maximum velocities shifted from the inner bank to the outer bank moving downstream along the curve, the change on the velocity field depends on the so called free-vortex effect. Figure 2.5 shows the typical redistribution of velocities that occurred in a curved open channel flow. In this case, the cross-sectional shape represents an additional source for secondary flows that is usually called "topographic secondary flow". The resulting local instantaneous velocity components are split into a turbulent and a turbulence-averaged part, and the latter is split into a depth-averaged and a depth-varying part (see Fig. 2.5):

$$u_{wj}(t) = \langle \overline{u_{wj}} \rangle + \overline{u_{wJ}^{*}} + u'_{wj}(t) \qquad (j = s, n) \qquad (2\text{-}11)$$

where, s and n indicate respectively streamwise and transverse directions, t is time, the over bars indicate turbulence-averaging, and the angle brackets indicate depth-averaging.

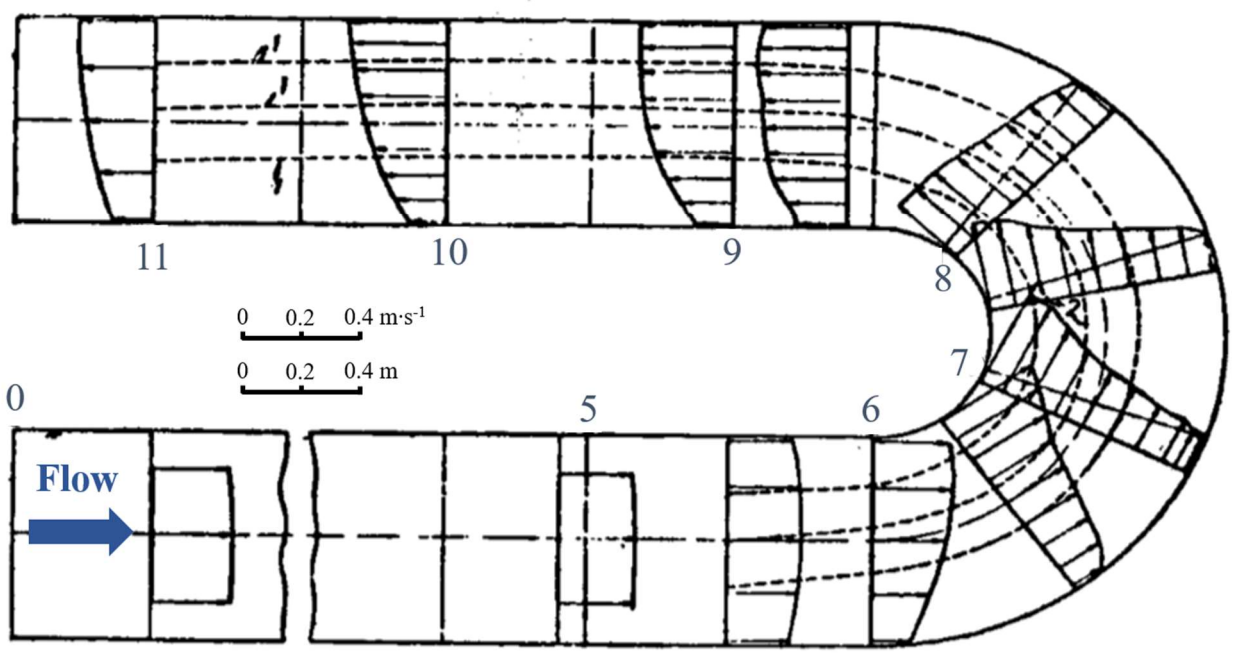

Figure 2.4 Results of the Rozovskii's experiment, the change in the velocity profile is showed along a 180° curve, progressive numbers indicate the cross-section name. Source: Rozovskii (1957).

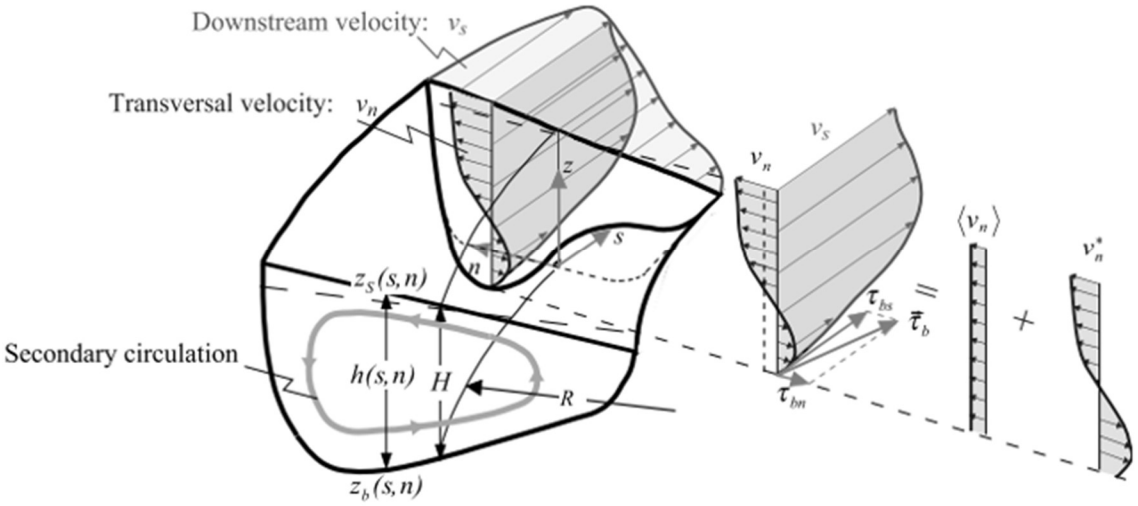

Figure 2.5 Sketch of curved open-channel flow and decomposition of transversal velocity. Notation in figure is different from the one used in the present work, v in figure is equivalent to u_w. Source: Blanckaert & De Vriend (2003).

The simulation of secondary currents in natural rivers requires 3D models due to the three-dimensionality of the helical flow. However, applying 3D models to natural river domains is a very time and computational-consuming procedure (Baghlani, 2012; Lane et al., 1999; Song et al., 2012). On the other hand, using simpler models (1D or 2D) information about secondary flows cannot be captured, for example in 2D depth-averaged models the presence of the helicoidal secondary flow cannot be considered, having a zero depth-averaged mean. However, 2D depth-averaged models can be enhanced to simulate the effect of the secondary currents on the mean flow, that is to consider the additional stresses due to helical flows on the depth averaged velocity field, or to estimate the surface or near bed velocities, with a good compromise between accuracy and feasibility (Baghlani, 2012; Ghamry & Steffler, 2005; Nabi et al., 2016; Rinaldi et al., 2008; Vasquez et al., 2005).

The depth-averaged momentum equations (SWE) obtained integrating three-dimensional momentum equations (Reynolds Averaged Navier-Stokes equations: RANS) contain dispersion terms that are due to the vertical non-uniformity of velocity. These terms are usually negligible in nearly straight reaches, but are of great importance in bends, due to the formation of secondary currents (Baghlani, 2012). The definition of these dispersion terms is not obvious, and in the past many researchers tried to evaluate them in various ways. For example, Kalkwijk & Booij (1986) presented an adaptation of secondary currents to a two-dimensional model which accounts for the convection of momentum of secondary currents in streamwise direction. This solution has been applied in few recent works in which the effects of secondary currents on the main flow was considered adding correction terms to the depth-averaged momentum equations (Baghlani, 2012; Nabi et al., 2016; Rinaldi et al., 2008).

Kalkwijk & Booij (1986) also introduced the concept of "relaxation length" or "adaptation length" (highlighted in Fig. 2.1a) that represents the decay of a fully developed secondary current. The latter concept is necessary

in order to consider the streamwise lag-effect on the secondary current equilibrium. Thus, the intensity of the secondary current, the measure of the magnitude of the component of the secondary current normal to the depth-averaged flow, changes across the channel bend depending on the local radius of curvature of streamline, water depth and streamwise velocity. Jagers (2003) presented a scalar transport model for the streamwise adaptation of the vertical flow structure to curvature changes, in which the secondary current is advected by the depth-averaged velocity. The equation proposed by Jagers (2003) allows the simulation of the secondary flow intensity (I) as:

$$\frac{\partial}{\partial t}(h \cdot I) + \frac{\partial}{\partial x}(U_x \cdot h \cdot I) + \frac{\partial}{\partial y}\left(U_y \cdot h \cdot I\right) = h \cdot S \tag{2-12}$$

in which, u and v are respectively the velocity components in streamwise and transverse direction, and S is the source term of the secondary flow intensity, defined as:

$$S = \frac{(I_{FD} - I) \cdot |U|}{\lambda} \tag{2-13}$$

where, I_{FD} is the spiral flow intensity for a fully developed constant radius curve, defined as:

$$I_{FD} = \frac{h \cdot |U|}{R_s} \tag{2-14}$$

and λ is the adaptation length that can be computed using the formulation proposed by Kalkwijk & Booij (1986):

$$\lambda = \frac{1 - 2 \cdot \alpha}{2 \cdot \alpha \cdot k^2} \tag{2-15}$$

in which, k is the von Karman constant, and α is defined as:

$$\alpha = min\left(\frac{g^{0.5}}{k \cdot C}; 0.5\right) \tag{2-16}$$

where, C is the Chezy coefficient.

Effects of secondary currents on the bedload sediment transport was studied numerically by Vasquez et al. (2005) who included a correction for simulating the deviation of boundary shear stress directions. The authors proposed to correct the surface and near-bed velocity vector directions applying the same deviation angle (δ). Figure 2.6 show their results, while δ was defined as:

$$\delta = arctan\left(A_\delta \cdot \frac{h}{R_s}\right) \tag{2-17}$$

in which, R_s is the radius of curvature, and the A_δ is a parameter defined as:

$$A_\delta = \frac{2}{k^2}\left(1 - \frac{\sqrt{g}}{k \cdot C}\right) \tag{2-18}$$

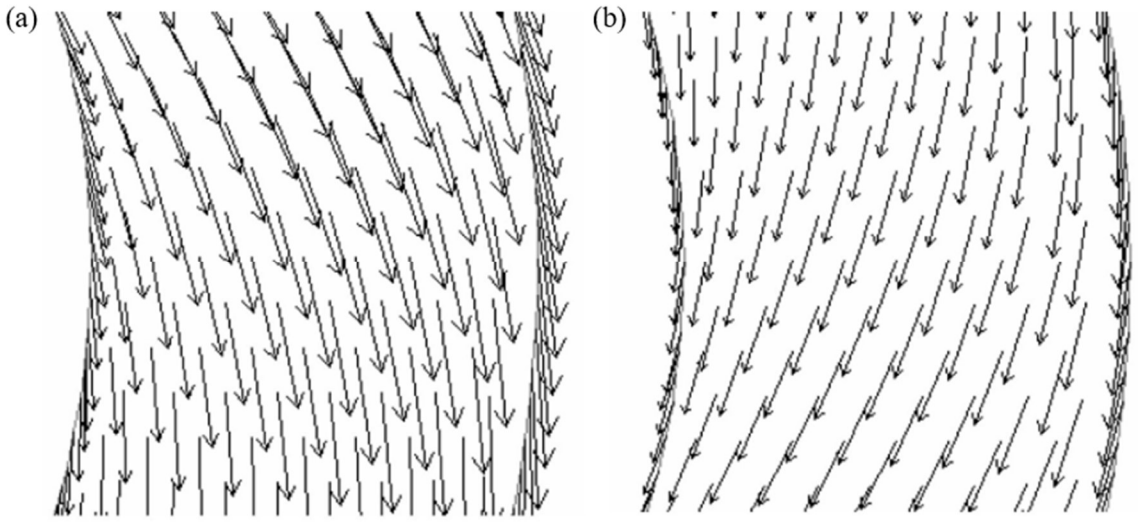

Figure 2.6 Velocity vectors at the water surface (a) and at near-bed (b). Source: Vasquez et al. (2005).

2D depth-averaged models were enhanced in last decades for simulating secondary currents effects in order provide more usable tools by reducing the computational time of 3D simulations.

2.5 Knowledge gaps

Transport of large wood in rivers is a very complex process that depends on several factors, as the wood characteristics, the flow regime, the river morphology, and the presence on in-channel structures (see Tab. 2.1). Only little field data are available on this matter as LW is mainly mobilized during floods, i.e., for conditions under which field measurements are difficult to execute. However, numerous processes have been studied in last decades, especially using physical and numerical models.

Physical and numerical modelling are powerful tools that allow studying flow, sediment, and vegetation dynamics in a controlled environment and open new possibilities for understanding and disentangling the complex linkages in the bio-geomorphological evolution of the fluvial system. Previous studies contributed to the knowledge of how instream wood moves in river networks, to the better understanding of the forces exerted by water on wood pieces and how they change with wood piece orientation. After analyzing the basic mechanisms of wood transport, the next step is to explore the motion of LW in more complex hydraulic conditions such as the presence of secondary flows or investigating the mutual interaction between sediments and wood pieces during floods.

Many flume experiments and numerical models have been proposed, with different details depending on the aim of the investigation. The choice of which model to use (physical or numerical) is dictated by the spatial and temporal scales of the problem, as well as the research question. Both methodologies have been used for investigating the role of different parameters applying simplifying hypotheses. Sometimes physical models are the only way to provide data for calibrating a numerical model, so the two methodologies are developed together.

The flume experiments for studying the transport of wood by the flow have been mainly carried out in straight channels. The study of Meninno et al. (2020) represents an exception as these authors realized a series of flume experiments in a mildly bended channel with a curvature ratio greater than 2. Thus, information on LW transport in sharply bended curves, i.e., curves with a curvature ratio less than 2, is still lacking. Moreover, most physical analysis did not focus on the dynamics of a floating wood piece. Also, the values of hydraulics coefficients (C_D, C_S and C_L) were investigated performing experiments in straight channels and mounting the wood on a test stand in order to measure the horizontal and vertical instantaneous forces acting perpendicularly to the wood piece. However, the dynamics of a floating object may be different.

The complex shape of natural trunks is often schematized with very simple elements such as cylindrical sticks. However, in nature they may have stems and roots, especially when LW enters in the river corridor due to a movement of mass. Thus, a better characterization in terms of stem/foliage distribution, roots structure, and wood form may lead to a more accurate reproduction of the interaction with flow and sediments.

Finally, the two-dimensional modelling of curvature driven secondary flows was carried out in last years with the main objective to simulate secondary current effects on the mean flow and on the bedload sediment

transport. However, to date, there are no studies concerning the effects of secondary currents on transport of floating LW.

The main remaining challenges identified in the literature review are summarized in Tab. 2.3.

Table 2.3 Main knowledge gaps.

	Remaining challenges
Entrainment	• quantification of recruitable wood flux
Transport, Deposition and Remobilization	• live tracking of transported LW • validation of numerical models on wood transport with field data • tests on wood transport combined with morphodynamic processes • implementation of wood transport and sediment transport in numerical models • dynamic investigation of transported wood in curved channels • implementation of secondary current effects on wood trajectories in numerical models
Entrapment	• tests on pier-to-pier accumulation • tests on wood accumulation at bridges in a curved channel
Wood Shape	• implementation of LW elements with complex shapes (considering branches and roots) for computing the interactions between wood pieces and the boundaries

Chapter 3

Dynamics of large wood in sharp river bends

3.1 Introduction

Large wood can be transported in rivers and streams as individual pieces or congested accumulations (jams) (Braudrick et al., 1997). In both cases the corresponding trajectories depend on the wood physical characteristics and the channel system (e.g., river morphology or presence of in-channel structures). In turn, the presence of large quantities of LW strongly influences the hydraulic and morphodynamic characteristics of the channel (Abbe & Montgomery, 2003; De Cicco et al., 2020; Hickin, 1984; Schalko et al., 2018).

The dynamics of transported LW in river corridors have been largely studied by researchers in the last decades to increase knowledge of the numerous processes linked to the presence of wood in river networks, such as the ecological role of wood in river ecosystems, the interaction between wood pieces and the riverbed or with in-channel structures, and the aspects related to hydraulic risk (Abbe & Montgomery, 2003; Bocchiola et al., 2006; Braudrick et al., 1997; De Cicco et al., 2018; Hickin, 1984 and others; see chapter 2). However, the dynamics of LW in sharp river bends has not been studied yet.

In this section, experimental observations about LW dynamics in sharp bends are reported with the aim to explore the role of several parameters on the LW trajectories such as the diameter and length of wood pieces, their approaching position to the bend and their orientation with regard to the main channel axis. Subsequently, a mathematical model is presented for describing the transport of floating LW derived by the Alonso's model (Alonso, 2004). In particular, this model was applied to laboratory experiments to provide new information regarding the drag coefficient of floating LW.

The chapter is organized as follows: experiments are presented by describing the setup, the wooden dowel characteristics, and the experimental protocol (section 3.2); the mathematical model defined for modelling the transport of floating LW is presented in section 3.3, the experimental results are presented in section 3.4, and the results are discussed in section 3.5. Conclusions are reported in section 3.6.

3.2 Experiments

3.2.1 Flume setup

Experiments were carried out in a double-bended channel in the laboratory of the Leichtweiß Institute for Hydraulic Engineering and Water Resources of the Technische Universität Braunschweig, Germany. Fig. 3.1 shows a picture and a sketch of the 26.26 m long channel that is masoned and plastered with a smooth concrete layer. The channel had a rectangular cross-section (2.40 m wide and 0.4 m high) and a slope of 0.001 along the centerline. Both bends alter the channel course for 65° and are characterized by a radius of 3.6 m (regarding the centerline) resulting in a curvature ratio of 1.5. The first bend is a left bend and located 5.46 m downstream of the inlet. The second bend is a right bend, located 4.85 m upstream of the channel outlet and connected to the first one by a 7.74 m long straight section. We note that the rectangular channel cross-section used in the study differs from the typical cross-sectional geometry of natural river bends. However, it was decided to use this channel without further modifications due to the availability of high-resolution 3D velocity data from a previous study (Zaid, 2017) which could be used to characterize the flow field in the bend and its effect on the transport of floating LW through this bend.

Velocity measurements by Zaid (2017) were carried out using a down- and a side-looking Acoustic Doppler Velocimeter (ADV) probe (Vectrino plus from Nortek) with a sampling frequency of 100 Hz, respectively. The grid of the ADV-measurements by Zaid (2017) is indicated in Fig. 3.1b showing that vertical velocity profiles were measured along nine cross-sections (CS1 − 9). In each cross-section seven vertical profiles with 9 points along the vertical were measured. A detailed analysis of the velocity measurements can be found in Zaid (2017). Moreover, since Zaid (2017) worked with a water depth of 0.1 m, the ratio of channel width to flow depth of 24 allowed to safely neglect the effects of the bank shape on the channel hydraulics and on the wood trajectories (expect for the thin boundary layer developing along the bank region).

The discharge to the channel was provided by water circuit of the hydraulic laboratory and regulated by a valve installed at the inlet pipe. The water entered the channel through an inlet basin equipped with flow straighteners and a weir at the downstream end of the channel was used to adjust the water level and water surface slope in the channel. The discharge was measured by an electromagnetic flowmeter (Krohne OPTIFLUX 2300) with an accuracy of ±0.2% of the measured discharge. The water levels along the channel were monitored by three point-gauges that were installed in the channel centerline 3.0 m, 13.4 m, and 23.7 m downstream of the channel inlet section (see Fig. 1). A camcorder (model: Panasonic HC-V520) with a resolution of 1920 x 1080 p and 50 frames per second was placed with top view about 12 m above the flume to capture the movement of wooden dowels through the first bend of the channel for which the 3D flow field was known by the previous work of Zaid (2017).

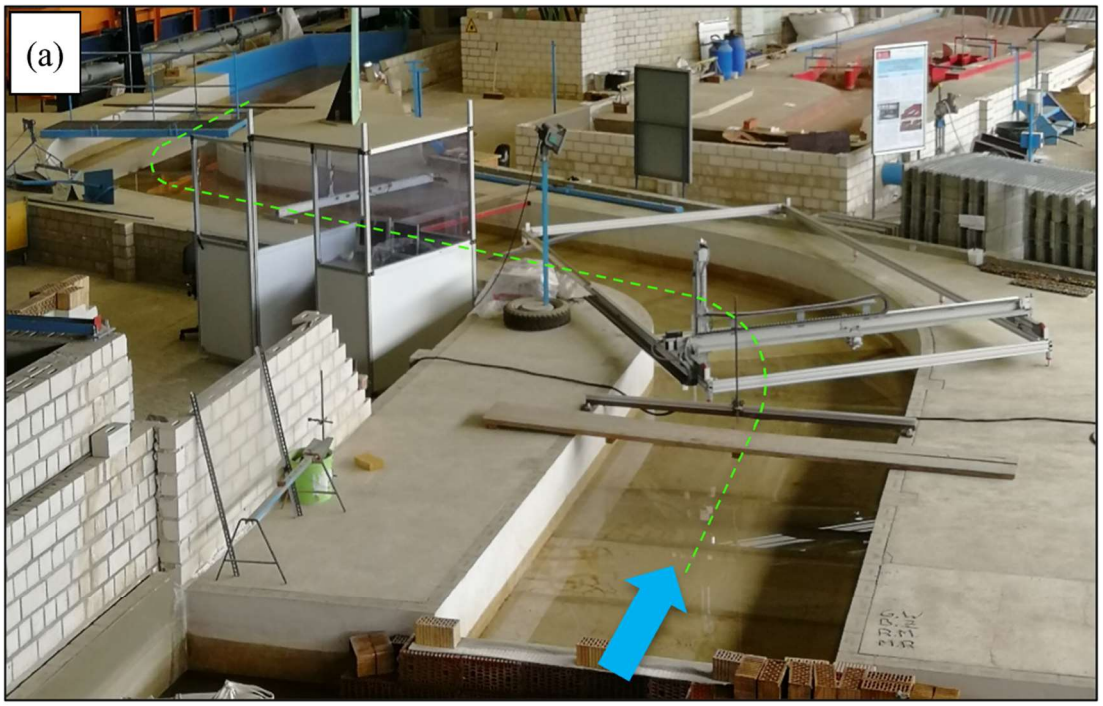
(a)

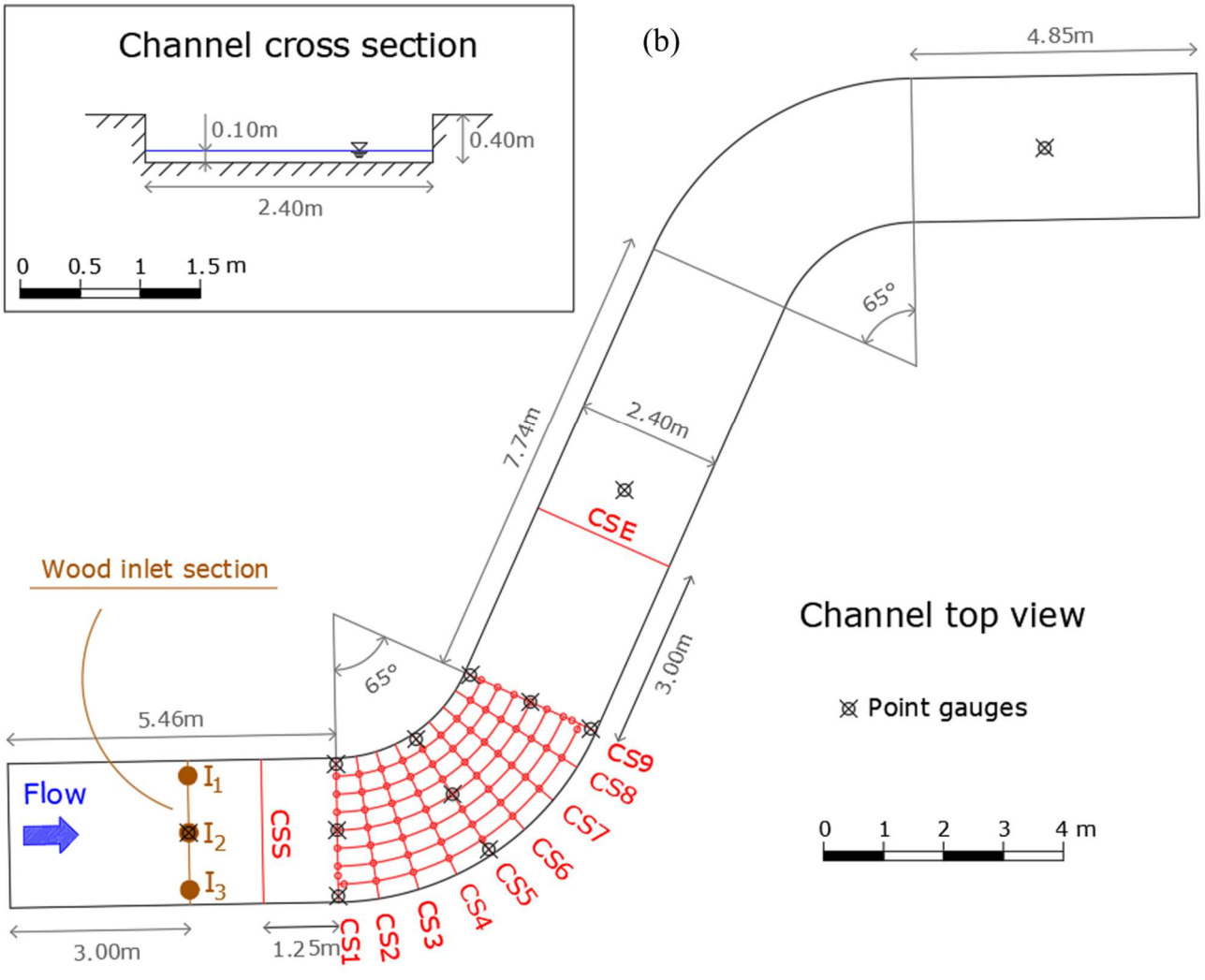
Channel cross section
0.10m
0.40m
2.40m
0 0.5 1 1.5 m
(b)
4.85m
65°
7.74m
2.40m
CSE
Wood inlet section
Channel top view
Point gauges
65°
3.00m
5.46m
Flow
I1
I2
I3
CSS
CS9
CS8
CS7
CS6
CS5
CS4
CS3
CS2
CS1
3.00m
1.25m
0 1 2 3 4 m

Figure 3.1 Picture (a) and sketch (b) of the experimental flume. In the picture (a) the flume centerline is reported in green, and the blue arrow indicates the flow direction. The sketch (b) reports an illustration of the measurement grid used for flow velocity measurements in the first bend modified from Zaid (2017), and the definition of relevant cross-sections. Moreover, the wood inlet section and the point gauge locations are reported.

3.2.2 Wooden dowels

Cylindrical wooden dowels were used to simulate in-channel wood, i.e., branches and roots were not considered in this study. The dowels had a diameter of 0.04 m and 0.06 m and a length of 0.20 m and 0.40 m, respectively, resulting in four different dowel geometries defined in Tab. 3.1. The dowel dimensions were chosen with respect to the scale of the used flume to reproduce LW transportation in a large river (Gurnell et al., 2002) and to guarantee floating condition. Twenty dowels of each type were manufactured using commercial beech wood rods and the dowel extremities were marked with blue and red colored tape, respectively, to facilitate the analysis of the dowel movements based on the camcorder recordings. Once the dowels were manufactured, their density was determined by weighing the dry and wet dowels, respectively. The mean dry density was 740 kg/m^3 for dowel types I and II, and 700 kg/m^3 for dowel types III and IV. For the determination of the wet density, dowels were immersed in water until their weight was constant, Tab. 3.1 reports the ranges and mean wet density of the different dowels; in the following, when referring to the dowel density (ρ_{wood}), we consider the mean wet density reported in Tab. 3.1. Only wet dowels were used for experiments.

Table 3.1 Dowel characteristics.

Dowel	D_{wood} [cm]	L_{wood} [cm]	Wet density [kg/m^3]	Mean wet density [kg/m^3]
I	4	20	848 ÷ 875	861
II	4	40	772 ÷ 838	800
III	6	20	713 ÷ 806	740
IV	6	40	704 ÷ 761	734

3.2.3 Experimental protocol

The experiments were carried out using the same hydraulic boundary conditions as Zaid (2017), i.e., a constant discharge of 130 l/s, a water surface slope that in average was equal to the bed slope and a water depth of 0.10 m. Hence, the depth/width ratio was 0.04 and resembled the ratio for a large river (Gurnell et al., 2002) and the Froude number resulted in 0.55.

The dowel-experiments were designed to investigate the influence of the (i) dowel diameter, (ii) dowel length, (iii) inlet point, and (iv) initial orientation of the dowel on the transport trajectory through the first bend. Despite

the channel had two bends, only the first one was considered in this study due to the available velocity measurements. All dowels were inserted 3 m downstream of the inlet at three lateral positions ($I_1 - I_3$; see Fig. 3.1b) located in a distance of 0.25 m, 1.2 m, and 2.15 m to the left channel wall, respectively. For each inlet position, the effect of the initial dowel orientation (parallel and perpendicular with respect to the channel axis, respectively) on the dowel trajectory was investigated. The combination of dowel type, inlet point, and initial dowel orientation resulted in a total of twenty-four investigated configurations; a summary of the twenty-four experimental configurations is provided in Table B.1, Appendix B. For each configuration, twenty dowels were manually released and their movement through the bend was recorded by the camcorder.

3.2.4 Evaluation of experiments

The dowel dynamics, trajectories and orientations were obtained from the analysis of every video frame (timestep 0.02 s) using the software Tracker (Brown & Christian, 2011). The observed dowel trajectories are reported and analyzed both, visually and statistically. In particular, the trajectories are displayed using top-view plots with reference to the dowel center of mass. Moreover, a statistical analysis was provided through the definition of a coefficient of variation (C_v), which was calculated as:

$$C_v = \frac{\sigma}{\mu} \tag{3-1}$$

where σ and μ are the standard deviation and the mean distance to the inner wall of the channel at each cross section (CS1 – 9, see Fig. 3.1b), respectively.

In addition, two cross sections located 1.25 m upstream and 3 m downstream of the bend, respectively, (CSS and CSE, see Fig. 3.1b) were defined as reference cross-sections to evaluate the travel time of the dowels through the bend.

3.3 A mathematical model for the transport of floating large wood

The mathematical model presented here was defined for studying the dynamics of isolated dowels along the channel bend with the aim to observe how the drag area ($C_D A_f$, i.e., drag coefficient, C_D, times the frontal area of the dowel, A_f) varied along the bend.

Once the dowels were only partially submerged and always in motion, no interactions with the bottom of the channel are considered, moreover, the apparent-mass force is considered negligible (Braudrick & Grant, 2000; Haga et al., 2002; Alonso, 2004; Bocchiola et al., 2006). Thus, the driving force ($\vec{F}$) acting on a moving dowel is given by:

$$\vec{F} = \overrightarrow{W_{eff}} + \overrightarrow{F_D} + \overrightarrow{F_S} \tag{3-2}$$

where $\overrightarrow{W_{eff}}$ is the effective weight of the dowel in the direction of motion (i.e., the difference between the weight force and the buoyant force), $\overrightarrow{F_D}$ is the drag force, and $\overrightarrow{F_S}$ is the Saffman lift force (see Fig. 3.2). The driving force can be further reduced considering that the slope of the channel is equal to 0.001, so the effective weight becomes negligible. As a result, the linear momentum equation can be written as:

$$\overrightarrow{F_D} + \overrightarrow{F_S} = m_d \cdot \overrightarrow{a_{wood}} \tag{3-3}$$

where m_d is the mass of the dowel and $\overrightarrow{a_{wood}}$ is the dowel acceleration vector. The drag force and the Saffman lift force are defined as in Eqs 2-6 and 2-9, respectively, and the side coefficient (C_S) is calculated using the formulation presented by Persi et al. (2019):

$$C_S = 0.149 \cdot \cos\left(\frac{\theta}{0.279} - 166.19\right) + 0.173 \tag{3-4}$$

Equation 3-3 was not used for modelling the dowel trajectory while it was applied at the nine cross-sections defined along the channel bend (CS1 – 9, see Fig. 3.1b) for observing the variation of $C_D A_f$ along the bend. As a result, Eq. 3-3 was applied nine times for each dowel-run. Every time the analysis was conducted considering the streamwise (s) and transverse (n) directions which were oriented parallel to the water surface. The water velocity was extracted from the flow field measurements (Zaid, 2017). The dowel velocity and dowel acceleration were obtained from the analyses of the video footage using the software Tracker that also provided the direction of motion of the dowel obtained from the positions of the dowels center of mass measured at subsequent timesteps (frames). Accordingly, the frontal area A_f was calculated as:

$$A_f = A_{sub} \cdot \cos\theta + y_{wood} \cdot L_{wood} \cdot \sin\theta \tag{3-5}$$

where A_{sub} represents the submerged area (approximated as in Eq. 3.6), θ is the angle of the piece relative to flow, with $\theta = 0°$ when the dowel is parallel to flow (Fig. 3.2a), y_{wood} is the submerged diameter (approximated as in Eq. 3-7), and L_{wood} is the dowel length.

$$A_{sub} = \frac{\rho_{wood}}{\rho_w} \cdot \frac{\pi \cdot D_{wood}^2}{4} \quad (3\text{-}6)$$

$$y_{wood} = \frac{\rho_{wood}}{\rho_w} \cdot D_{wood} \quad (3\text{-}7)$$

Application of Eq. 3-3 in *s*- and *n*-directions provides the drag force components ($F_{D,s}$, and $F_{D,n}$, respectively) that allows to calculate the drag area from Eq. 2-6 as:

$$C_D A_f = \frac{\sqrt{{F_{D,s}}^2 + {F_{D,n}}^2}}{\frac{1}{2} \cdot \rho_w \cdot (|\overrightarrow{u_w}| - |\overrightarrow{u_{wood}}|)^2} \quad (3\text{-}8)$$

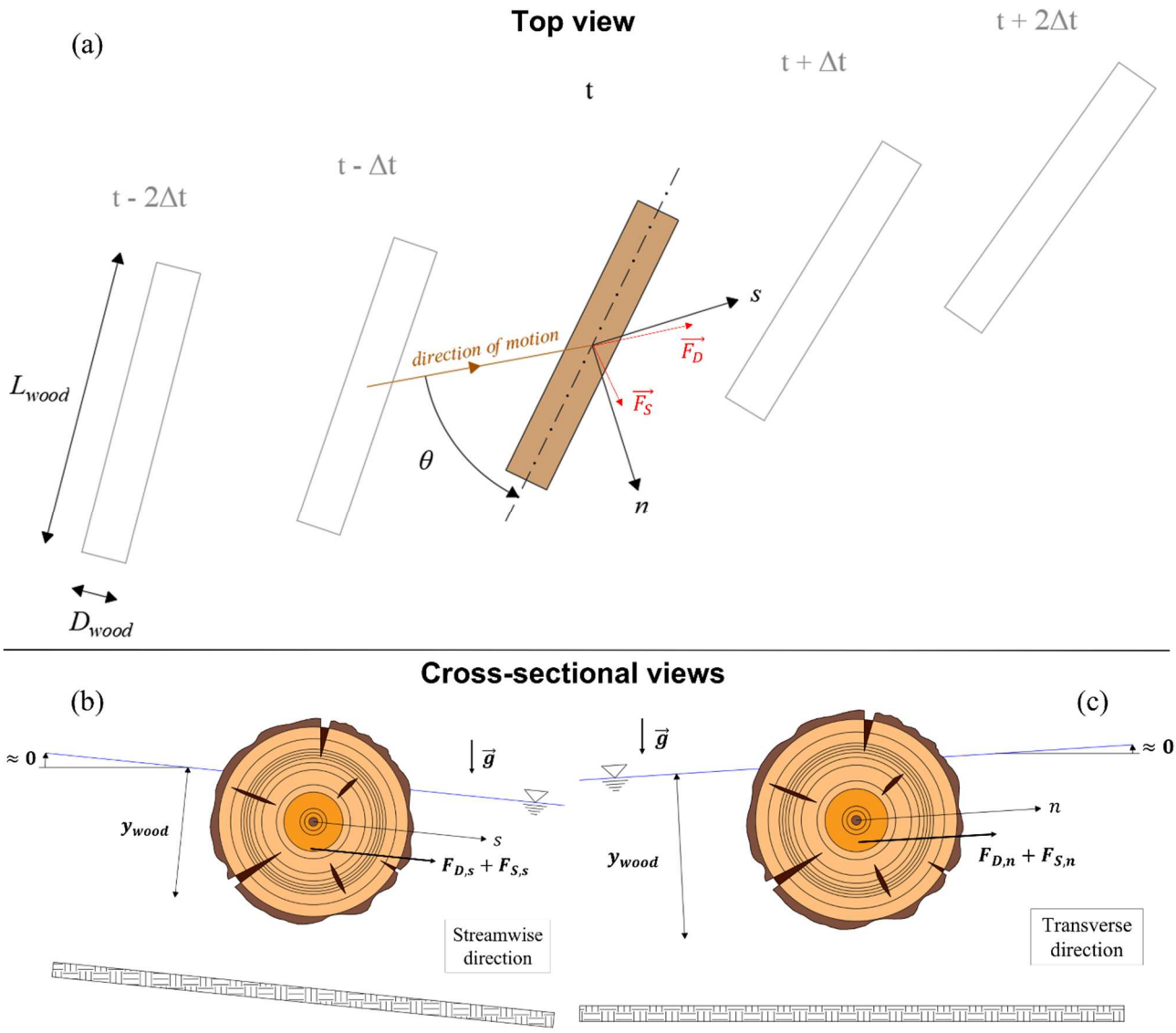

Figure 3.2 Schematic representation of a floating LW dowel. The top view (a) shows the angle of the dowel relative to the direction of motion of the dowel (θ) and the acting forces on the LW piece: the drag force ($\overrightarrow{F_D}$) and the Saffman lift force ($\overrightarrow{F_S}$). Cross-sectional views are presented for streamwise (b) and transverse (c) directions, respectively.

3.4 Results

3.4.1 Flow patterns

Table 3.2 reports the corresponding local water depths h at 0.10 m, 1.20 m and 2.30 m from the inner wall for the cross-sections CS1, CS5 and CS9 as well as the superelevation Δh corresponding to the difference between the water levels at the outer and inner bend in each cross-section. Zaid (2017) observed the highest super-elevation at cross-section CS5, i.e., in the middle of the bend.

Table 3.2 Super-elevations characteristics for CS1, CS5 and CS9 (Zaid, 2017).

		Distance from the inner wall [m]				
		0.1	1.2	2.3		
CS1	h [cm]	9.12	9.73	10.06	Δh [cm]	0.94
CS5		7.88	9.72	10.16		2.28
CS9		8.94	9.91	10.15		1.21

The data collected by Zaid (2017) were used to characterize the 3D velocity field in the first bend of the channel for the used hydraulic boundary conditions. Figure 3.3 (created using the software Tecplot 360) visualizes the velocity magnitude in a plane parallel to the bed located 7 cm above the bottom of the channel (Fig. 3.3a) and within the cross-section CS5 (Fig. 3.3b). Figure 3.3a shows that the maximum velocity was observed at the inner bank whereas lower velocities occurred at the outer bank and thus represent typical velocity patterns that can be observed at the beginning of a bend with constant curvature. Due to higher bed slopes at the inner bend, the so called free-vortex effect prevails while the transverse transport of longitudinal momentum, which tends to decelerate the inner flow and accelerate the outer flow, prevails towards the exit of long bends (Rozovskii, 1957). Moreover, the typical helical motion, which is a characteristic of flows in bends can be identified in Fig. 3.3b and shows transverse flow velocities directed towards the outer (inner) wall at the free surface (channel bottom). The intensity of the transverse velocity in the middle of the bend (CS5) corresponded to 9% of the stream-wise velocity. This is in agreement with Blanckaert & de Vriend (2004)who found in their experiments that the magnitude of transverse velocities is typically 10% of the stream-wise velocity. In the uppermost layers, from z = 7 cm to z = 9 cm, the velocities were substantially constant along the various verticals, as the changes were in the range of 2÷4%. Further details of the flow field can be found in Zaid (2017)and in Appendix A.

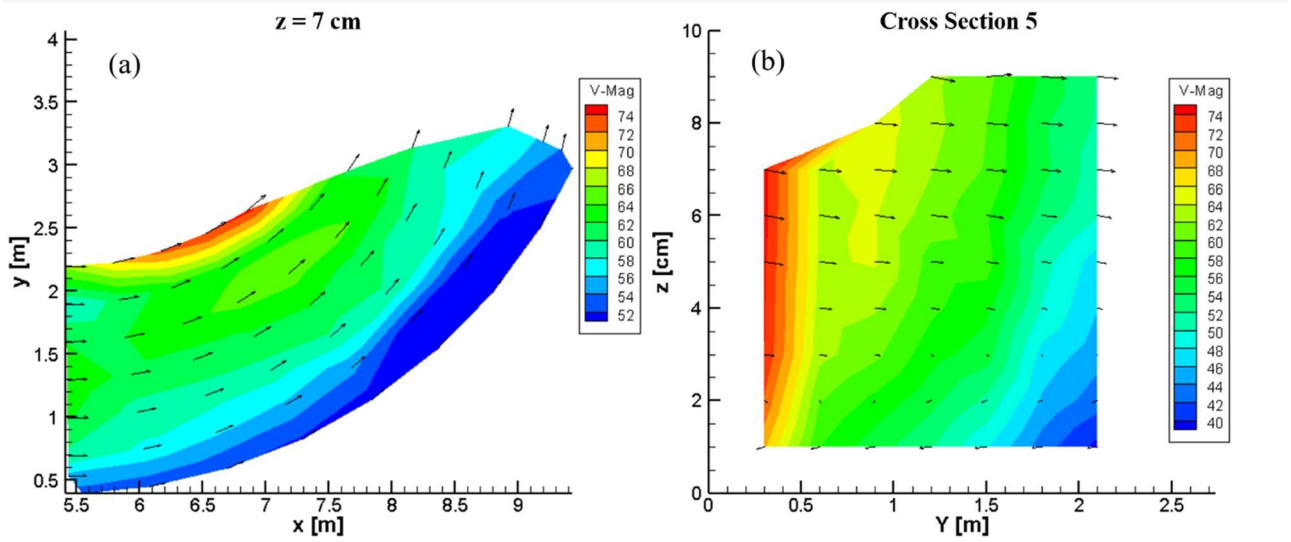

Figure 3.3 2D flow field. The velocity magnitude is reported for the 7 cm horizontal plane (a) and for the cross-section CS5 (b), V-Mag is the velocity magnitude expressed in cm s^{-1} (reproduced from Zaid, 2017).

3.4.2 Dowel trajectories

Figure 3.4 shows the trajectories for the different dowel types released from inlet position I_1 in parallel orientation to the flow (twenty dowels for each experimental configuration). The general behavior of the dowels is similar for the four experimental configurations. After their release, the dowels tended to move slightly away from the left bank before entering the bend. Then, their trajectories progressively moved towards the channel-center without reaching the outer wall, so no collisions of the dowels with the outer wall were observed for this inlet point. For these experimental configurations, the average travel time was lowest for dowel type I (11.8 s) and longest for dowel type IV (13.7 s). Dowel types II and III showed comparable travel times (12.5 s and 12.1 s, respectively) which were between the travel times for dowel types I and IV. For the sake of brevity, here and in the following, only some of the twenty-four experimental configurations will be displayed below; the results for the other configurations can be found in Appendix B.

Moreover, Fig. 3.4 provides a comparison between dowel trajectories and flow streamlines that reveals that the experimental dowel trajectories follow the streamlines at the beginning of the bend but deviate from the streamlines while moving further downstream. This means that the change in curvature ratio of the dowel trajectories is greater than the corresponding change of the streamlines. This evidence was observed in all the experimental configurations performed from I_1 and I_2, while for I_3 the dowels were also following the flow streamlines at the beginning of the bend but due to the collisions with the outer wall the deviation of dowel trajectories from the streamlines was less pronounced.

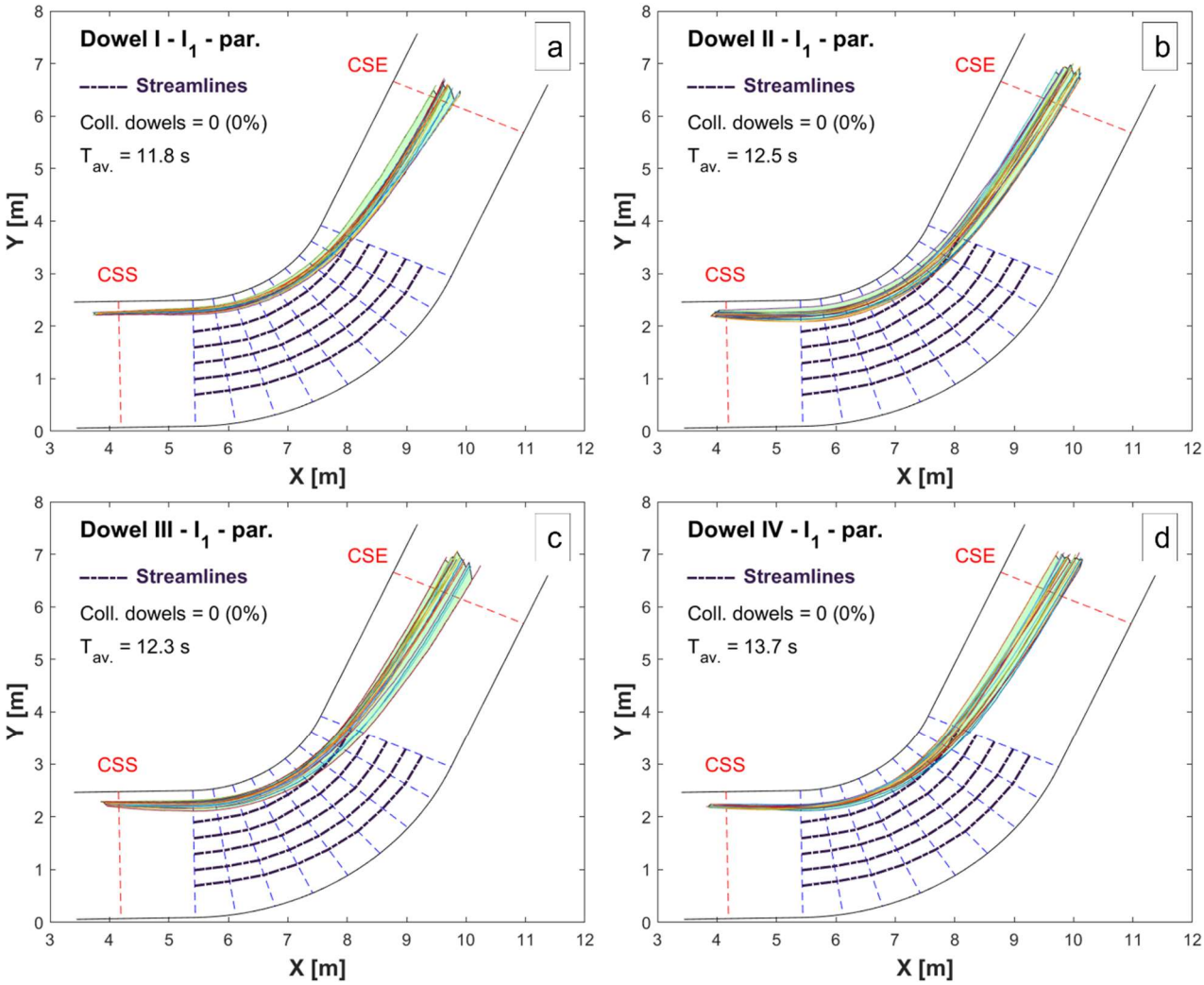

Figure 3.4 Trajectories of experiments in the case of inlet point I_1 and initial dowel orientation parallel to the flow. The results for the four dowels are presented, dowel type I (a), dowel type II (b), dowel type III (c), and dowel type IV (d). $T_{av.}$ is the average travel time between cross-sections CSS and CSE; 'coll. Dowels' are the number (and percentage) of dowels colliding with the outer wall. The flow streamlines are referred to the water surface, defined from the velocity measurements.

The variation of C_v along the bend for the four experimental configurations presented in Fig. 3.4 is shown in Fig. 3.5. The similar behavior of dowel trajectories was confirmed by observing the variation of C_v along the bend. An analysis of variance (anova) confirmed the statistically similitude between dowel types II – IV, while a difference was observed for dowel type I. For dowel types I and II the C_v progressively decrease moving downstream, contrarily, for dowel type III it was almost constant, and for dowel type IV it was increasing along the bend.

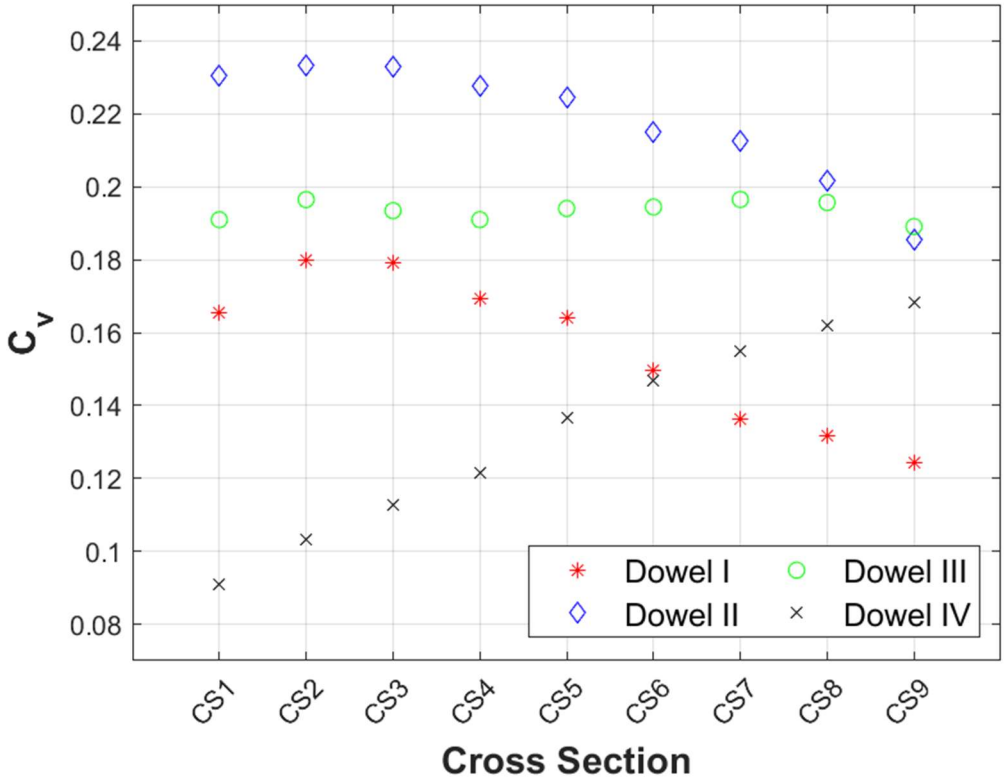

Figure 3.5 Variation of C_v moving downstream into the channel bend for the experimental configurations that considered the inlet point I_1 and the initial dowel orientation parallel to the flow.

Figure 3.6 visualizes the effect of the initial position and orientation on the trajectories exemplarily for dowel type I. The two considered initial orientations of the dowels are reported in the subplots for I_1, I_2 and I_3 (Figs 3.6a, 3.6b and 3.6c, respectively). The dowels inserted from I_1 (Fig. 3.6a) with a parallel orientation are located closer the inner wall and show a larger coefficient of variation than the ones inserted with a perpendicular orientation. This was confirmed by a C_v of 0.14 calculated at CS9 for the parallel initial orientation, while for the perpendicular orientation C_v was 0.12. On the contrary, the dowels released from I_2 (Fig. 3.6b) showed an opposite behavior as the trajectories of the dowels inserted parallel are further away from the inner wall than the ones inserted perpendicularly, but again the coefficient of variation is greater for the first case, 0.09 at CS9 for initial parallel orientation, and 0.07 for dowels inserted perpendicularly. Finally, for the dowels inserted from I_3 (Fig. 3.6c) no differences can be observed between the two cases which can be explained by the collisions of dowels with the outer wall.

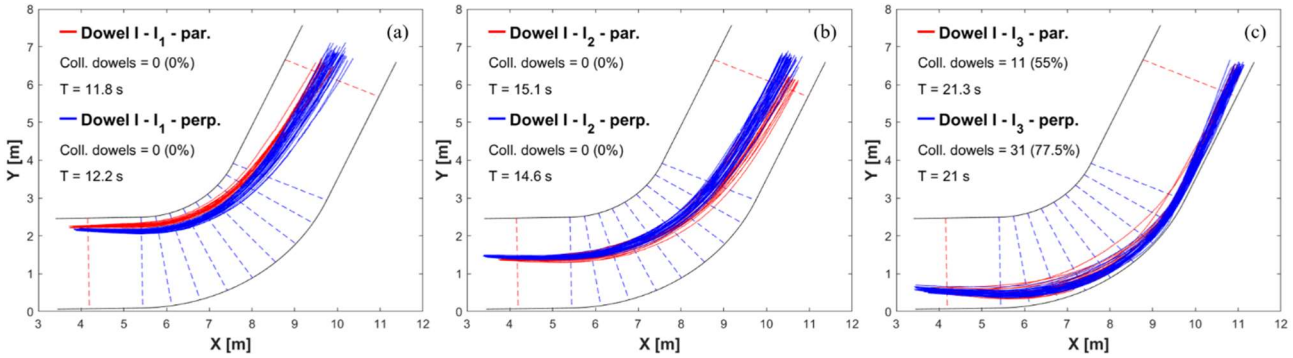

Figure 3.6 Trajectories of experiments with dowel type I. The two considered initial orientations (parallel or perpendicular) of the dowel are reported in each subplot for I_1, I_2 and I_3 (a, b and c, respectively).

3.4.3 Mathematical model

Results of the mathematical model for the twenty-four configurations are shown in Fig. 3.7, in which the variation of the drag area $C_D A_f$ (Eq. 3-8) is presented as a function of the angle of the dowel relative to the motion direction, θ. Results are presented using boxplots; in particular, the 90° rotation of the dowel was divided in six ranges of 15° each. The calculated median values of $C_D A_f$ were almost constant, around 0.005 m^2, independent of θ, thus it can be hypothesized that the pressure distribution around the dowels was nearly constant and not dependent on θ. Moreover, the figure shows outliers for all the defined ranges of θ. These values came from a small percentage of the total number of data, i.e., less than 5%, and could be associated with an overestimation of the dowel velocity by the tracking software. Although the videotape analysis was conducted setting the frame timestep according to the camcorder sampling frequency, the dowels were not clearly visible in some frames, and this might have led to some overestimation of the kinematic variables (i.e., velocity and acceleration).

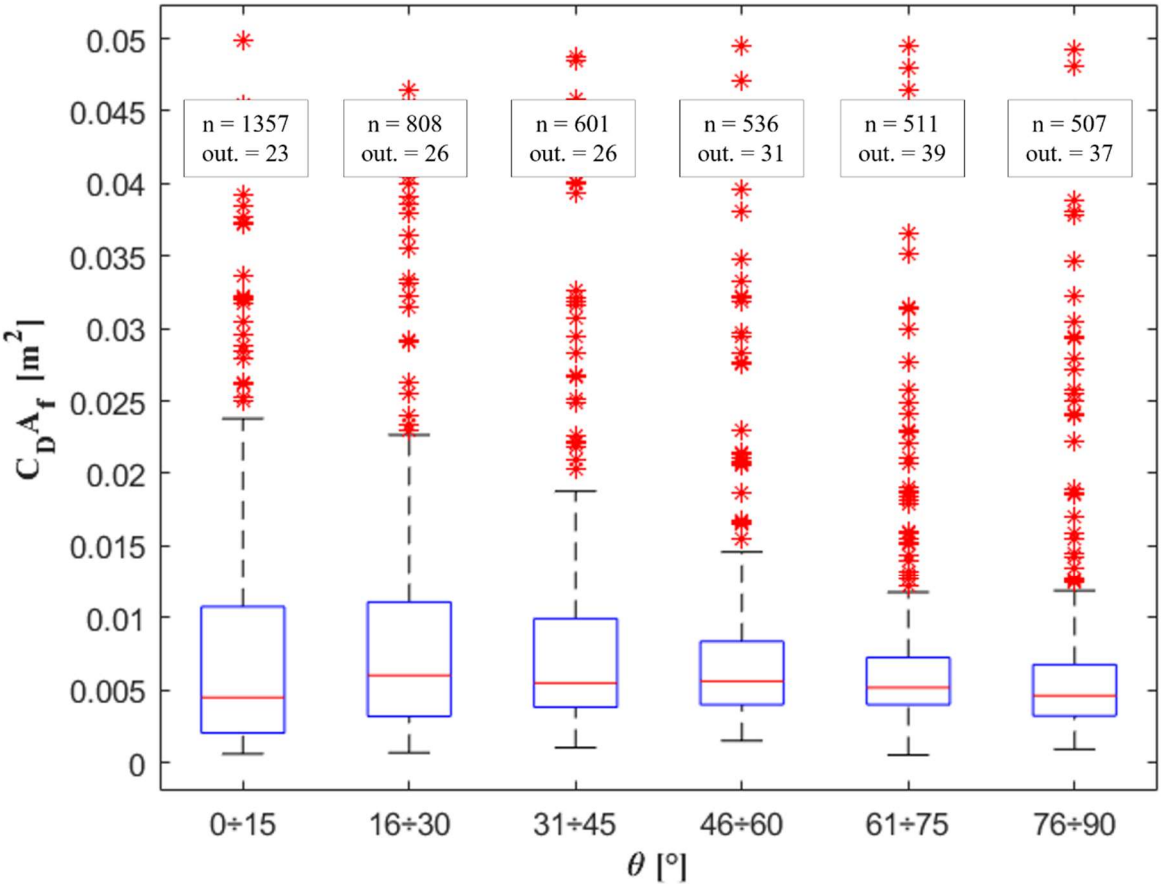

Figure 3.7 Variation of the drag area $C_D A_f$ with the angle θ. Results refer to the twenty-four experimental configurations. The central red mark indicates the median value, while the bottom and the top whiskers indicate the 25th and 75th percentiles, respectively. Moreover, red stars represent outliers whose number is indicated by "out.", while n is the number of samples for each group.

Results of Fig. 3.7 indicate that the drag coefficient decreased with increasing angle θ as A_f increased at the same time (as defined by Eq. 3-8). The variation of the frontal area, A_f, and of the calculated drag coefficient, C_D, are reported in Fig. 3.8 as a function of θ. The C_D median value ranges between 1.2 for $0° \leq \theta \leq 15°$ and 0.4 for $75° < \theta \leq 90°$. This means that a 90° dowel rotation globally induces a decrease of 65% in the drag coefficient. In particular, C_D was mostly halved passing from 0° to 45°, i.e., the mean value reduced 48% between $0° \leq \theta \leq 15°$ and $30° < \theta \leq 45°$ (for which $C_D = 0.6$). Then, the drag coefficient slowly decreases up to $\theta = 90°$ with a reduction of 50% with respect to the range $30° < \theta \leq 45°$. In addition, the best-fit polynomial curve calculated for the C_D results (in a least-squares sense) is shown in Fig. 3.8b:

$$C_D = 1.7053 - 5.2040 \cdot 10^{-2} \cdot \theta + 7.4088 \cdot 10^{-4} \cdot \theta^2 - 3.7139 \cdot 10^{-6} \cdot \theta^3 \qquad (3\text{-}9)$$

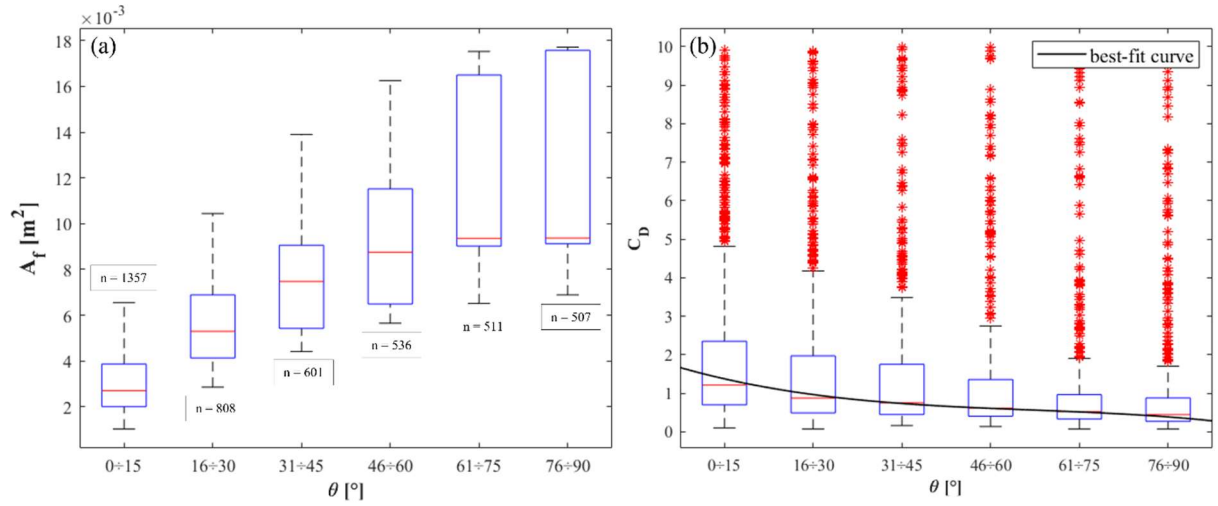

Figure 3.8 Variations of calculated frontal areas (A_f) and drag coefficients (C_D) with θ are reported in panels a and b, respectively. The black line (panel b) represents the best-fit curve considering the median values of boxplots. The central red mark indicates the median value, while the bottom and the top whiskers indicate the 25th and 75th percentiles, respectively. Moreover, red stars represent outliers whose number is indicated by "out.", while n is the number of samples for each group.

The effect of the initial dowel orientation on the model results is shown in Fig. 3.9. A difference was observed for the two considered initial orientation of the dowels, as for the configurations in which the initial orientation was parallel (Fig. 3.9a) the median value of the drag area was increasing with θ, while for the perpendicular orientation (Fig. 3.9b) this variation was not observed. Anyway, in both cases (i.e., parallel and perpendicular, Figs 3.9a and 3.9b respectively) the product $C_D A_f$ ranged between 0.003 m^2 and 0.005 m^2.

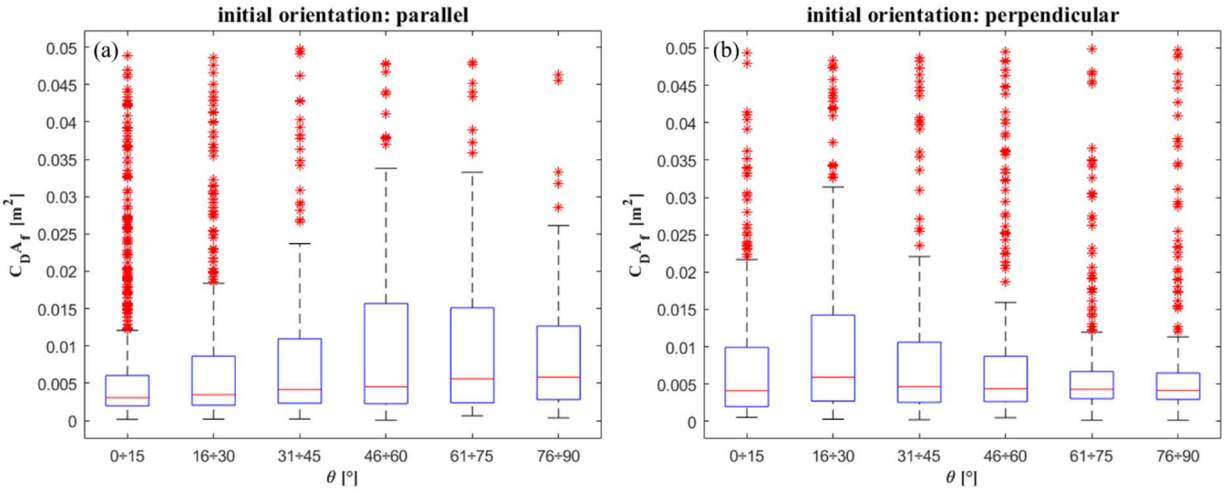

Figure 3.9 Variation of the drag area ($C_D A_f$) with the angle θ for the two considered dowel initial orientation: parallel (a) and perpendicular (b). The central red mark indicates the median value, while the bottom and the top whiskers indicate the 25th and 75th percentiles, respectively. Moreover, red stars represent outliers.

3.5 Discussion

The experimental setup chosen for the presented series of laboratory experiments was designed to investigate the transport of floating LW in river bends. The hydraulic conditions, previously studied by Zaid (2017), reproduced the classical helical flow that is established in sharply river bend (Blanckaert and de Vriend, 2004). Cylindrical wooden dowels were used to simulate LW as defoliated and cylindrical trunks, although in nature wood pieces usually present roots and branches (Benda et al., 2003) is common to use cylindrical dowels for laboratory experiments (Bocchiola et al., 2006; Braudrick et al., 1997; Gippel et al., 1996; Haga et al., 2002; Shields & Alonso, 2012). Moreover, cylindrical LW are recruited by extreme natural events as windstorm and wildfire that typically induce the loss of branches and roots (Benda and Sias, 2003).

The experimental dowel trajectories agree with the description provided by Diehl (1997), LW tends to drift towards the outer wall of the channel while moving downstream. Two main reasons can be identified to explain this observation, the presence of the helical flow and the dowel inertia. The helical flow induces a drift of the dowels as it moves at the surface from the inner side to the outer side of the channel bend. In addition, the own inertia of the dowel concurs to increase the dowel drift. The hydraulic conditions and the dowel dimensions drive the observed dynamics as the linear momentum equation of the dowel (Eq. 3-3) depends on the flow field velocities.

The dowel length (and the corresponding volume) was the main parameter that controlled the drift especially for the dowels inserted parallel to the main flow direction. This is confirmed by Fig. 3.10a, in which the relative distance from the inner wall (distance, d, to channel width, B) at CS5 is plotted as a function of the relative dowel volume (dowel volume, V_d, to the volume of dowel type IV, $V_{d,IV}$) for the configurations with I_1 as starting point and initial parallel dowel orientation. It appears that the dowels of type IV were following a wider trajectory and that the dowels of type II were more distant to the wall than the dowels of type III despite having similar volumes (503 cm^3 for dowel type II and 565 cm^3 for dowel type III). This can be associated with the greater length of dowel type II which is in agreement with findings of Ruiz-Villanueva et al. (2016) who detected the LW length as the main parameter controlling the LW transport in single-thread channels. In fact, the lateral drift increased with the size of the dowel. This is confirmed by results of the mathematical model shown in Fig. 3.10b that, for the same experimental configurations considered in Fig. 3.10a, provides lower values of the drag area for dowel type I and higher values for dowel type IV. While, dowel type II and III results are in between of dowel type I and dowel type IV, in particular, the resulting $C_D A_f$ is higher for dowel type II.

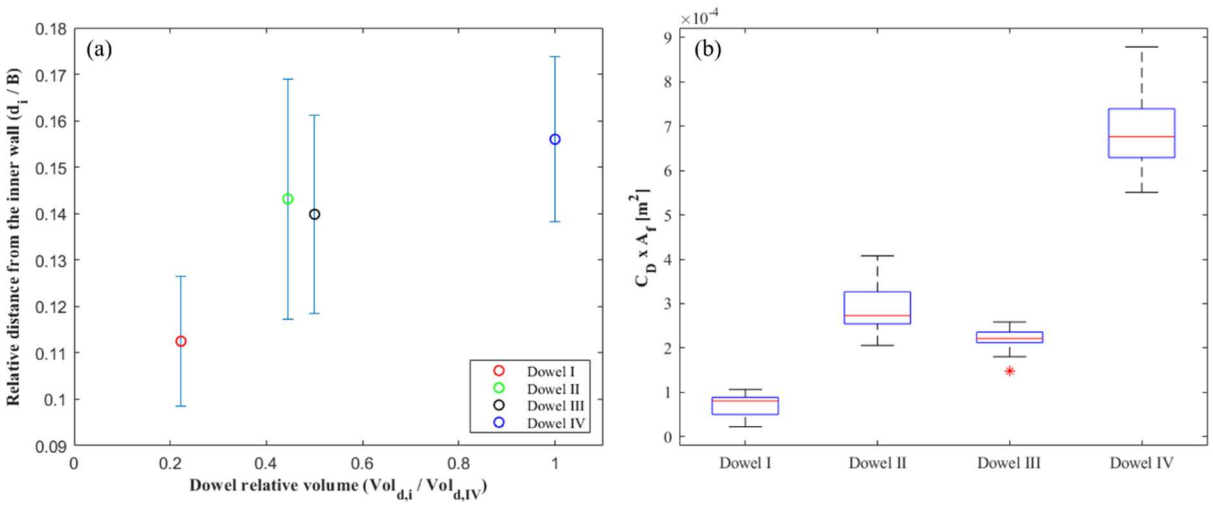

Figure 3.10 Relative distance from the inner wall at CS5 (a) and corresponding values of drag area (b) for the four dowel types. The figure reports results of the four experimental configurations that considered I_1 and the dowel initial orientation parallel to the flow direction. The relative distance from the inner wall is reported as a function of the dowel relative volume, calculated as the ratio between the dowel volume and the volume of dowel type IV. In boxplots (b) the central red mark indicates the median value, while the bottom and the top whiskers indicate the 25th and 75th percentiles, respectively. Moreover, red stars represent outliers.

Estimated drag coefficients are partially in contrast to previous studies (Gippel et al., 1996; Shields & Alonso, 2012) which reported an opposite relationship between drag coefficients and the angle of the dowel relative to the main axis (θ). Figure 3.11 reports the comparison between the results of the present work and results of the aforementioned authors. For the latter, three series of data are reported as the corresponding experiments were conducted by varying the material of the dowels. The results showed a slight increase of C_D with increasing angle θ, while we observed the opposite. This difference can be associated with the different experimental configurations. In fact, in previous works, the authors conducted experiments in straight channels with immobile dowels that were mounted on a test stand in order to measure the horizontal and vertical instantaneous forces acting perpendicularly to the trunk. In the present study, the dowels were transported by the flow through a sharply bend without interacting with the bottom of the channel. Importantly, despite the different experimental configurations, the ranges of variation of C_D of the present work and of the previous studies are comparable. In particular, the calculated median C_D are ranging between 0.3 and 1.2 as the results by Gippel et al. (1996) and Shields and Alonso (2012).

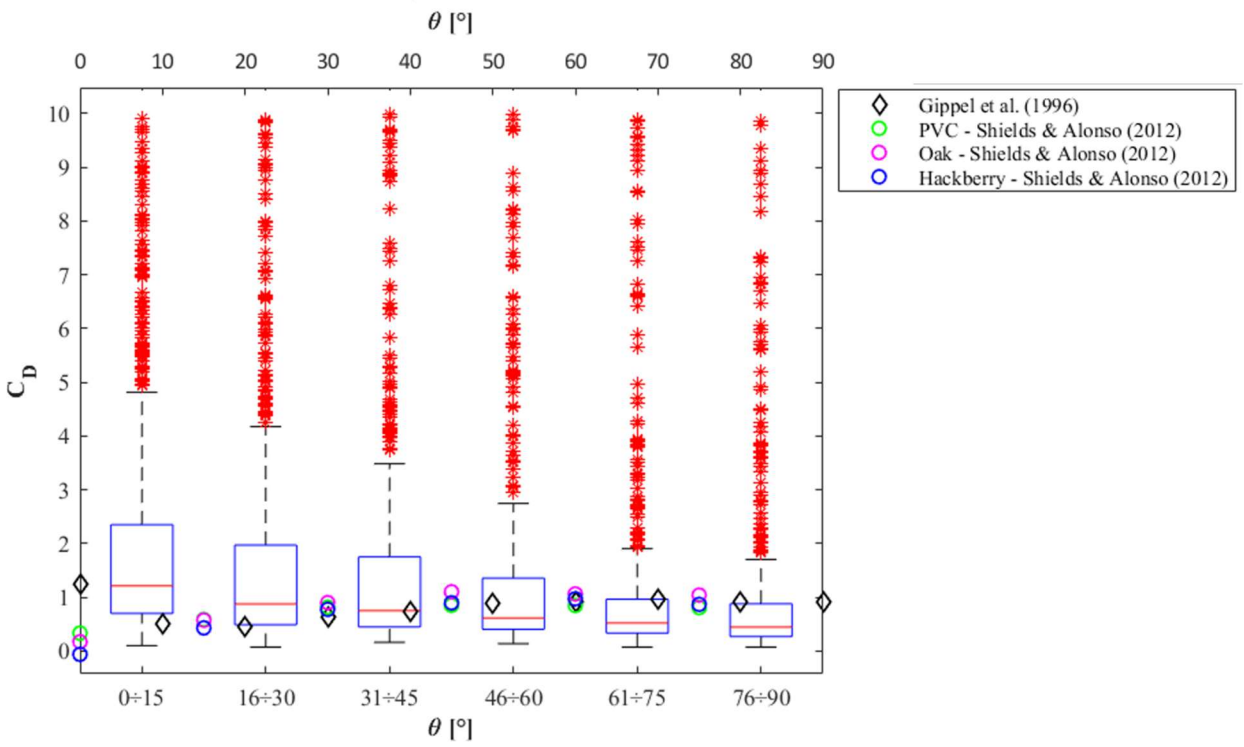

Figure 3.11 Comparison between the results of the present work and the results presented by Gippel et al, (1996) and by Shields & Alonso (2012). Black diamonds represent results from Gippel et al. (1996), while circles represent the results from Shields & Alonso (2012). For this latter case, three series of data are reported as authors varied the dowel material (PVC, oak wood, and hackberry wood). Results are referred to the twenty-four experimental configurations. The central red mark indicates the median value, while the bottom and the top whiskers indicate the 25th and 75th percentiles, respectively. Moreover, red asterisks represent outliers.

3.6 Conclusion

The experimental activity reports novel observations on the trajectories of single floating LW-pieces in sharp bends made in a series of laboratory experiments. The impacts of dowel dimensions, dowel inlet point and initial orientation on the dowel-trajectories were highlighted and the importance of secondary flow was pointed out. The size of the dowel is the most important parameter, in particular the length resulted as the main parameter controlling the dowel trajectory. The deviation of the dowels with respect to the flow streamlines were greater for the longest dowels (dowel type II and dowel type IV) used in the experiments. The approaching position of the dowel to the bend influenced the travel time and the impact of the dowel on the outer wall. The dowels that approached the bend closer to the inner wall travelled faster than others because of the higher flow velocity. In the present series of experiments only the dowels released closer the outer wall impacted with the wall until the end of the bend. The initial orientation of the dowel is important especially for the smaller dowels, in fact the trajectories for dowel type IV with the orientations parallel and perpendicular were indistinguishable.

A mathematical model for studying the dynamics of the transport of floating LW has been presented and applied to the experimental data. Results indicated as drag force increased with the dowel size, that confirmed the importance of the LW size, in particular of the frontal area of the dowel. The measured drag coefficients decreased with increasing angle of the dowel relative to flow, this evidence is opposite with previous studies on drag coefficient for fixed LW in straight channels (Gippel et al., 1996; Shields & Alonso, 2012) that estimated an increasing of C_D with increasing the angle θ. On the contrary, the range of variation is similar being from 0.4 to 1.2.

Further aspects, not considered in this first study, deserves future investigation. For example, experiments were carried out by considering a single constant value of discharge, while non-stationarity was observed as one of the main factors that might control LW transport (Ruiz-Villanueva et al., 2016). Moreover, dowels were released individually, without considering interactions between them. While this assumption was fundamental for highlighting the main parameters controlling the transport of LW in river bends, nevertheless, the formation of wood jams may change the trajectories inducing a greater deviation of the wood than in the present experiments. Finally, the curvature ratio is another factor which deserves some further attention for better understanding the effects of secondary flows.

Chapter 4

Two-dimensional modelling of wood transport in bended channels considering secondary currents effects

4.1 Introduction

In the past, LW transport has mostly been studied on the basis of field surveys (Curran, 2010; MacVicar et al., 2009; MacVicar & Piégay, 2012; Wohl & Goode, 2008 and others) that reported spatial and temporal distribution patterns of wood accumulations and described related transport processes. Additionally, laboratory experiments have been largely used to better understand aspects of the dynamics of the transport of wood that are difficult to observe in the field, as LW is mobilized especially during floods. Laboratory experiments provided information about several processes as the characterization of LW transport regimes (Braudrick et al., 1997) and the tendency to form wood jams (Bocchiola et al., 2008; Davidson et al., 2015), but the interaction between LW and bridges (i.e., bridge piers and bridge decks) has been also investigated (De Cicco et al., 2020; Schalko et al., 2018; Schmocker & Hager, 2011).

As reported in the literature review (chapter 2), the simulation of wood dynamics has only recently been addressed by researchers, who have developed numerical models to explicitly simulate wood transport at river reach-scale (Bertoldi & Ruiz-Villanueva, 2017; Kang & Kimura, 2018; Mazzorana et al., 2011; Persi et al., 2018; Ruiz-Villanueva et al., 2014a, 2020; Zischg et al., 2018). Between these models, only few coupled the simulation of wood transport to the water flow hydrodynamics (Kang & Kimura, 2018; Persi et al., 2018; Ruiz-Villanueva et al., 2014a). In particular, the model Iber-Wood (Ruiz-Villanueva et al., 2014a) has been extensively applied to study a varied set of aspects related to wood dynamics in rivers with different morphologies (e.g., Ruiz-Villanueva et al., 2014b, 2016, 2017); see section 2.3 and Appendix A for model characteristics. However, the model has never been applied to study wood transport in meandering or curved channels. In such morphologies wood transport might be significantly affected by the secondary currents that appear in bends and that may influence the wood trajectories, especially when floating.

In this chapter the implementation of secondary current effects in Iber-Wood is presented and tested in simulating the transport of LW in bended channels. In order to validate the enhanced model results presented in chapter 3 were used. In particular, flow field measurements provided by Zaid (2017) were used to validate the hydrodynamic model performance and observed dowel trajectories were used to validate the approach to represent LW transport.

Since the helical motion is a three-dimensional flow, the goal is the simulation of secondary current effects on the water surface. The depth-averaged momentum equations obtained integrating three-dimensional momentum equations (Reynolds Averaged Navier-Stokes equations: RANS) contain dispersion terms that are due to the vertical non-uniformity of velocity. These terms are usually negligible in nearly straight reaches, but are of great importance in bends, due to the formation of secondary currents (Baghlani, 2012). The first step to achieve the goal of implementing secondary current effects in Iber-Wood was the definition of these dispersion terms. In particular, three definitions of these terms are provided. Then, the variation of the secondary current intensity in river bends was calculated by implementing the equation proposed by Jagers

(2003) in the model (see Eq. 2-12). Finally, a new formulation is provided for correcting the direction of surface velocity vectors according to the presence of the helical flow.

The chapter is organized as follows: the methodology is firstly presented with the description of all the new methods implemented in Iber-Wood (section 4.2), while the description of the transport modelling is reported in Appendix C; then, the results of the simulation of experiments are presented in section 4.3; a discussion of numerical results is provided (section 4.4); finally, conclusion are presented (section 4.5).

4.2 Methodology

4.2.1 Implementation of secondary current effects in Iber-Wood

In order to consider secondary currents in Iber-Wood, the horizontal momentum equations were modified, and the boundary shear stress directions were deviated according to the helical flow characteristics. Moreover, a new equation was introduced in the model to calculate the spiral flow intensity.

The effects of secondary currents on the main flow were considered in the model by introducing additional dispersion stress terms (F_{sx} and F_{sy}) to the two-dimensional depth-averaged horizontal momentum equations (Eqs 4-1 and 4-2).

$$\frac{\partial}{\partial t}(h \cdot U_x) + \frac{\partial}{\partial x}\left(h \cdot U_x^2 + g \cdot \frac{h^2}{2}\right) + \frac{\partial}{\partial y}(h \cdot U_x \cdot U_y) = -g \cdot h \cdot \frac{\partial z_b}{\partial x} + -\frac{\tau_{bx}}{\rho_w} + h \cdot F_{sx} \quad (4\text{-}1)$$

$$\frac{\partial}{\partial t}(h \cdot U_y) + \frac{\partial}{\partial x}(h \cdot U_x \cdot U_y) + \frac{\partial}{\partial y}\left(h \cdot U_y^2 + g \cdot \frac{h^2}{2}\right) = -g \cdot h \cdot \frac{\partial z_b}{\partial y} + -\frac{\tau_{by}}{\rho_w} + h \cdot F_{sy} \quad (4\text{-}2)$$

where t is time, h is the water depth, U_x and U_y are the depth-averaged velocities in x- and y-directions, g is gravity, $z_b$is the bed elevation, τ_{bx} (τ_{by}) is the shear stress at the bottom in x-direction (y-direction), ρ_w is the water density.

Bed shear stresses are defined using the Manning formula (Manning, 1891) as:

$$\tau_{bx} = \rho \cdot g \cdot h \cdot \frac{n^2 \cdot U_x \cdot |U|}{h^{4/3}} \quad (4\text{-}3)$$

$$\tau_{by} = \rho \cdot g \cdot h \cdot \frac{n^2 \cdot U_y \cdot |U|}{h^{4/3}} \quad (4\text{-}4)$$

where n is the Manning coefficient [s m$^{-1/3}$], and $|U|$ is the module of the depth-averaged velocity.

Three methods were considered for the definition of the additional dispersion stress terms F_{sx} and F_{sy}. The first method (M1), follows the adaptation of secondary currents in nearly-horizontal flow proposed by Kalkwijk & Booij (1986) according to which the main flow is assumed to have a logarithmic velocity profile and the secondary current originates from a multiplication of a universal function with the spiral motion intensity. Thus, the additional terms are coupled to parameters of the depth-averaged flow field as reported in Eqs 4-5 and 4-6.

$$F_{sx} = \frac{1}{h}\left\{-2 \cdot \frac{\delta}{\delta x}(\beta \cdot h \cdot U_x \cdot U_y) + \frac{\delta}{\delta y}\left[\beta \cdot h \cdot \left(U_x^2 + U_y^2\right)\right]\right\} \quad (4\text{-}5)$$

$$F_{sy} = \frac{1}{h}\left\{\frac{\delta}{\delta x}\left[\beta \cdot h \cdot \left(U_x^2 + U_y^2\right)\right] + 2 \cdot \frac{\delta}{\delta y}\left[\beta \cdot h \cdot U_x \cdot U_y\right]\right\} \quad (4\text{-}6)$$

where

$$\beta = \beta^* \cdot \frac{h}{R_s} \quad (4\text{-}7)$$

$$\beta^* = \beta_c \cdot (5 \cdot \alpha - 15.6 \cdot \alpha^2 + 37.5 \cdot \alpha^3) \quad (4\text{-}8)$$

$$\alpha = min\left(\frac{g^{0.5}}{k \cdot C}, \frac{1}{2}\right) \quad (4\text{-}9)$$

in the above expressions R_s is the effective radius of curvature of a 2D streamline calculated by Eq. 2-14, α is a nondimensional parameter, k is the von Karman constant, C is the Chezy coefficient, and β_c is set by the user and ranges between 0 and 1, $\beta_c = 0$ means that depth-averaged flow is not influenced by the secondary flow. For further details see Deltares (2019).

The variation of the secondary current intensity I in space and time is computed with the depth-averaged advection equation proposed by Jagers (2003), already presented in Eq. 2-12. In the model two possibilities were considered for the calculation of the adaptation length (λ): it can be computed using the formulation proposed by Kalkwijk and Booij (1986), Eq. 2-15, or it can be set by the user. In the latter case the user can specify the generation length (λ_{gen}) and the relaxation length (λ_{rel}) that control the generation and the decay of spiral flow as in Eq. 4-10.

$$\lambda = \begin{cases} \lambda_{gen} & for \quad I < I_{FD} \\ \lambda_{rel} & for \quad I \geq I_{FD} \end{cases} \quad (4\text{-}10)$$

The deviation of the shear stress direction at the water surface induced by the secondary current was considered by calculating the deviation angle δ, the angle of deviation with respect to the main flow direction, as:

$$\delta_{M1} = c \cdot arctan\left(A_\delta \cdot \frac{h}{R_s}\right) \quad (4\text{-}11)$$

where c is a nondimensional correction term, and A_δ is a nondimensional parameter that depends on the von Karman constant and the Chezy coefficient (Vasquez et al., 2005). The correction term c was inserted in the definition of δ to account for the spiral flow characteristics. In fact, the shear stress deviation is not constant along the cross-section, it is practically zero close to riverbanks (where the flow is mainly vertical), and increases moving from the riverbanks to the main active channel (Blanckaert & De Vriend, 2003). In order to reproduce this effect, the correction term was set equal to zero next to the banks or channel walls, and calculated elsewhere as:

$$c = min(c_m + d \cdot \Delta c\,, 1) \quad (4\text{-}12)$$

where c_m is the minimum correction term of boundary mesh elements, d is the distance to the boundary or lateral channel wall and Δc is the gradient of the correction term.

Iber-Wood's numerical scheme is based on the Finite Volume Method (FVM). Thus, the whole computational domain is discretized with a mesh of triangles or quadrilaterals. Applying Eq. 4-12 to the mesh means that in the row of elements at the model edge, or in the wet elements next to the shore (adjacent to a dry element) the correction is imposed to be exactly c_m, while for the rest, c is calculated with Eq. 4-12, d being the distance between an element center and the nearest element adjacent to a dry one.

The second implemented method (M2) considered the same equations than method M1 for modelling the variation of the secondary current intensity in space and time (Eq. 2-12) and for calculating the deviation angle of boundary shear stresses, δ_{M2} (Eq. 4-11). Thus, method M2 differs from M1 only in the definition of the additional shear stress terms, F_{sx} and F_{sy}. Assuming that the secondary current acts similarly at the water surface and at the bed, the velocity components at the boundaries in x- and y-directions, U_{sx} and U_{sy} at the surface and U_{bx} and U_{by} at the bed, are:

$$U_{sx} = U_{bx} = U_x \cdot \cos\delta_{M2} - U_y \cdot \sin\delta_{M2} \tag{4-13}$$

$$U_{sy} = U_{by} = U_x \cdot \sin\delta_{M2} + U_y \cdot \cos\delta_{M2} \tag{4-14}$$

The velocity field variation due to the secondary current was considered as the source of additional dispersion stress terms, thus, they were considered to be equal to the shear stress at the bed, and defined from the Manning equation as:

$$F_{sx} = g \cdot \frac{n^2 \cdot |U| \cdot (U_{bx} - U)}{r^{4/3}} \tag{4-15}$$

$$F_{sy} = g \cdot \frac{n^2 \cdot |U| \cdot (U_{by} - U)}{r^{4/3}} \tag{4-16}$$

where r is the hydraulic radius calculated for each cell ($r = (B \cdot h)/(B + h)$, with B is the cell width).

Finally, the third implemented method (M3) was based on the analytical approach presented by Odgaard (1986). The author presented a model for steady, subcritical, turbulent flow in alluvial channel curves with uniform bed sediment. The provided model was developed in order to study the portion of the channel cross-section where the effects of the banks on the flow pattern are insignificant. A definition of the shear stress due to the presence of secondary currents can be derived from the Odgaard model. The definition of F_{sx} and F_{sy} is analogous to Eqs 4-5 and 4-6 with a difference in the calculation of the shear stress terms.

The Odgaard model was described in orthogonal, curvilinear coordinates, the velocity profile in streamwise direction was assumed to be given by the traditional power law, while the velocity profile in transverse direction was assumed to be linear; see Odgaard (1986) for details. As a result, the water surface velocity components can be calculated as:

$$U_{ss} = \frac{m+1}{m \cdot |U|} \tag{4-17}$$

$$U_{sn} = -\frac{2 \cdot m + 1}{m \cdot k^2} \cdot \frac{h \cdot |U|}{R_s} \tag{4-18}$$

where subscripts “s” and “n” identify streamwise and transverse direction respectively, and m is the velocity-profile exponent that depends on the von Karman constant, the modulus of velocity and the shear velocity (u_*):

$$m = \frac{k \cdot |U|}{u_*} \tag{4-19}$$

The horizontal shear stress terms were obtained by integrating the velocity profiles along the vertical, and resulted in:

$$D_{ss} = \left(\frac{u_*}{k}\right)^2 \cdot \left\{h - \frac{k_s}{30} \cdot \left[\ln\left(\frac{k_s}{11+}\right)\right]^2 - 2 \cdot \ln\left(\frac{k_s}{11+h}\right) + 2\right\} \quad (4\text{-}20)$$

$$D_{sn} = U_{sn} \cdot \frac{u_*}{k}\left[\frac{h}{4} - \frac{k_s^2}{3600 \cdot h} + \frac{k_s}{60} \cdot \left(\frac{k_s}{30 \cdot h} - 1\right)\right] \cdot \ln\left(\frac{k_s}{30 \cdot h}\right) \quad (4\text{-}21)$$

$$D_{nn} = \frac{h}{12} \cdot U_{sn}^2 \quad (4\text{-}22)$$

where k_s is the roughness height.

D_{ss}, D_{sn}, and D_{nn}, defined for curvilinear coordinates, are calculated in cartesian coordinates as in Eqs 4-23, 4-24, and 4-25.

$$T_{xx} = D_{ss} \cdot (\cos\gamma)^2 + D_{nn} \cdot (\sin\gamma)^2 - 2 \cdot D_{sn} \cdot \cos\gamma \cdot \sin\gamma \quad (4\text{-}23)$$

$$T_{xy} = T_{yx} = D_{ss} \cdot \cos\gamma \cdot \sin\gamma - D_{nn} \cdot \cos\gamma \cdot \sin\gamma + D_{sn} \cdot [(\cos\gamma)^2 - (\sin\gamma)^2] \quad (4\text{-}24)$$

$$T_{yy} = D_{ss} \cdot (\sin\gamma)^2 + D_{nn} \cdot (\cos\gamma)^2 - 2 \cdot D_{sn} \cdot \cos\gamma \cdot \sin\gamma \quad (4\text{-}25)$$

where γ is the angle between curvilinear coordinates (*s, n*) and cartesian coordinates (*x, y*).

As a result, the stress terms added to the depth-averaged horizontal momentum equations resulted:

$$F_{sx} = \frac{1}{h}\left\{\frac{\delta}{\delta x}(h \cdot T_{xx}) + \frac{\delta}{\delta y}\left[h \cdot T_{xy}\right]\right\} \quad (4\text{-}26)$$

$$F_{sy} = \frac{1}{h}\left\{\frac{\delta}{\delta x}\left(h \cdot T_{yx}\right) + \frac{\delta}{\delta y}\left[h \cdot T_{yy}\right]\right\} \quad (4\text{-}27)$$

Similarly to methods M1 and M2, the variation of the secondary current intensity in space and time was computed by applying Eq. 2-12. While the deviation of the shear stress direction at the water surface was directly calculated from the surface velocity components as:

$$\delta_{M3} = c \cdot arctan\left(\frac{U_{sn}}{U_{ss}}\right) \quad (4\text{-}28)$$

The main characteristics of the three implemented methods described above are summarized in Tab. 4.1.

Table 4.1 Main characteristics of the three implemented methods.

	M1	M2	M3
Secondary flow intensity (I)	Modelled with the depth-averaged advection equation proposed by Jagers (2003) $\frac{\partial}{\partial t}(h \cdot I) + \frac{\partial}{\partial x}(U_x \cdot h \cdot I) + \frac{\partial}{\partial y}(U_y \cdot h \cdot I) = h \cdot S$		
Deviation angle at the water surface (δ)	$\delta_{M1} = c \cdot arctan\left(A_\delta \cdot \frac{h}{R_s}\right)$	$\delta_{M2} = c \cdot arctan\left(A_\delta \cdot \frac{h}{R_s}\right)$	$\delta_{M3} = c \cdot arctan\left(\frac{U_{sn}}{U_{ss}}\right)$
	Additional dispersion stress terms (F_{sx}, F_{sy})		
M1	$F_{sx} = \frac{1}{h}\left\{-2 \cdot \frac{\delta}{\delta x}(\beta \cdot h \cdot U_x \cdot U_y) + \frac{\delta}{\delta y}\left[\beta \cdot h \cdot (U_x^2 + U_y^2)\right]\right\}$ $F_{sy} = \frac{1}{h}\left\{\frac{\delta}{\delta x}\left[\beta \cdot h \cdot (U_x^2 + U_y^2)\right] + 2 \cdot \frac{\delta}{\delta y}\left[\beta \cdot h \cdot U_x \cdot U_y\right]\right\}$		
M2	$F_{sx} = g \cdot \frac{n^2 \cdot \lvert U \rvert \cdot (U_{bx} - U)}{r^{4/3}}$ $F_{sy} = g \cdot \frac{n^2 \cdot \lvert U \rvert \cdot (U_{by} - U)}{r^{4/3}}$		
M3	$F_{sx} = \frac{1}{h}\left\{\frac{\delta}{\delta x}(h \cdot T_{xx}) + \frac{\delta}{\delta y}\left[h \cdot T_{xy}\right]\right\}$ $F_{sy} = \frac{1}{h}\left\{\frac{\delta}{\delta x}(h \cdot T_{yx}) + \frac{\delta}{\delta y}\left[h \cdot T_{yy}\right]\right\}$ in which, the shear stress terms are defined following the Odgaard's model		

4.2.2 Experimental setup

The experimental setup used to calibrate and validate the presented model was the one presented in the previous chapter (chapter 3). In particular, with respect to the experiments of dowel type IV, see Tab. 3.1 for dowel characteristics. The focus here was on evaluating the model capabilities in reproducing effects of secondary currents on LW transport in curves.

Dowel-experiments were modelled using Iber-Wood in order to observe the effect of the presented methods on the wood trajectories. A structured mesh with a maximum cell size of 0.1 x 0.1 m was used for reproducing the channel geometry (see Fig. 3.1) in the model. Model boundary conditions were set according to experiments (see section 3.2), a constant inflow of 0.13 m^3/s and a fixed water depth of 8 cm were set for the upstream and the downstream, respectively. The calibration of the model was realized with a two steps procedure: firstly, the calibration of the channel hydraulics was carried out varying the bottom roughness and using the available data of water depths and velocities; secondly the new parameters of the secondary current (i.e., the gradient of the correction term, Δc, and the adaptation length, λ) were calibrated by using the observed experimental dowel trajectories. The final values of these parameters were: a Manning coefficient of 0.011 s $m^{-1/3}$, Δc equal to 1.75, and an imposed λ that was set equal to 50 for both generation and relaxation lengths. Moreover, the turbulence was modelled using the k-eps model (Rastogi & Rodi, 1978) already present in Iber.

4.2.3 Evaluation of simulation performances

The experimental setup was simulated with the three implemented methods and without any correction for considering the presence of secondary currents. The performance of each method was evaluated by calculating the Root Mean Square Error (RMSE), the Relative Standard Error (RSE) and the Nash-Sutcliffe Efficiency (NSE) coefficient (Nash & Sutcliffe, 1970). These measures were calculated taking into account the available data of water depth and velocity at channel bend. Moreover, for testing differences between more than two groups, the *p* value (Kruskal & Wallis, 1952) was calculated in order to identify which pairs of groups were different (significance was set to *p* value < 0.05). In addition, the sensitivity analysis of the model to the variables related to the secondary current was considered and the similarity between observed and simulated wood trajectories was measured by calculating a coefficient of similarity, C_{sim}. The coefficient C_{sim} is a nondimensional coefficient defined as the ratio between the sum of the absolute value of the difference in area (calculated with the formula of trapezoids) and the total available area for dowel trajectories assumed as the area of the channel between CSS and CSE (see Fig. 3.1b); Eq. 4-29.

Due to the definition of the coefficient of similarity, lower values of C_{sim} indicate a better adjustment of the simulated trajectory to the observed one.

$$C_{sim} = \frac{\sum|A_{obs,i} - A_{sim,i}|}{A_{tot}} \quad (4\text{-}29)$$

where A_{obs} and A_{sim} indicate the observed and simulated area, and A_{tot} is the area of the domain. In the present case the domain area was defined as a fixed area of the channel that contained the curve.

4.3 Results

Wood trajectories from Leichtweiß Institute experiments were compared with simulated trajectories obtained using Iber-Wood. All the three implemented methods were used for reproducing the measured experimental hydraulic conditions. Then, simulated trajectories were presented for only the method that showed the best performance.

The sensitivity analysis result of the model to the variables related to the secondary current effects (Δc and λ) is reported in Fig. 4.1. The effect of Δc (Fig. 4.1a) on the trajectories was limited at the beginning of the curve, i.e., trajectories for all the considered models were similar. The method proposed in Eq. 2-15 for calculating λ overestimates the effects of secondary currents, and the resulting simulated trajectory significantly differed from the observed ones (Fig. 4.1b). Contrastingly, the similarity between observed and simulated trajectories increased by specifying λ_{gen} and λ_{rel}. As a result of applying Eq. 2-12, the effects of secondary currents were not limited at the curve, but they were extended to the upstream and downstream, thus, wood trajectories continued deviating to the outer wall even downstream the curve.

As Fig. 4.1 shows, the observed dowel trajectory strongly differed from the simulated one when applying the model without any correction for secondary currents.

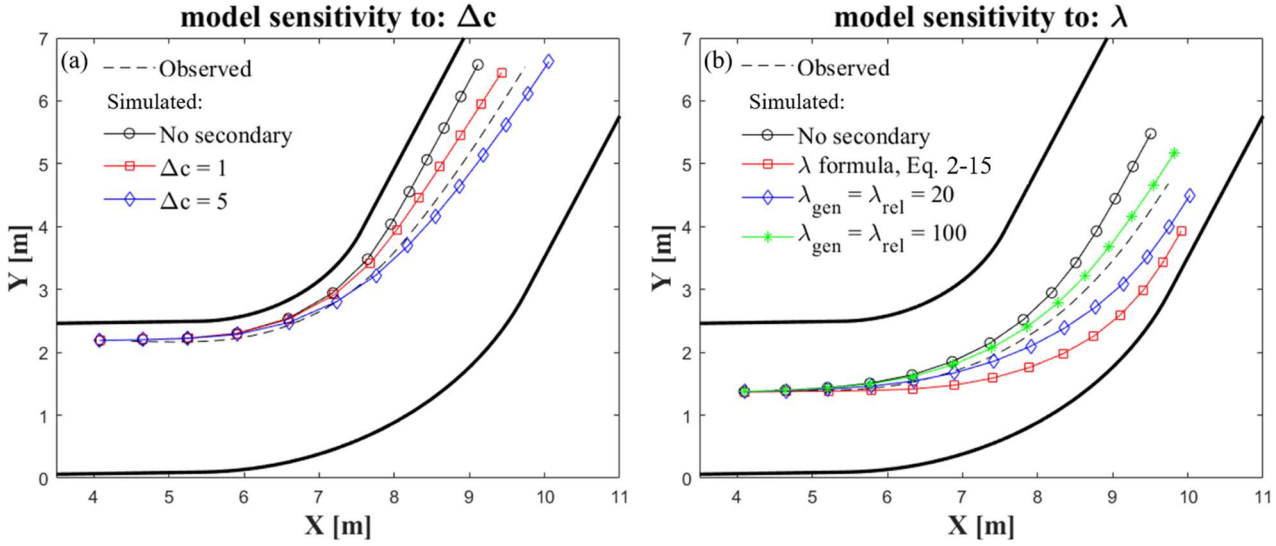

Figure 4.1 Sensitivity analysis of the model to the gradient of the correction term, Δc (a) and to the adaptation length, λ (b). In both panels the observed trajectory is compared with a series of simulated trajectories. For observing the sensitivity to Δc the results for the model without any correction, and for $\Delta c = 1$ and $\Delta c = 5$, are reported. While, for λ in addition to the model without any correction the cases of λ calculated as in Eq. 2-15, $\lambda_{gen} = \lambda_{rel} = 20$, and $\lambda_{gen} = \lambda_{rel} = 100$, are considered.

Figure 4.2 shows the calculated deviation angle, δ, used for correcting the shear stress direction at the surface in the area of influence of secondary currents. The deviation angle was practically zero close to the channel walls and increased moving in cross-sectional direction from walls to the center of the channel. Moreover, δ varied also in the longitudinal direction following the process of formation and decay of secondary currents. As a result, the deviation angle was progressively increasing in the first part of the curve while reaching its maximum value at about the middle of the curve, then remained stable until the end of the curve, once the channel curvature changes the deviation angle started to gradually decrease along the downstream straight reach.

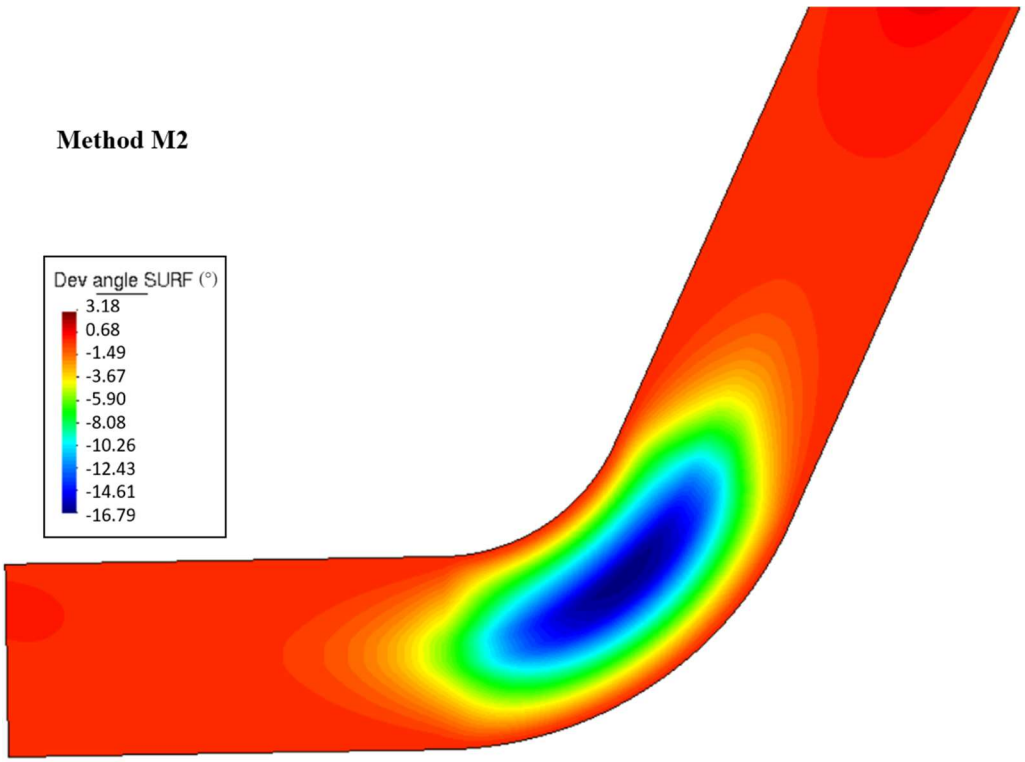

Figure 4.2 Deviation angle at the free surface. Positive deviation means anti-clockwise rotation of vectors direction.

The comparison between observed and simulated values of water depth and water surface velocity is shown in Figs 4.3 and 4.4, while the global performances of the four considered methods are reported in Tab. 4.2; values of the singles cross-sections are reported in the Appendix D. According to these results, no significant differences were found between observed and modelled water depths (p value = 0.99; Fig. 4.3a). Still, according to the model performance assessment, M1 resulted globally the best method in simulating the water depth (Fig. 4.3 and Tab. 4.2), while for other methods an overestimation was observed. In this case, performance for M3 was the worst, whereas the model without correction and M2 showed comparable results always in the middle between M1 and M3. Analogously, the comparison of the magnitude of the surface velocity did no show significant differences between observed and modelled values for which a p value of 0.99 was calculated (Fig. 4.4a). Moreover, results showed that measured surface velocities (Fig. 4.4 and Tab. 4.2) were better simulated by the model without any correction (NSE = 0.61). The others three methods (M1, M2

and M3) were performing similarly with a measured range of variation of the NSE coefficient of 0.57 ÷ 0.59. On the contrary, the comparison of velocity components highlights the differences between results of the four considered methods. Figure 4.5 reports velocity variation of M1, M2 and M3 with respect to the model without any correction for x- and y-components of surface velocity, i.e., surface velocity components of implemented methods minus mean flow velocity components of the model without secondary current effects. Method M1 (Figs 4.5a and 4.5d) was characterized by the presence of fluctuations in the straight reach upstream of the curve and by a region of low velocities close to the left wall of the channel from the middle of the curve to downstream. Differently, for methods M2 and M3 (Figs 4.5b, 4.5c, 4.5e and 4.5f) no differences were observed in the first part of the curve, while from about the center of the curve effects of the introduced approximations became clearly visible, in particular for the central region of the channel. Globally, the secondary current effects approximations modified the velocity field of the channel with respect to the result of the model without any correction, in particular increasing the transverse velocity component and consistently reducing the streamwise component. These changes were commensurately with the area of influence of secondary currents, this is clearly visible in M2 simulation (Figs 4.5b and 4.5e). Moreover, as shown by Figs 4.5c and 4.5f, results of M3 were really similar to the model without secondary current effects with a maximum difference of 0.04 m s^{-1}.

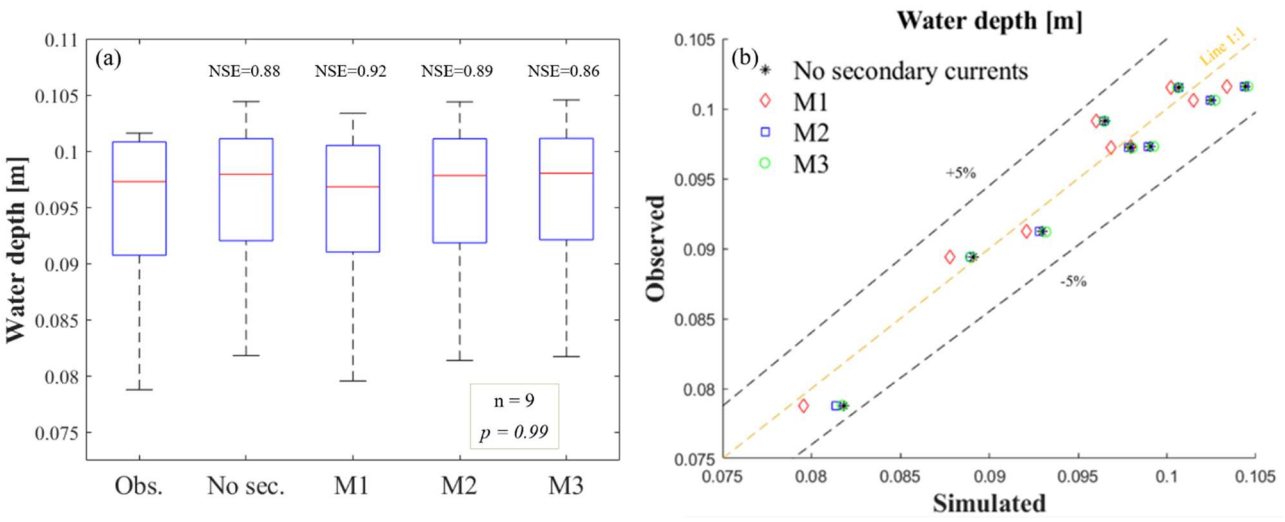

Figure 4.3 Observed and simulated water depth for the different methods implemented in the model. The central red mark in the boxplot (panel a) indicates the median value, while red crosses represent outliers. The bottom and the top whiskers indicate the 25th and 75th percentiles, respectively. n is the number of samples, equal for each group. The *p* value is from the Kruskal-Wallis test.

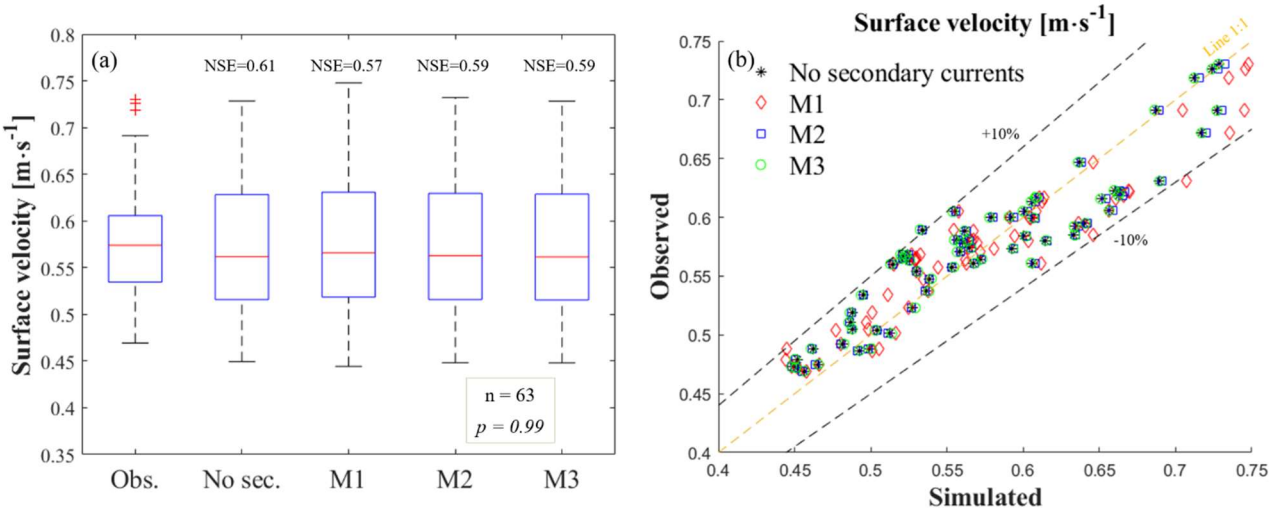

Figure 4.4 Observed and simulated module of water surface velocity for the different methods implemented in the model. The red line within the boxplot (a) indicates the median value, while the bottom and the top whiskers show the 25th and 75th percentiles, respectively. n is the number of samples. The *p* value is from the Kruskal-Wallis test.

Table 4.2 Performances of the methods implemented to simulate Leichtweiß Institute experiments. The reported values represent the global value of RMSE, RSE, and NSE, for water depth and water surface velocity in simulating the flow at the channel curve. Moreover, the minimum and maximum measured values are reported in parenthesis.

	Water depth			*Water surface velocity*		
	RMSE [mm]	RSE [%]	NSE	RMSE [mm s^{-1}]	RSE [%]	NSE
Iber without any correction	1.9 (1.6 ; 2.4)	1.84 (1.3 ; 2.4)	0.88 (0.78 ; 0.94)	29.3 (26.3 ; 38.4)	4.11 (3.0 ; 5.6)	0.61 (-0.24 ; 0.88)
M 1	1.4 (0.8 ; 2.2)	1.32 (0.9 ; 2.1)	0.92 (0.83 ; 0.99)	30.4 (25.9 ; 35.7)	4.14 (2.78 ; 5.3)	0.57 (-0.44 ; 0.89)
M 2	1.8 (1.6 ; 2.2)	1.76 (1.4 ; 2.2)	0.89 (0.81 ; 0.95)	30.0 (27.0 ; 38.3)	4.17 (3.1 ; 5.5)	0.59 (-0.33 ; 0.87)
M 3	2.0 (1.6 ; 2.5)	1.96 (1.4 ; 2.4)	0.86 (0.73 ; 0.94)	29.7 (26.9 ; 39.0)	4.20 (3.1 ; 5.7)	0.59 (-0.31 ; 0.88)

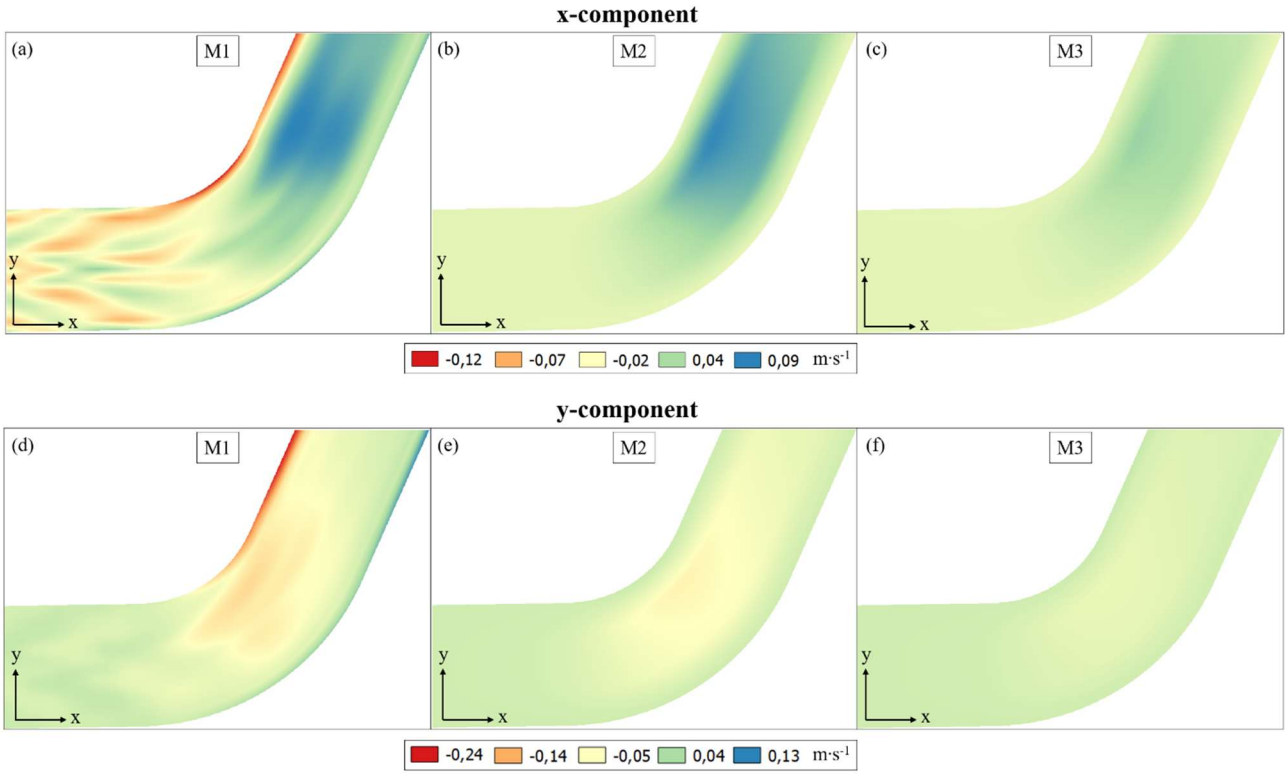

Figure 4.5 Maps of the velocity variation due to simulation of secondary current effects with respect to the model without any correction; reported as velocity components in x- (panels a, b, and c) and y-directions (panels d, e, and f). The presented variation expresses the difference between the surface velocity obtained by simulations of implemented methods (M1, M2, and M3) and the mean flow velocity of the model without secondary current effects.

Despite the best performance was determined for M1 (see Tab.4.2), the simulated surface velocity pattern obtained with M1 presented fluctuations (see Figs 4.5a and 4.5d) that influenced the hydraulics in the curve. These fluctuations were not observed during the experiments execution, thus method M2 was chosen for simulating dowel-experiments, as it showed similar performances than M1 (i.e., all the following results were obtained applying M2).

Figures 4.6 and 4.7 show the LW trajectory results of dowel-experiments simulated with Iber-Wood considering the effect of secondary currents. The observed trajectories from inlet points I_1 and I_2 (see Fig. 3.1b) showed a deviation of dowels once entered in the curve, in fact, travelling along the curve dowels were pushed to the outer wall of the channel by the presence of secondary currents. While the deviation was lower for I_3 because, in this case, dowels were interacting with the outer wall of the channel while moving downstream, bumping, or sliding on that. The dowel deviation was simulated by the implemented method for all the considered inlet points and both initial dowel orientation, parallel (Fig. 4.6a) and perpendicular (Fig. 4.6b). The similarity between observed and simulated trajectories is expressed by the C_{sim} values (Fig. 4.6c), the higher values of C_{sim} were obtained for the two experiments conducted from I_1, in particular for the experimental configuration perpendicular to the channel axis resulted the worst. The two runs from I_2 obtained

similar C_{sim}, 0.013 and 0.014 for parallel and perpendicular orientation, respectively. Finally, a good agreement was obtained for I_3, especially considering the orientation perpendicular for which the observed and simulated trajectories are mostly overlapped (Fig. 4.6b) and the resulting C_{sim} was the lowest (Fig. 4.6c).

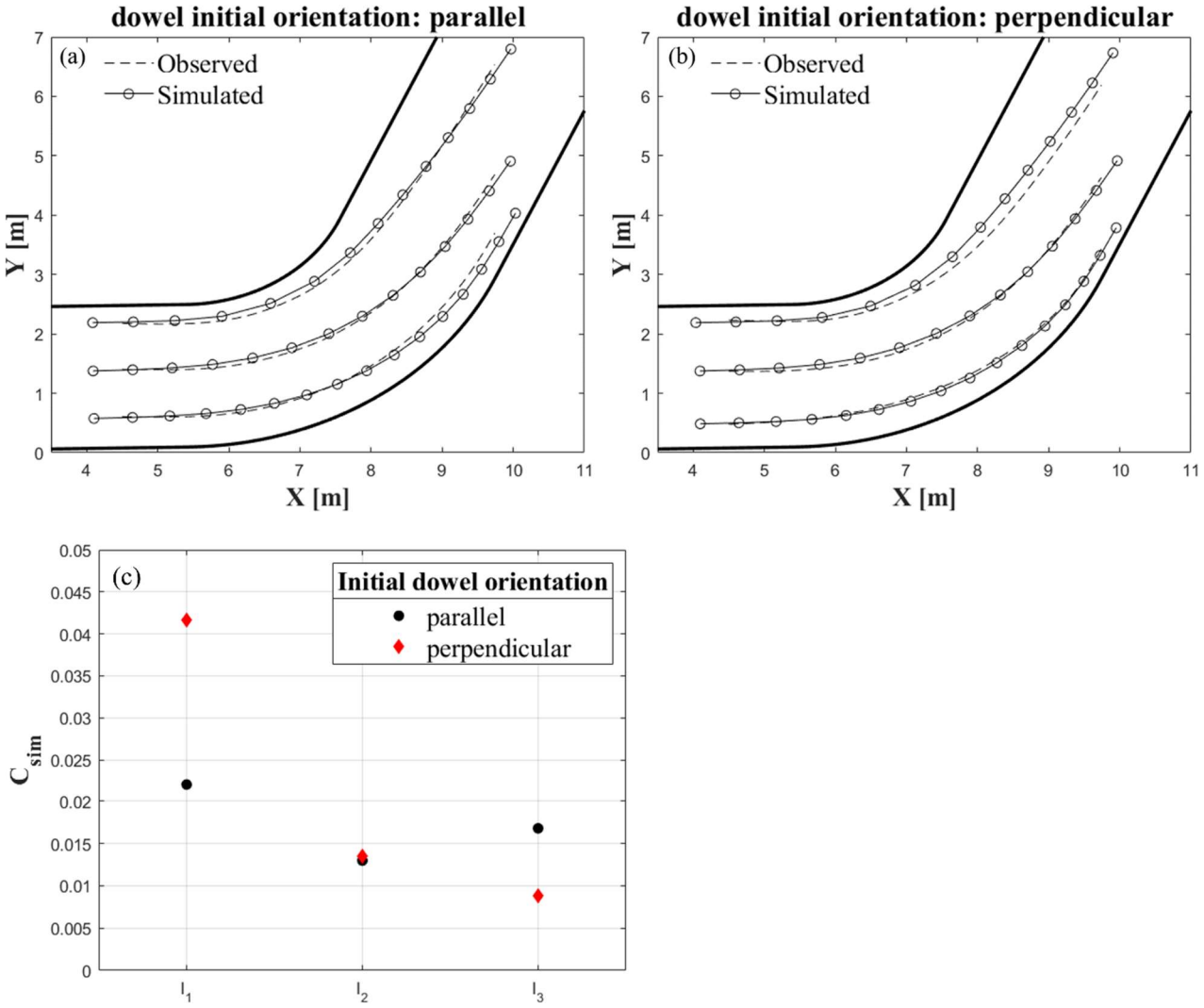

Figure 4.6 Comparison between observed and simulated trajectories considering different dowel inlet points and dowel orientations (a, b) and the corresponding C_{sim} values (c). Three wood pieces parallel (a) and perpendicular (b) to the flow entered the channel at 0.25 m from the left wall (I_1), in the middle (I_2), and at 0.25 m from the right wall (I_3). Simulations were performed using the model present in section 4.2.2. All trajectories are related to the dowel center of mass.

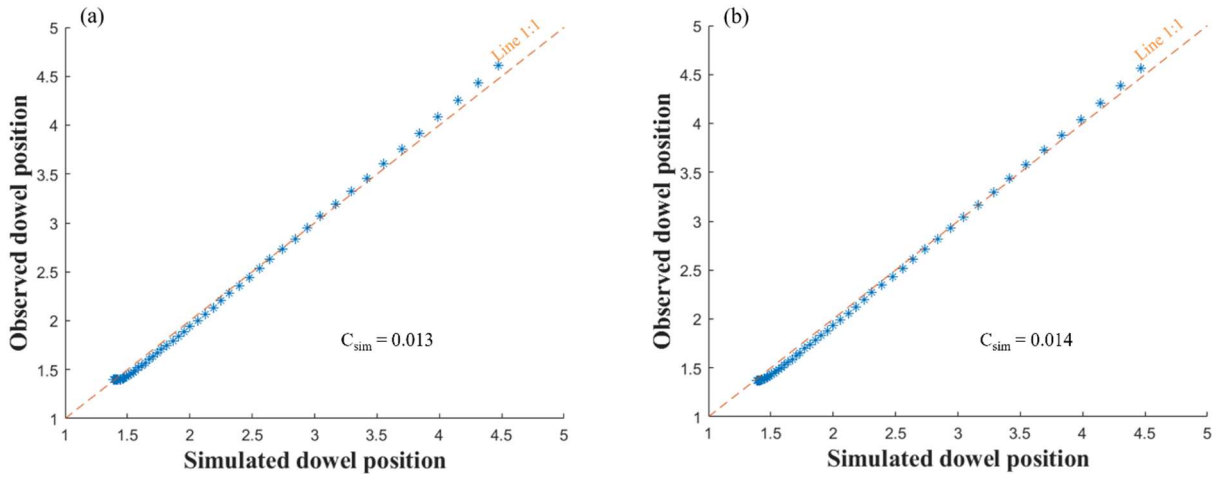

Figure 4.7 Observed and simulated dowel position for experiments from I_2 with initial dowel orientations parallel (a) and perpendicular (b). The C_{sim} is the similarity coefficient, Eq. 4-29.

4.4 Discussion

An existing 2D depth-averaged hydrodynamic numerical model has been implemented to simulate effects of secondary currents at the water surface, and, as a result, to predict and simulate wood transport in river bends. Methodologies for including secondary current effects in Iber have been defined in order to introduce the fewest number of new parameters in the model, thus, decreasing uncertainty while validating the model.

The accuracy in reproducing the hydrodynamics of the flume was tested by simulating the experimental setup specifically designed and carried out for achieving the objectives of the present research (illustrated in chapter 3). Although the hydraulic models were calibrated, deviations were observed between simulations and measurements. The reasons for the obtained differences are several. Firstly, a pure 3D phenomenon as secondary currents cannot be entirely reproduced by a two-dimensional model. Another reason is connected to the instrumentation used for collecting velocity data in the laboratory that did not allow to take measures of the water surface velocity.

The three implemented methods (M1, M2, and M3) performed similarly in reproducing the experimental setup (see Tabs 4.2), moreover, the result was comparable to the solution of the model without any correction in terms of water depth, as shown in Fig. 4.3. On the contrary, the effect of the implementation was highlighted in the surface velocity results as the velocity components changed due to the simulation of secondary current effects. Even more marked was the effect on wood trajectories, which were much more similar to the experimental ones than those simulated using the model without any correction (Figs 4.1, 4.6, and 4.7).

The Leichtweiß Institute experiments were simulated in order to observe the effect of the presented methods on the wood trajectories. Simulation of secondary current effects provided good results for dowel-experiments as the similarity between observed and simulated wood trajectories strongly increased (see Figs 4.1, 4.6 and 4.7). In fact, as showed in Fig. 4.1, the simulated trajectory for the model without any correction was following the flow streamlines resulting quite far from the observed trajectory and maintaining about the same distances from the lateral walls along the channel.

Numerical results highlighted the role of the gradient of the correction term (Δc) and of the adaptation length (λ) in the implemented methods. As shown in Figs 4.2, the correction of velocity vector directions was not uniform along the cross-section, but it increased moving from lateral walls to the center of the channel. As a result, the cross-section was characterized by a central region, that covers a large part of the channel width, in which the helical motion develops (Blanckaert & de Vriend, 2004). The introduction of the correction term improved the definition of the deviation angle (δ) provided by Vasquez et al. (2005), see Eq. 2-15. In fact, the introduction of c in Eqs 4-11 and 4-28 prevents vectors from being directed outward from the channel for cells in mesh cells close to channel walls. The value of Δc in simulating dowel-experiments was firstly set according to the gradient of velocity in transverse direction, then it was calibrated on the observed dowel trajectories. The streamwise lag-effect on the secondary current equilibrium, modelled with the equation proposed by Jagers (2003), was clearly represented by the simulation of dowel-experiments (see Figs 4.1, 4.6, and 4.7). The

adaptation of the flow to the curvature change was modelled by setting the values of λ_{gen} and λ_{rel} because the application of Eq. 2-13 showed an overestimation of the driftwood along the curve (see Fig. 4.1b).

4.5 Conclusion

The main goal of the present part of the research was the simulation of secondary currents effects on wood transport in the existing model Iber-Wood. The capacity of the implemented methodologies to accurately reproducing the trajectories of floating wood pieces was tested by simulating flume experiments presented in chapter 3. The good agreement between simulated and observed trajectories in a sharply bend substantiates the validity of the proposed approach.

Here, the secondary current effects on the hydraulics were highlighted by comparing results of the three proposed methodologies with the results of the model without any correction. In simulating the two experimental setups no significant differences were observed in reproducing the water depth along the channel bend for the four considered methods. This evidence highlighted how small were the secondary current terms compared to the hydrodynamics of the channel. Similar results were obtained while considering the magnitude of the surface velocity. On the contrary, the surface velocity components have been changed by the introduced methodologies, which was the desired result in order to reproduce secondary current effects on the surface.

The implemented correction of the velocity vectors direction at the surface together with the transport-type equation used for calculating the secondary current intensity increased the accuracy in simulating the wood trajectories. The simulated dowel trajectories obtained using the model without any correction did not accurately reproduce the observed trajectories, while the progressively drift of dowels through the outer wall of the channel was simulated by using the implemented methodologies.

Although simplifications adopted in the implementation and knowing that further study is needed to better simulate the complexity of natural rivers, this methodology constitutes at present the first attempt to incorporate secondary current effects in a 2D depth-averaged model for simulating the transport of LW in curved channels. Future application of the methods will allow to improve the methodologies and investigate opening challenges for different purposes, as LW management and flood risk prevention.

Chapter 5

Case study: simulation of wood transport in a tight bend in the Versilia River during the flood event of June 19, 1996

5.1 Introduction

In this chapter the methodologies presented in chapter 4 are applied in order to simulate a real flood event with the aim to test the applicability of the proposed enhanced version of Iber-Wood model (Ruiz-Villanueva et al., 2014a) to a river-scale geometry. The flood event that occurred in the Versilia River (Italy) on 19 June 1996 was selected as a huge quantity of wood was transported by the flow in a tight bend having a curvature ratio of 1.7. Also, the extreme flood condition and the presence of LW caused the formation of a breach in the outer bank of the S. Bartolomeo bend, close to the town of Pietrasanta (Italy) in the lowland part of the Versilia River basin (Fig. 5.1). According to the thesis objectives, the focus of this application was the simulation of LW during the flood event, while the breach formation was modelled with an existing tool of Iber, and so, results are presented only considering the wood trajectories.

Figure 5.1 The flooding caused by the levee breach on 19 June 1996 formed along the Versilia River close to the town of Pietrasanta (source: http://www.neteservice.it/ilfiumeversilia/alluvione_Versilia96.htm).

The selected flood event was firstly studied by Paris & Settesoldi (1999) that provided a 1D model for the characterization of the breach formation. The authors reconstructed the flooding by deriving the incoming flow hydrograph and the outflow volume of water from the breach. This study represented the reference conditions for calibrating the present numerical model. LW transport was simulated and compared with available multimedia proofs, i.e., videos and photographs found online.

The chapter is organized as follows: the study area and the flood description are firstly presented (section 5.2); then, the description of the model is provided (section 5.3); the results of the simulation are presented by comparing numerical results with the study of Paris & Settesoldi (1999) and with available multimedia proofs (section 5.4); finally, conclusion are presented (section 5.5).

5.2 Study area and 1996 flood description

The study area is located in Italy (south Europe) close to the border between Tuscany and Liguria regions. The Versilia River (Fig. 5.2) has a mountain catchment located in the western side of the Apuan Alps, it covers an area of about 115 km^2 and the altitude range is 425 m a.s.l., while maximum and minimum elevations are 1676 and 0.46 m a.s.l., respectively. The catchment is mainly characterized by forests with the exception of the lowland reach, close to the Mediterranean Sea, in which there are numerous inhabited centers. The study reach, located in the lowland part of the catchment close to the town of Pietrasanta (see Fig. 5.2), is 1.3 km long and has an average slope of 1.2 ‰. This reach is characterized by the presence of a right curve of about 90° called S. Bartolomeo bend, with a curvature radius of 128 m (regarding the centerline) and a channel width of 75 m, resulting in a curvature ratio of 1.7. The flood event occurred on June 19th, 1996, induced the collapse of the outer levee at the S. Bartolomeo bend that resulted in a breach formation (see Fig. 5.1). The breach developed rapidly (in about 40 minutes) and reached a final length of 70 m, the embankment was eroded down to the level of the riverbed. Table 5.1 shows the main characteristics of the river basin and the studied reach.

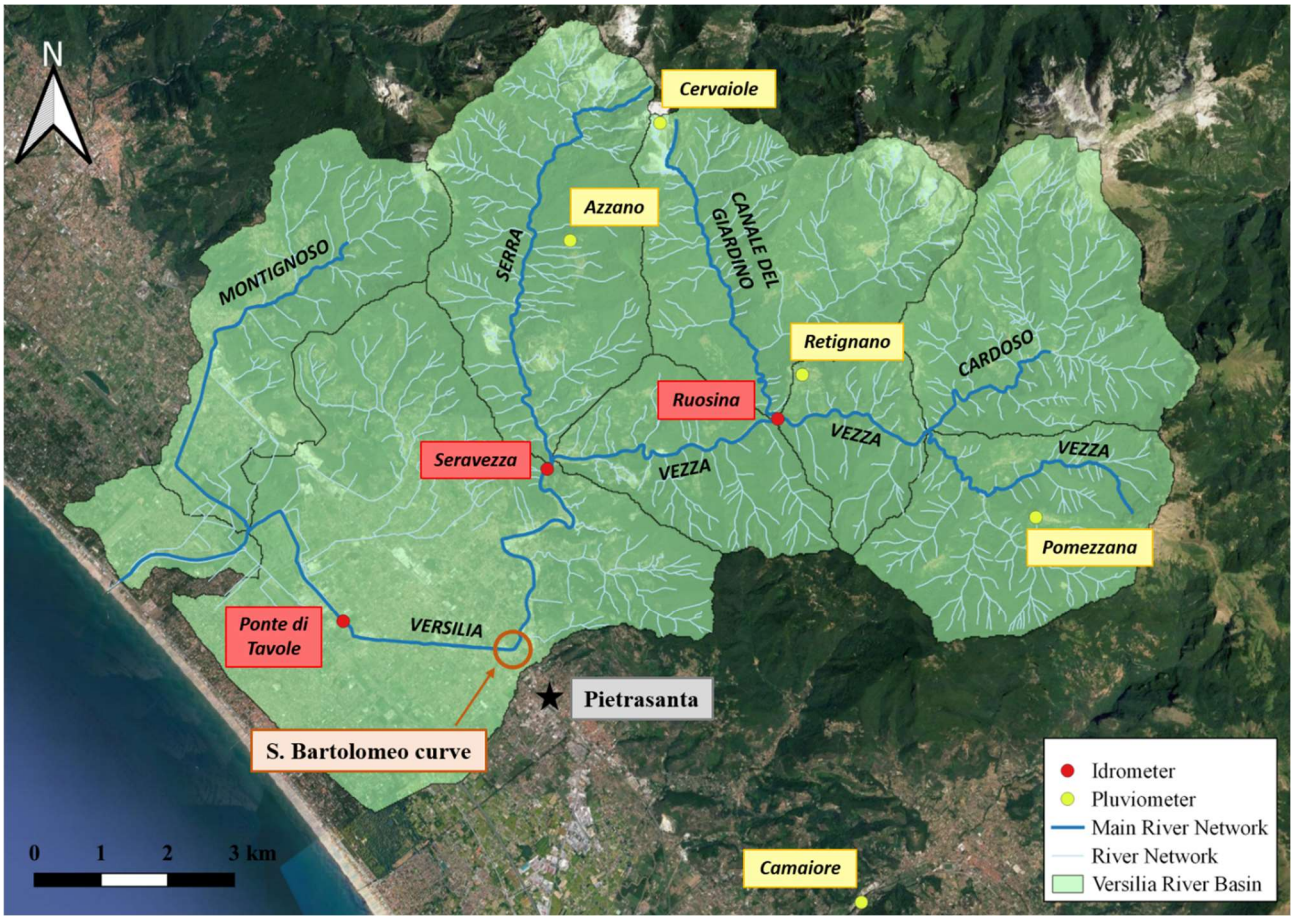

Figure 5.2 Versilia River basin and hydrographic network. Installed hydrometers and pluviometers are reported, and the S. Bartolomeo curve is highlighted (in brownish color).

Table 5.1 Main characteristics of the Versilia catchment and the studied reach.

Drainage area	115 km^2
Length of the main channel	23 km
Average basin altitude	425 m a.s.l.
Minimum basin elevation	0.46 m a.s.l.
Maximum basin elevation	1676 m a.s.l.
Length of the studied reach	1.3 km
River width at the S. Bartolomeo bend	75 m
Radius of curvature of the S. Bartolomeo bend	128 m
Curvature ratio	1.7
Minimum studied reach elevation	12.9 m a.s.l.
Maximum studied reach elevation	14.54 m a.s.l.
Studied reach bed slope	0.0012

Torrential rainfall events usually occur in autumn and winter, resulting in abundant surface runoff and sediment mobilization, in particular in the mountain area of the basin. Contrarily, the lowland reach is characterized by low floods especially during the summer in which the riverbed can also be completely drained as only subsurface flow occurs.

The flood event of 1996 was generated by an extremely rapid rainfall that affected the mountainous part of the catchment area. The western side of the Apuan Alps has been affected by rain since the early hours of the day with characteristics of flash events. Two main rainfall were registered during the day, the first one in the early morning (from 5 a.m. to 8 a.m.) and the second one during the morning (from 10 a.m. to 13 p.m.), that generated two consecutive flash floods. Table 5.2 shows the Pluviometric measurements recorded by rain gauges presented in the area, is important to notice how different were measurements from instruments located on the mountains (Pomezzana, Retignano, Cervaiole and Azzano) and instruments located near the sea (Camaiore, Torre del Lago and Viareggio); see Fig. 5.2 for the location of rain gauges. The hydrometers

installed along the river corridor registered the data of the first flood than they were swept away by the current in the first hour of the second flood, so the flow hydrograph was not measured for the second flood event.

Table 5.2 Pluviometric measurements of 19 June 1996; values are in millimeters.

Rain gauge name	1 h	3 h	6 h	12 h	24 h
Pomezzana	-	320	390	474	478
Retignano	78	165	214	387	400
Cervaiole	67	126	182	230	245
Azzano	61	144	183	242	260
Camaiore	27	29	38	47	53
Torre del Lago	1	1	1	1	1
Viareggio	7	9	9	11	11

The chronological description of the flash flood event is as follows: the intense rainfall on the first morning resulted in an abundant surface runoff which caused profound disruptions in the slopes and in the hydrographic network, resulting in the saturation of the soil. The situation in the mountain subbasins was exacerbated by the second rainfall for which the intense rain rapidly generated a second flood event, as the ground was waterlogged. At this time, numerous landslides have been observed in the upper part of the basin introducing a huge amount of soil and wood in the river network. The fallen trees were quickly curtailed, their branches and roots were detached from the trunks due to the violent collisions that occurred in the river corridor. The flood hydrographs reached, especially in mountain subbasins, absolutely exceptional peak values (estimated return times in the order of 300 years) with solid transport concentrations at the limits of saturation values. In lowland reaches, the over-flooding, and the huge amount of transported wood pieces (Fig. 5.3c) compromised the river channel conveyance capacity. Areas close to the watercourse were locally flooded already during the first flood event, but the second flood wave caused the greatest damages to buildings and infrastructures. In particular, the breach of S. Bartolomeo curve caused the inundation of Pietrasanta town and surrounding areas, also affecting the railway line (Figs 5.3a and 5.3b) and the highway (Fig. 5.3d) which are located downstream of the curve.

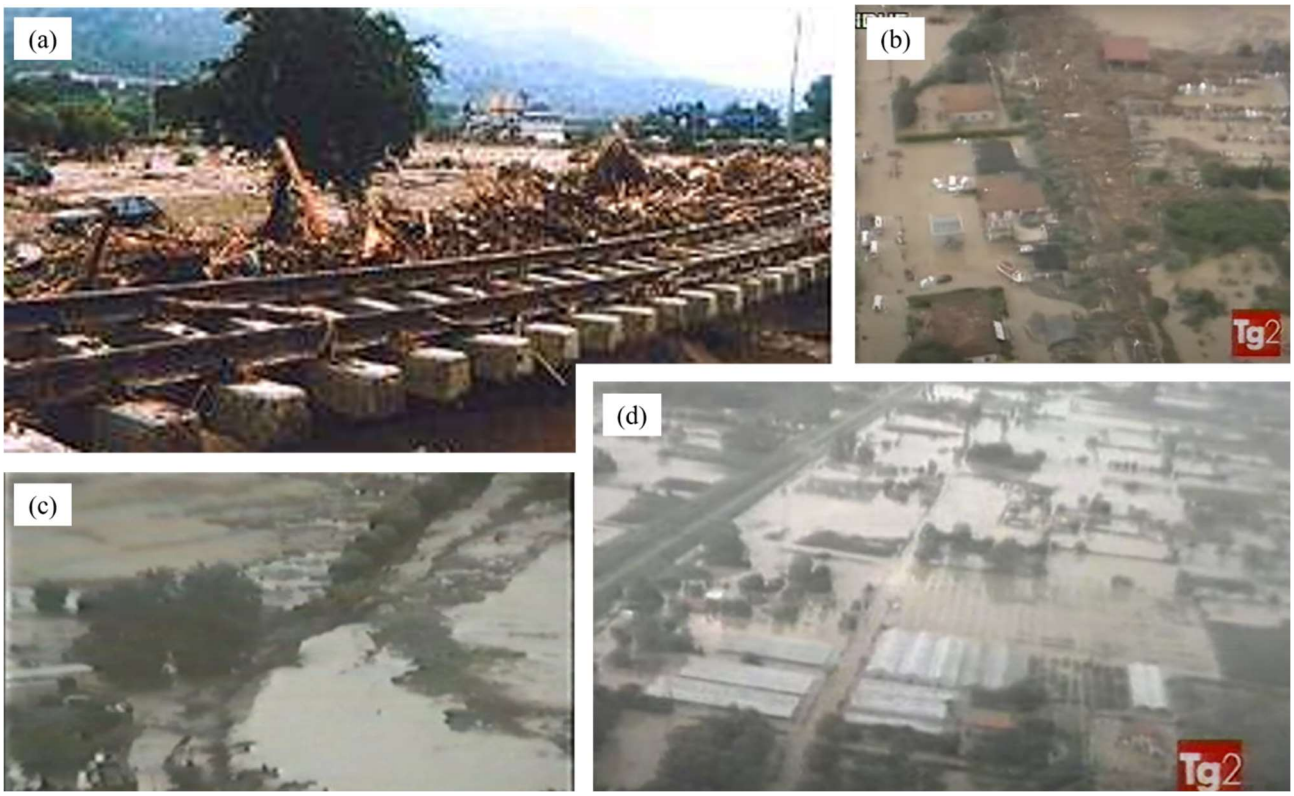

Figure 5.3 Images of the flooding around the town of Pietrasanta. The beginning of the breach formation (c), the damages to the railway line (a and b), and to the highway (d) (sources: www.neteservice.it/ilfiumeversilia/alluvione_Versilia96.htm and www.youtube.com/watch?v=Ccvt6IuhQ90).

Paris & Settesoldi (1999) conducted a study on the characterization of the breach formation at the S. Bartolomeo curve. Their results are showed in Fig. 5.4 in which the reconstructed flow hydrograph upstream of the curve is compared with the flow hydrograph of the flow through the breach and the flow hydrograph downstream. The breach formed during the second flood event and was characterized by a peak of about 570 $m^3 s^{-1}$.

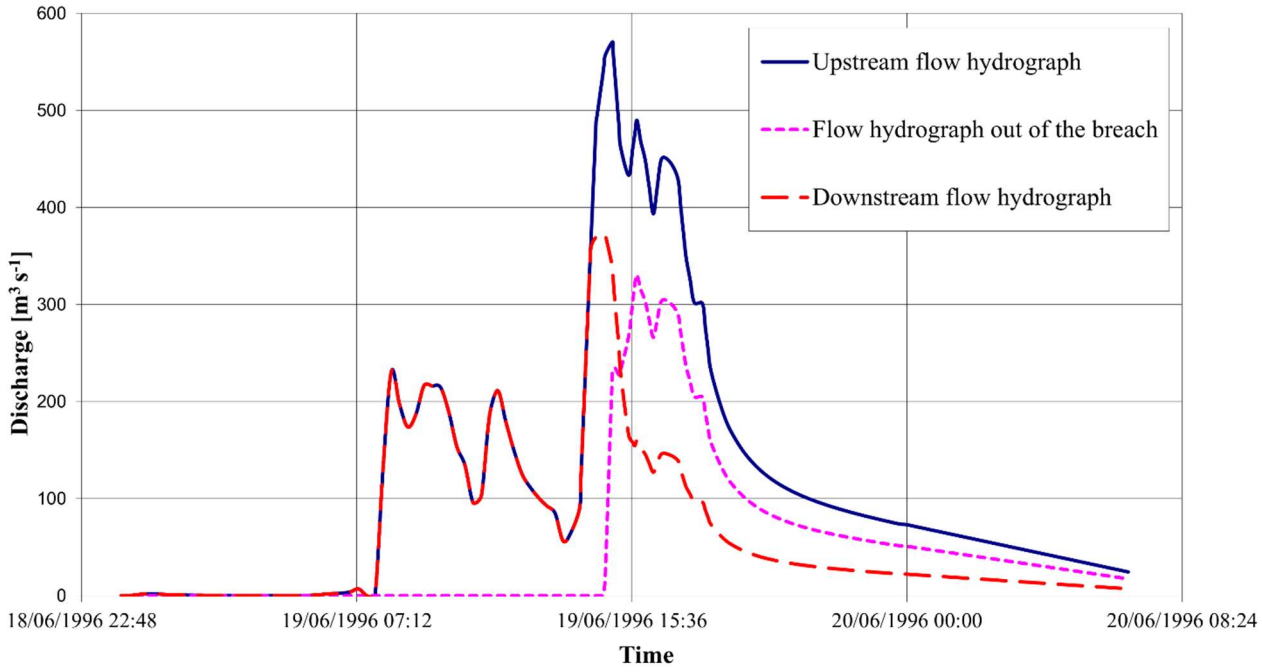

Figure 5.4 Reconstructed flow hydrographs (Paris & Settesoldi, 1999). Upstream and downstream refer to the S. Bartolomeo bend.

5.3 Methodology

The simulation of the flood event was conducted by using the model Iber-Wood with the implementation of secondary current effects (as presented in chapter 4). In order to numerically reproduce the flood event at the study site, firstly the mesh was generated to properly reproduce the area of interest. Once the geometry was generated, the hydrodynamics boundary conditions were defined, and the model calibration was carried out varying the roughness coefficient and by comparing numerical results with the flow hydrographs provided by Paris & Settesoldi (1999) (see Fig. 5.4). Finally, the large wood simulation was performed. These steps are presented below.

Mesh generation

A 2D unstructured irregular triangular mesh was generated for simulating the flow into the river corridor and the flooding of areas close to the S. Bartolomeo bend. The geometry of the river corridor was partly known by a survey conducted by Eng. David Settesoldi during the 1996 (before and after the flood event) that provided 12 channel cross-sections in the study reach. In addition, the Digital Terrain Model (DTM) of the area of interest was available from the Tuscany Region with a resolution of 1 m (survey carried out in years 2008 – 2010, available at: https://www.regione.toscana.it/-/geoscopio). This information was elaborated and corrected by observing several images and videos of the flood event found online. The final mesh considered, in addition to the 1.3 km of the study reach, an area of about 0.4 km^2 that partly covered the inundated areas, in particular the area at the outer side of the curve where the city of Pietrasanta is located.

As already mentioned in the introduction, the breach formation was modelled using an existing tool of Iber. This tool allows to define the shape and other properties of the breach formation process, as a result, the mesh is deformed during the simulation in order to reproduce the evolution of the breach. The breach characterization is not reported in this chapter as it was not the focus of the simulation, however, a description of the tool is given in Appendix E.

Figure 5.5 shows the resulting mesh around the S. Bartolomeo curve. The cell size was not set uniformly for the entire mesh, but the mesh was divided into uniform areas (with similar land use characteristics) and the maximum cell size was defined for each. In addition, particular attention was paid to the external levee of the S. Bartolomeo curve, the one affected by the breach. The maximum cell size adopted for the mesh generation are summarized in Tab. 5.3.

Table 5.3 Maximum cell size adopted for the mesh generation.

Area	Max. cell size [m^2]
Main channel	5
Floodplain	5
Agricultural field	10
Industrial area	10
Residential area	20
Outer levee of S. Bartolomeo curve	2

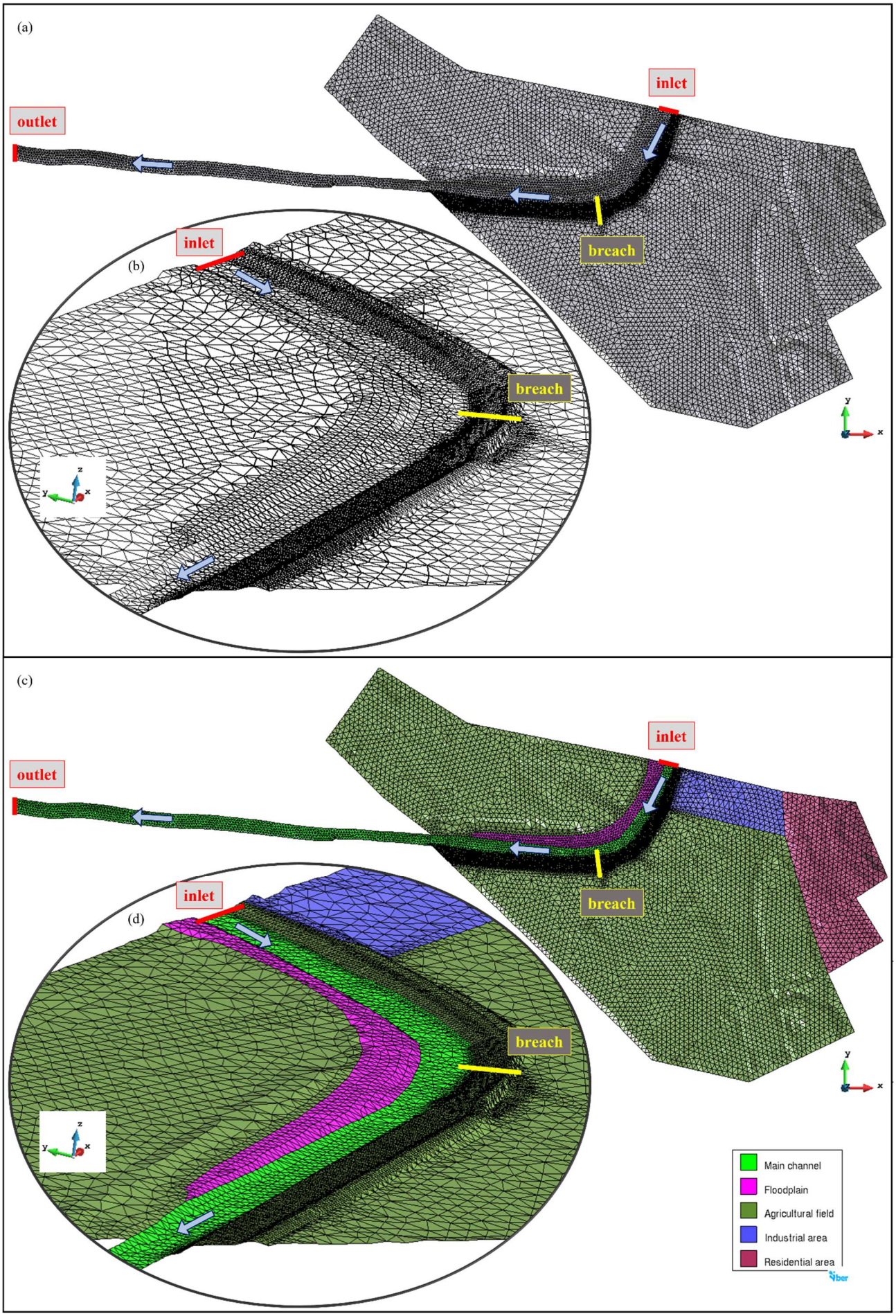
(a)
inlet
outlet
breach
(b)
inlet
breach
(c)
inlet
outlet
breach
(d)
inlet
breach
Main channel
Floodplain
Agricultural field
Industrial area
Residential area

Figure 5.5 Mesh overview. Top views (a and c) and 3D representations (b and d) of the 2D unstructured triangular mesh. The defined uniform zones of the mesh are presented in panels c and d.

Hydrodynamics boundary conditions

The hydrodynamics boundary conditions were set according the study of Paris & Settesoldi (1999). The upstream boundary condition was set equal to the flow hydrograph presented in Fig. 5.4, in particular, simulating the flow of the two floods, i.e., from the 6:45 a.m. to the 9:00 p.m. of the 19 June (Fig. 5.6). The downstream boundary condition was set at the end of the study reach by applying the condition of uniform flow; importantly, this condition is located further downstream from the curve in order to avoid influences on the hydrodynamics at the S. Bartolomeo bend. In addition, a second outlet for the flow was defined on the model boundaries in proximity of Pietrasanta in order to allow the water flow out of the mesh domain after the breach formation.

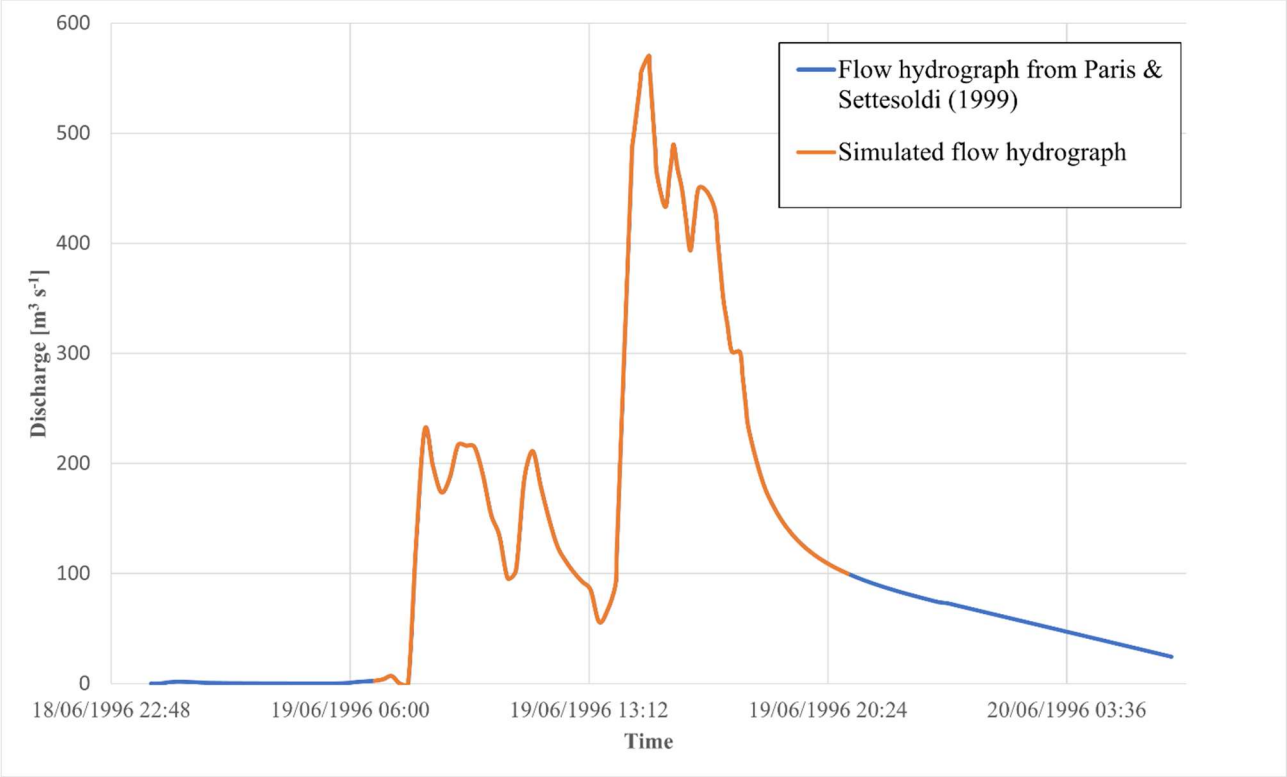

Figure 5.6 Simulated flow hydrograph.

Model calibration

The model calibration was carried out by varying the roughness coefficient and comparing numerical results with the flow hydrographs shown in Fig. 5.4 (Paris & Settesoldi, 1999). In particular, the calibration was performed by considering the first flood, i.e., before the breach formation. A different Manning coefficient was selected for each of the five selected uniform zones (see Tab. 5.3 and Fig. 5.5), the final coefficients are reported in Tab. 5.4.

Table 5.4 Adopted roughness coefficients (Manning) for each of the five selected uniform zones.

Area	Manning coefficient [$m^{1/3} \cdot s^{-1}$]
Main channel	0.03
Floodplain	0.035
Agricultural field	0.05
Industrial area	0.10
Residential area	0.15

Large wood boundary conditions

A huge amount of large wood mobilized during the flood event was clearly visible from numerous sources (partially presented in Fig. 5.3), unfortunately the wood flux was not characterized in the field (in terms of dimensions, quantity, and density). However, on the basis of visual observations and with the collaboration of Prof. Eng. Enio Paris an accurate characterization of the wooden material was possible.

The wood flux used as the upstream boundary condition for the introduction of wood elements in the model is shown in Fig. 5.7. This wood flux, applied at the water inlet section, was defined on visual evidence (such as that of Prof. Eng. Enio Paris) and on multimedia proofs, as no further data were available. So, as large wood entered the main river corridor whit the second flood event the wood flux during the first flood wave was considered negligible and set equal to zero. The wood flux was rapidly increased along the rising limb of the second wave, reaching a value of 10 pieces per minute (see Fig. 5.7), estimated by videos. Then, the wood flux was progressively reduced in the falling limb of the hydrograph. All the wood elements were introduced in the model with varying dimensions (i.e., diameter and length), density and initial orientation. As the wood was introduced in a straight reach all the elements were considered mostly parallel to the flow direction, so their

initial orientation was considered in the range 0° ÷ 30°. Finally, the drag coefficient was set variable during the simulation with the wood piece orientation (θ) according with Eq. 3-5. Table 5.5 reports all the wood data adopted in the model for the characterization of the wood pieces.

Table 5.5 Large wood characteristics.

Minimum diameter	0.05 m
Maximum diameter	0.3 m
Minimum length	0.5 m
Maximum length	20 m
Minimum density	700 kg/m^3
Maximum density	800 kg/m^3
Wood initial orientation	0° ÷ 30°
Drag coefficient	variable with θ

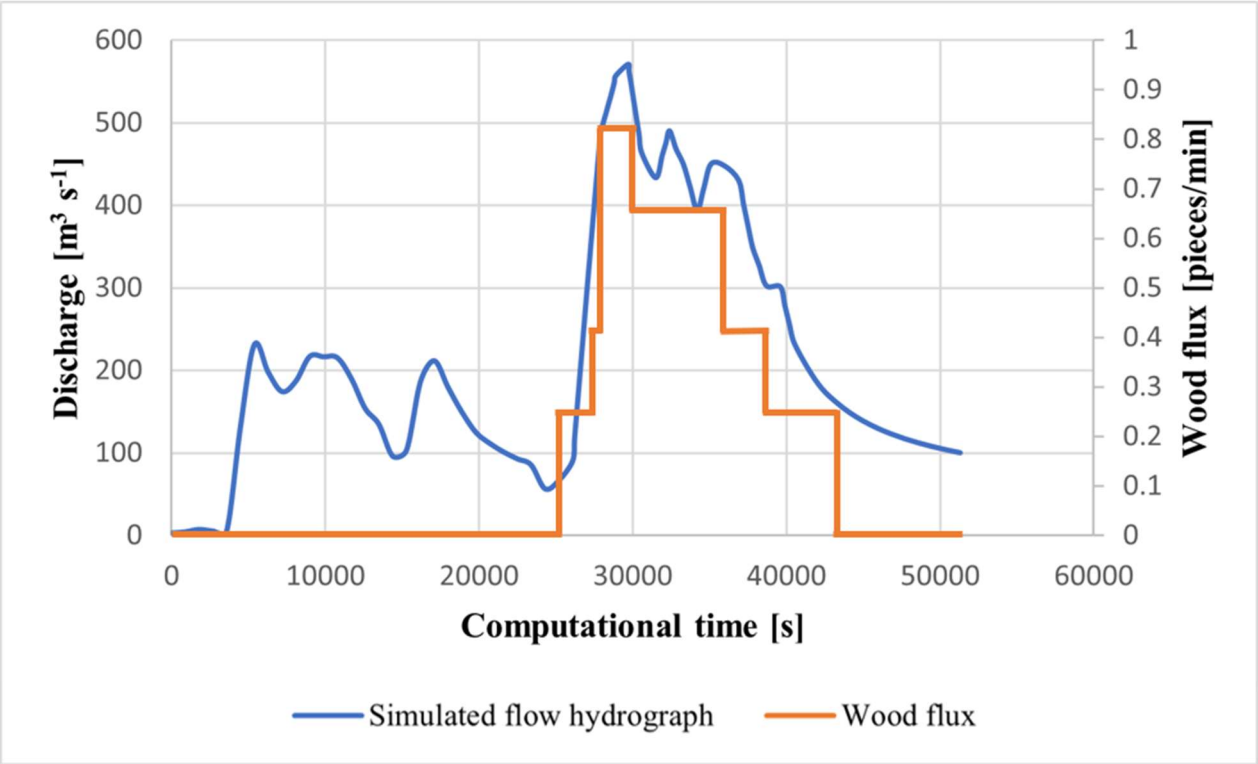

Figure 5.7 Simulated wood flux.

5.4 Results

In Fig. 5.8 the numerical results are compared with the data from Paris & Settesoldi (1999). Figure 5.8a shows the flow hydrograph downstream of the S. Bartolomeo bend, while Fig. 5.8b shows the flow hydrograph out of the breach. As stated above, the calibration of the model has been conducted considering only the flow data before the formation of the breach (see Fig. 5.8a), for which a RMSE of 3.5 $m^3 \cdot s^{-1}$ was calculated.

The result of the model slightly underestimates the flow through the breach (see Fig. 5.8b), even if it reproduces its trend over time. In particular, a delay can be observed in reaching the maximum flow rates, this could be due to a different modeling of the breach formation. Moreover, the flow underestimation is greater for discharges higher than 275 $m^3 s^{-1}$, while in the falling limb results are comparable with Paris & Settesoldi (1999). Similar observations can be extracted for the downstream flow (see Fig. 5.8a) after the breach formation, although in this case the differences between the two graphs are minor. The differences observed in Fig. 5.8 can be attributed to the approach used by Paris & Settesoldi (1999) that considered the breach as the only lateral point outflow source from which the flow exited from the river corridor, while this was true from simulation results.

Due to the non-negligible differences observed between numerical results and results from Paris & Settesoldi (1999), and because the simulation of the breach was not in the focus of this work, in the following, exclusively results of the simulation before the breach formation will be presented.

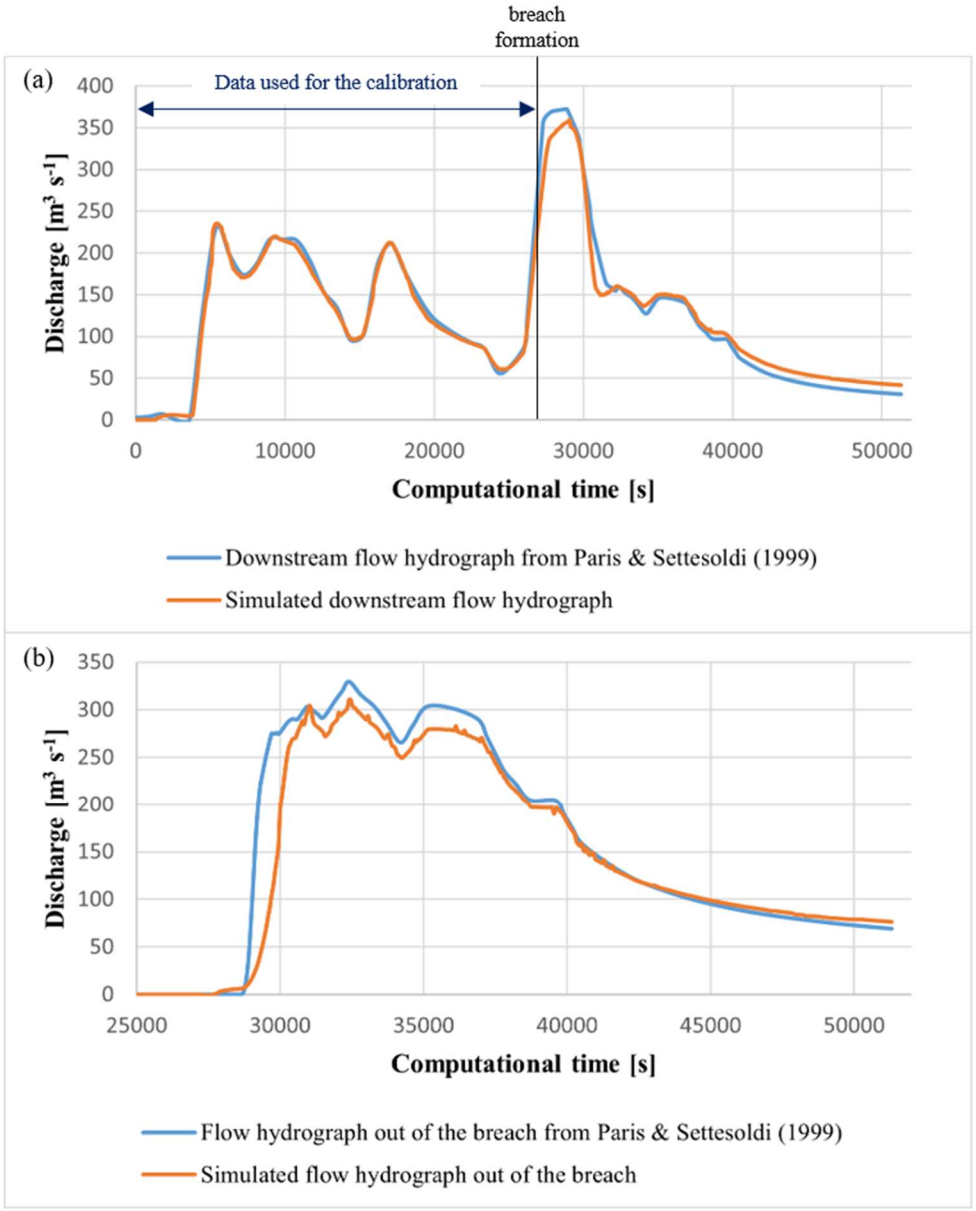

Figure 5.8 Comparison between numerical results and results from Paris & Settesoldi (1999) for the downstream flow (a) and the discharge through the breach (b). The data used for the calibration of the model are highlighted in panel a.

Figures 5.9 and 5.10 show the flood evolution, in terms of water depth, during the simulation of the first flood event; the background image used in these four pictures is not representative of the 1996 riverbed geometry but represents the current riverbed geometry (background image source: www.bing.com/maps).

Figure 5.9 reports the numerical solution for the timestep 10800 s which correspond to the passage of the first flood wave. At this timestep, the flow was completely contained into the riverbed, no overflows were observed; however, in few points the flow reached the top of the embankments on both riverbanks. Highest water depth was observed in the upstream area of the railway line bridge, downstream of the S. Bartolomeo curve, that caused a backwater rise. The simulated water depth at the end of the first flood peak event is shown in Fig. 5.10

(timestep 24300 s), as expected the water depth decreased along the entire reach. Again, as observed in Fig. 5.9, the highest water depth values were observed at the upstream section of the railway line bridge.

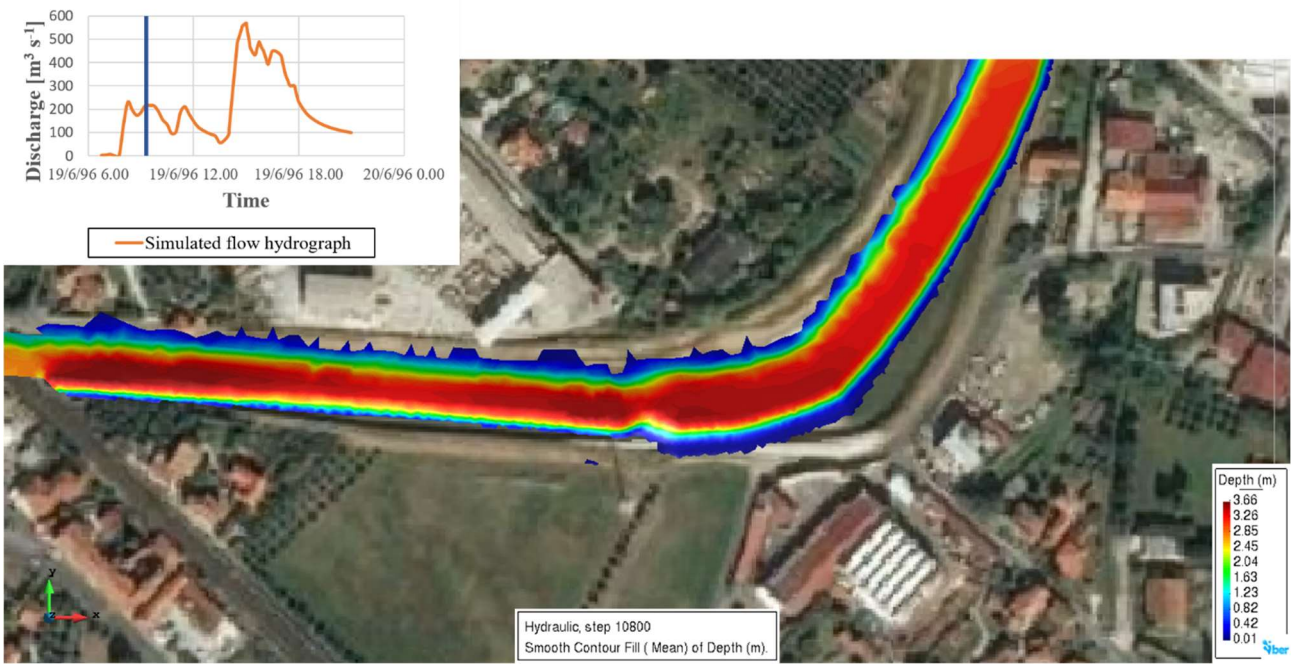

Figure 5.9 Maps of the simulated water depth during the first flood event (timestep: 10800 s).

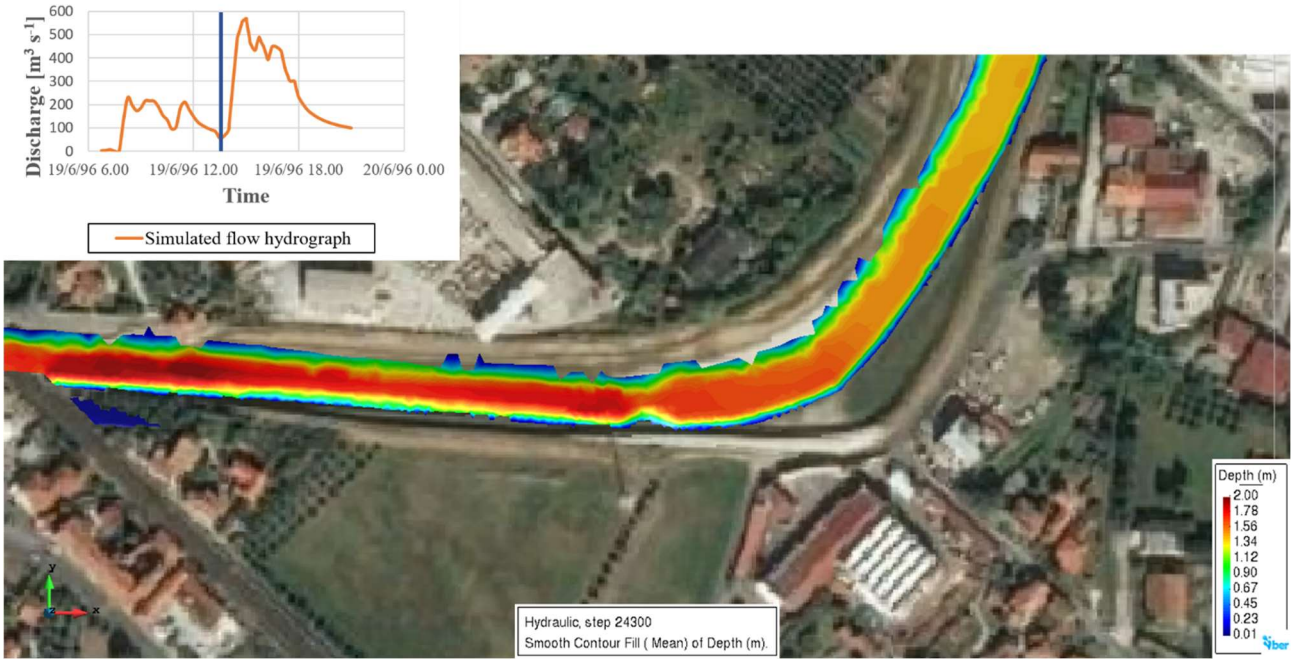

Figure 5.10 Maps of the simulated water depth at the end of the first flood event (timestep: 24300 s).

Figure 5.11 shows the comparison between simulated and observed LW trajectories. The latter are presented by a shade area that is representative of the area occupied by wood flux during the flood event, and by the mean observed wood trajectory. The simulated trajectories are presented for both the model with secondary current effects, and the model without any correction; moreover, for illustration purposes, these are referred to only three elements named LW1, LW2, and LW3, respectively. LW1 – 3 were chosen considering their inlet position and orientation that are the same in both showed simulations. Furthermore, the background map represents the water depth that was assumed as characteristic for the entire evolution of the LW trajectories.

The wood pieces, during the flood event, approached the bend at the center of the channel and then drifted towards the outer bank while travelling along the curve (see Fig. 5.11), their trajectories were affected in most of the cases by interactions with the riverbank that reduced the wood velocities and influenced their orientation. The enhanced version of Iber-Wood (i.e., considering secondary current effects as described in chapter 4) globally reproduced the observed dynamics, while, on the contrary, the trajectories obtained using the model without any correction strongly differ from observation, as the wood elements traveled along the bend without drifting to the outer bank. The performances of the two models are measured by calculating the coefficient of similarity C_{sim}, Fig. 5.12a reports the comparison between simulated trajectories, the trajectory observed with the model without any correction and the trajectory observed with the enhanced model, for the same wood piece (LW 1, LW 2, and LW 3), while Fig. 5.12b reports the comparison between the mean observed trajectory and the simulated trajectories for LW 2. The results obtained with the model without any correction (Fig. 5.12a) differs from the results obtained simulating secondary current effects by more than the 20%. This is reflected by the comparison with the mean observed trajectory (Fig. 5.12b), for the case of LW 2 the difference between the two performed models is highlighted by a C_{sim} of about 0.25 measured for the model without any correction and a C_{sim} of about 0.035 for the enhanced model.

The enhanced Iber-Wood model allowed to simulate the wood drifting from the beginning of the bend, and, even if characterized by different approaching positions to the curve, interacted with the outer bank in the same area, i.e., in the final part of the curve, then continued their motion downstream. As a result, the simulated wood flux agrees with the observed one much more than that obtained with the model without any correction (see Fig. 5.12b).

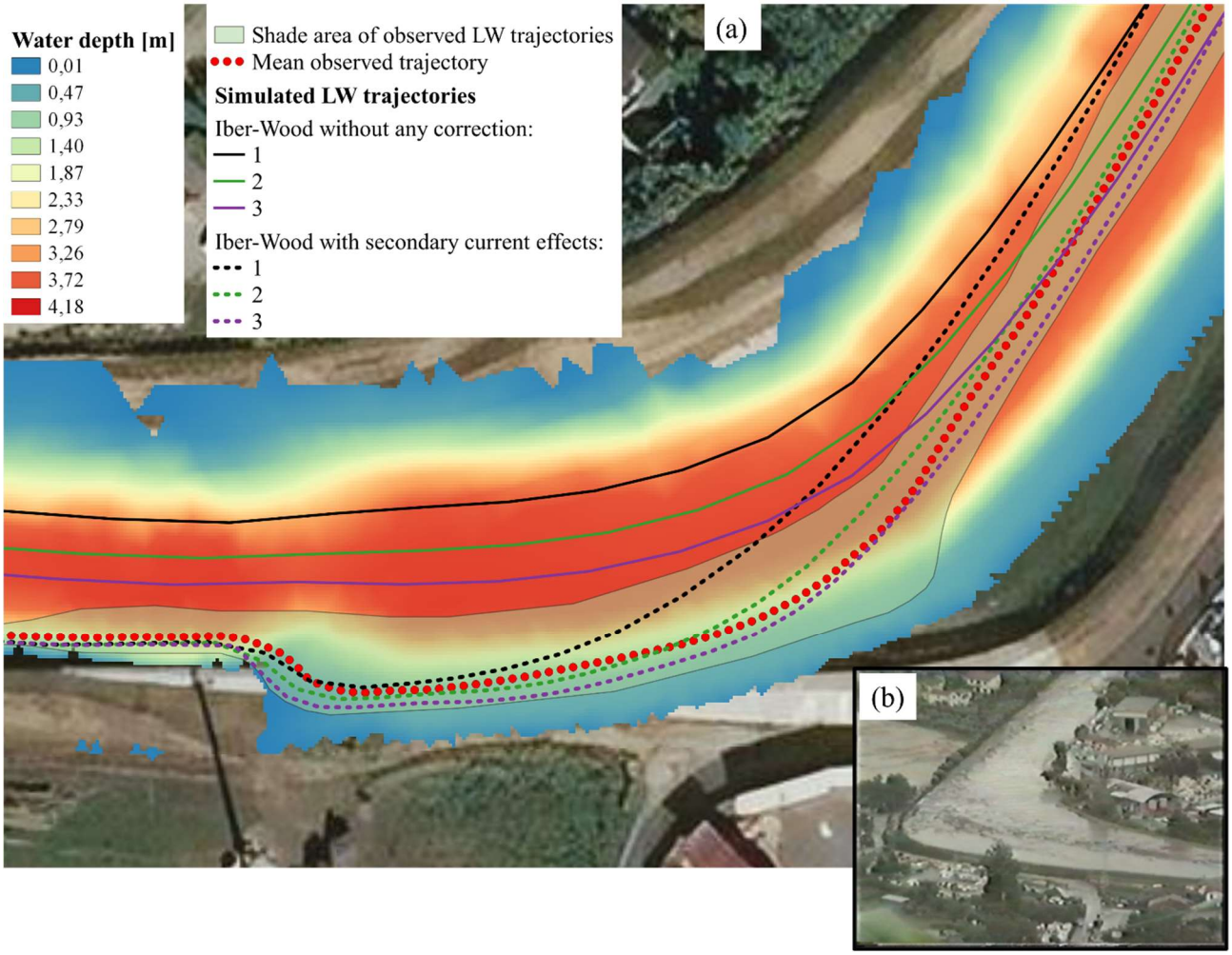

Figure 5.11 Comparison between observed LW pathway and simulated LW trajectories (a), and a picture of the event (b). The observed wood flux is represented by a shade area representative of the area occupied by LW during the flood event, and by the mean observed wood trajectory (dotted red line). Simulated trajectories of three wood pieces (indicated by numbers 1, 2, and 3), selected from the wood flux, are shown considering the model with secondary current effects (dotted lines) and the model without any correction (continuous lines). The background water depth map is referred to the timestep 27000 s, i.e., during the rising limb of the second flood.

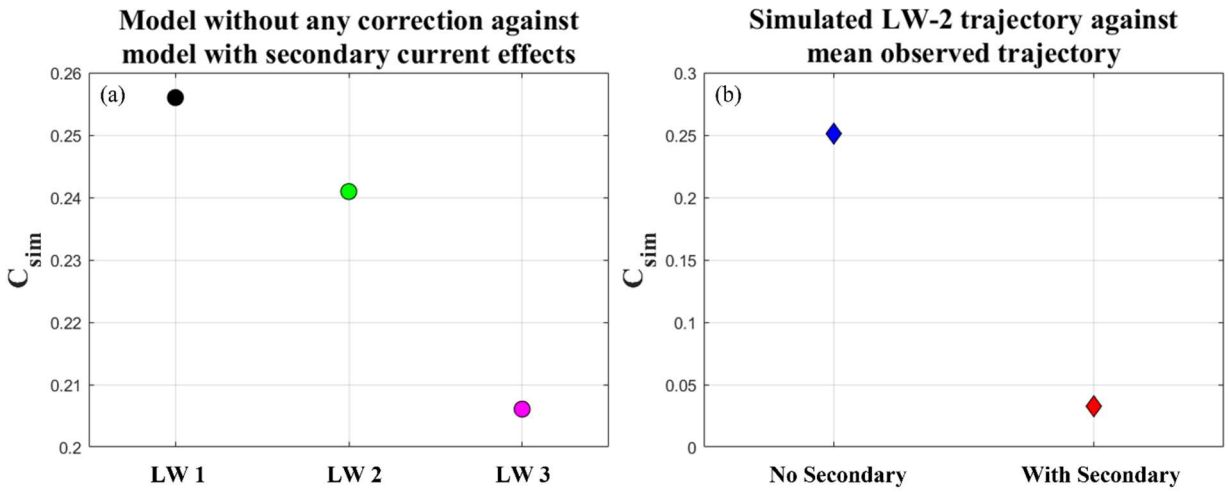

Figure 5.12 Similarity of simulated wood trajectories to results of the model without any correction for considering secondary current effects (a), and to the mean observed trajectory (b). The similarity is expressed through the calculation of C_{sim} (Eq. 4-29).

5.5 Conclusion

The 19 June 1996 flood event at the Versilia River was simulated in order to test the applicability of the new methodologies implemented in Iber-Wood (presented in chapter 4) to reproduce the wood trajectory in a tight river bend. Iber-Wood has been largely used in last years for studying the transport of LW, including river-scale simulations, however the model has never been applied to study wood transport in meandering or curved channels The study case was selected due to the characteristics of the reach that presented a right curve of about 90°, a curvature ratio of 1.7 (the S. Bartolomeo bend) and a huge amount of transported wood.

The hydraulic model was calibrated on the results presented by Paris & Settesoldi (1999) that firstly studied the flood evolution and provided the characterization of the flow hydrograph (see Fig. 5.4). Numerical results agree with the data used for the calibration, while differences were observed in simulating the influence of the breach on the flow due to the different approach considered by Paris & Settesoldi (1999). In fact, the authors assumed that the overflow started first along the river levees before the formation of the breach, and subsequently uniquely from the breach, while the present model highlighted the presence of several points along the investigated reach where the outflow occurred and thus inundating the nearby areas.

Due to the lack of field measurements, the wood boundary condition was set according to available sources, such as images of the flood and the testimony of Prof. Eng. Enio Paris. In order to highlight the simulation of secondary current effects on wood trajectories, large wood simulation was carried out using the enhanced version of Iber-Wood and the model without any correction. Results of these two models differ greatly to each other (see Fig. 5.11), as the observed driftwood was simulated only using the enhanced version of the model. On the contrary, results of the model with the simulation of secondary current effects agree with observations, reproducing the dynamics of wood elements that drifted to the outer bank along the bend, collided with the levee at the end of the bend, and then continued travelling downstream.

In conclusion, the approximations implemented in Iber-Wood for reproducing secondary current effects on the LW transport, provided overall good results in the Versilia River case study, confirming the validity of the proposed approach in simulating LW transport in rivers.

Chapter 6

Conclusions and outlook

6.1 Main conclusions

The results of the present PhD research are here presented as answers to the research questions (Tab. 1.1).

- ***Which are the main variables that are determining the trajectory of LW in a river bend?***

Large wood trajectories in river bends or meanders depend on multiple variables, such as LW characteristics, flow regime, river morphology, and the presence of in-channel structures. The performed flume experiments (see chapter 3) have been designed in order to report novel observations on the trajectories of single floating LW-pieces in a sharp bend. As the dynamics of transported LW in river bends had not yet been studied, the experimental setup was defined with the purpose of investigating the phenomenon, and so, experiments were performed using a constant water discharge, neglecting the interaction between dowels and the bottom of the channel (i.e., dowels were always floating), and no in-channel structures were considered. As a result, the impacts of dowel dimensions, dowel inlet point and initial orientation on the dowel-trajectories are highlighted and the importance of secondary flow is pointed out.

The laboratory activity involved the analysis of twenty-four experimental configurations that come from the combination of four different dowel types, three dowel inlet points and two initial dowel orientations. The size of the dowel strongly influence the LW trajectories, and the dowel length has been pointed out as the main parameter that controls the drift of the dowels towards the outer wall of the channel. In fact, the dowel drift resulted greater for longest dowels. Together with the length, the diameter of the dowel plays an important role in controlling the driftwood, it increases the frontal area of the dowel to the flow, increasing the magnitude of the hydrodynamic forces that act on the dowel. Moreover, the dowel dimensions are observed to be important in controlling the inertia of the bodies that concours to induce the wood drift while moving downstream in the channel bend. The approaching position of the dowel to the bend influence the travel time and the probability that dowels impact on the outer wall. In addition, the approaching position is connected with the travel time as the dowels that approached the bend closer to the inner wall travelled faster than others because of the higher flow velocity of the inner region. The initial dowel orientation is the investigated parameter that has less influence on the dowel trajectories, indeed the dowels tend to travel along the curve with their longitudinal axis parallel to the longitudinal axis of the channel regardless of the starting orientation. Only the smallest dowel (dowel type I) disagree with the latter statement as its observed trajectory depend on the initial orientation.

The conclusion is that the LW dimension is the main variables that is determining the trajectory of a single piece of wood that travels through a sharp river bend.

- ***Which is the drag coefficient for a transported floating LW?***

The drag coefficient is a key parameter for modelling the dynamics of transported LW in rivers and assessing its effect on flow resistance, for this reason its estimation is very much needed. The transport of wood in river

bends is subjected to a three-dimensional flow (the helical flow), however, for floating wood the velocity distribution on the water surface is of particular importance. In river bends, the transversal component of the flow is not negligible as in straight reaches, therefore a two-dimensional approach is needed for studying the wood dynamics. In order to achieve this goal, a 2D mathematical model was presented and applied to flume experiments (see chapter 3).

Calculated drag coefficients are mainly dependent on the dowel size and the relative dowel orientation with respect to the direction of motion. Both these two aspects concur to define the frontal area of the dowels exposed to the flow that determine the hydrodynamic resistance force on the dowel. The application of the model to the present experiments shows that the drag area does not depend on the dowel orientation with respect to the direction of motion as it resulted almost constant in the 90° rotation, it means that the pressure distribution around the dowel does not vary with its orientation. Thus, the drag coefficient decreases with increasing the orientation of the dowel, in disagreement with the available values in the literature which, however, come from different experimental configurations, in which the trunks were held still and were not free to move.

The conclusion is that the drag coefficient of a transported floating LW depends on the orientation of the piece with respect to the direction of motion, and progressively decrease from about 1.2 to about 0.4 for a 90° rotation.

- ***How can a 2D depth-averaged model reproduce the effects of secondary currents on the LW transport?***

The helical flow that characterize sharp river bends has a three-dimensional character that cannot be simulated in a 2D depth-averaged model, however its effects on the mean flow and on the boundary layers can be estimated and implemented. In the present research, the existing model Iber-Wood has been enhanced in order to simulate secondary current effects on the LW transport in river bends (see chapter 4).

The methodologies implemented in the model (section 4.2.1) allow for the consideration of the effects of secondary currents on the depth-averaged flow by adding additional dispersion terms to the horizontal momentum equations. In addition, a transport-type equation is added to the original model for calculating the variation of the secondary flow intensity (I), and, importantly, the direction of the surface velocity vectors is changed accordingly. In this way the effects of secondary flows on the wood trajectory are taken into account.

The Leichtweiß Institute experiments (see chapter 3) are used for testing the proposed methodologies. The simulations of the experimental setup highlight the benefits provided by the implemented methods in reproducing the typical surface flow field that characterize river bends. Moreover, quite good results are obtained by the simulation of the dowel-experiments as secondary current effects increases the similarity to the observed experimental trajectories, particularly, in reproducing the observed drift of the dowels while travelling through the channel bend.

The enhanced version of Iber-Wood is also tested by simulating a river-scale model (see chapter 5). The selected flood event, occurred on 19 June 1996 at the Versilia River, was characterize by a significant wood flux. The focus was on the simulation of LW transport that concurred to the formation of a breach on the outer levee of the S. Bartolomeo curve. The simulated LW trajectories globally agree with the observed ones during the event simulation, reproducing the impact of the wood elements on the outer bank. As observed while simulating Leichtweiß Institute experiments, the model reproduces the wood drift towards the outer bank along the curve quite better than the model without any correction, getting very close to the observed wood flux.

The conclusion is that the effects of secondary currents on the LW transport can be simulated by a 2D depth-averaged model.

6.2 Outlook

In addition to the findings of the present thesis, the following topics would further improve the process of understanding large wood transport in river bends or meanders:

- Investigate how the LW transport regime influence the dynamics of wood in river bends, thereby evaluate the tendency to form stable wood accumulation on the outer bank.
- Examine the role of unsteady flow conditions on the LW transport in river bends.
- Analyze the effect of wood branches and roots on the dynamics of large wood in river bends. The wood shape was already highlighted as a key parameter that influence the dynamics of LW in river corridors, however the influence on transported wood trajectories in bends is unknown.
- Examine the dual interaction between large wood and morphodynamic processes. The morphodynamic evolution of river bends and meanders may change the patterns of wood flux. Physical and numerical modelling as well as field tests are needed to further improve the knowledge about the complex dynamics of large wood-sediments interaction.
- Analyze the influence of in-channel structures on the dynamics of transported LW in river bends and provide estimates for the blockage probability in presence of the helical flow.

References

Abbe, T. B., & Montgomery, D. R. (2003). Patterns and processes of wood debris accumulation in the Queets river basin, Washington. *Geomorphology*, *51*(1–3), 81–107. https://doi.org/10.1016/S0169-555X(02)00326-4

Alonso, C. V. (2004). Transport Mechanics of Stream-Borne Logs. *Riparian Vegetation and Fluvial Geomorphology, Water Science and Application*, *8*, 59–69. https://doi.org/10.1029/008WSA05

Baghlani, A. (2012). Application of a high-resolution scheme in simulation of flow in curved channel using boundary-fitted curvilinear coordinates. *Scientia Iranica*, *19*(6), 1463–1472. https://doi.org/10.1016/j.scient.2012.10.006

Benda, L., Miller, D., Sias, J., Martin, D., Bilby, R., Veldhuisen, C., & Dunne, T. (2003). Wood Recruitment Processes and Wood Budgeting. *American Fisheries Society Symposium*, *37*(January), 49–73.

Benke, A. C., & Wallace, J. B. (2003). Influece of Wood on Invertebrate Communities in Streams and Rivers. In S. Gregory, K. Boyer, & A. Gurnell (Eds.), *The Ecology and Management of Wood in World Rivers* (pp. 149–177).

Bertoldi, W., Gurnell, A. M., & Welber, M. (2013). Wood recruitment and retention: The fate of eroded trees on a braided river explored using a combination of field and remotely-sensed data sources. *Geomorphology*, *180–181*, 146–155. https://doi.org/10.1016/j.geomorph.2012.10.003

Bertoldi, Walter, & Ruiz-Villanueva, V. (2017). Physical and Numerical Modelling of Large Wood and Vegetation in Rivers. *Gravel-Bed Rivers: Process and Disasters*, 729–753. https://doi.org/10.1002/9781118971437.ch27

Bertoldi, Walter, Welber, M., Mao, L., Zanella, S., & Comiti, F. (2014). A flume experiment on wood storage and remobilization in braided river systems. *Earth Surface Processes and Landforms*, *39*(6), 804–813. https://doi.org/10.1002/esp.3537

Bilby, R. E. (2003). Decomposition and Nutrient Dynamics of Wood in Streams and Rivers. In S. Gregory, K. Boyer, & A. Gurnell (Eds.), *The Ecology and Management of Wood in World Rivers* (pp. 135–147).

Bladé, E., Cea, L., Corestein, G., Escolano, E., Puertas, J., Vázquez-Cendón, E., Dolz, J., & Coll, A. (2014). Iber: herramienta de simulación numérica del flujo en ríos. *Revista Internacional de Metodos Numericos Para Calculo y Diseno En Ingenieria*, *30*(1), 1–10. https://doi.org/10.1016/j.rimni.2012.07.004

Blanckaert, K., & de Vriend, H. J. (2004). Secondary flow in sharp open-channel bends. *Journal of Fluid Mechanics*, *498*(498), 353–380. https://doi.org/10.1017/S0022112003006979

Blanckaert, Koen, & De Vriend, H. J. (2003). Nonlinear modeling of mean flow redistribution in curved

open channels. *Water Resources Research*, *39*(12), 1–14. https://doi.org/10.1029/2003WR002068

Blanckaert, Koen, Kleinhans, M. G., Mclelland, S. J., Uijttewaal, W. S. J., Murphy, B. J., van de Kruijs, A., Parsons, D. R., & Chen, Q. (2013). Flow separation at the inner (convex) and outer (concave) banks of constant-width and widening open-channel bends. *Earth Surface Processes and Landforms*, *38*(7), 696–716. https://doi.org/10.1002/esp.3324

Bocchiola, D. (2011). Hydraulic characteristics and habitat suitability in presence of woody debris: A flume experiment. *Advances in Water Resources*, *34*(10), 1304–1319. https://doi.org/10.1016/j.advwatres.2011.06.011

Bocchiola, D., Rulli, M. C., & Rosso, R. (2006). Flume experiments on wood entrainment in rivers. *Advances in Water Resources*, *29*, 1182–1195. https://doi.org/10.1016/j.advwatres.2005.09.006

Bocchiola, D., Rulli, M. C., & Rosso, R. (2008). A flume experiment on the formation of wood jams in rivers. *Water Resources Research*, *44*(2), 1–17. https://doi.org/10.1029/2006WR005846

Bradley, J. B., Richards, D. L., & Bahner, C. D. (2005). *Debris control structures: Evaluation and countermeasures. ReportNo. FHWA-IF-04-016* (3rd ed.). Federal Highway Administration, Washington, DC. http://www.fedworld.gov/ntis/

Braudrick, A., & Grant, E. (2000). When do logs move in Rivers? *Water Resources Research*, *36*(2), 571–583. https://doi.org/10.1029/1999WR900290

Braudrick, C. A., Grant, G. E., Ishikawa, Y., & Ikeda, H. (1997). Dynamics of Wood Transport in Streams: A Flume Experiment. *Earth Surface Processes and Landforms*, *22*(7), 669–683. https://doi.org/10.1002/(sici)1096-9837(199707)22:7<669::aid-esp740>3.3.co;2-c

Brown, D., & Christian, W. (2011). SIMULATION WHAT YOU SEE: COMBINING COMPUTER MODELING WITH VIDEO ANALYSIS. *MPTL 16 and HSCI 2011*, *September*. https://doi.org/10.1111/j.1467-7652.2011.00632.x

Comiti, F., Andreoli, A., Lenzi, M. A., & Mao, L. (2006). Spatial density and characteristics of woody debris in five mountain rivers of the Dolomites (Italian Alps). *Geomorphology*, *78*(1–2), 44–63. https://doi.org/10.1016/j.geomorph.2006.01.021

Comiti, Francesco. (2012). How natural are Alpine mountain rivers? Evidence from the Italian Alps. *Earth Surface Processes and Landforms*, *37*(7), 693–707. https://doi.org/10.1002/esp.2267

Curran, J. C. (2010). Mobility of large woody debris (LWD) jams in a low gradient channel. *Geomorphology*, *116*(3–4), 320–329. https://doi.org/10.1016/j.geomorph.2009.11.027

D'Aoust, S. G., & Millar, R. G. (2000). Stability of Ballasted Woody Debris Habitat Structures. *Journal of Hydraulic Engineering*, *126*(11), 810–817.

Davidson, S. L., MacKenzie, L. G., & Eaton, B. C. (2015). Large wood transport and jam formation in a series of flume experiments. *Water Resources Association*, *51*, 10065–10077. https://doi.org/10.1002/2015WR017446

De Cicco, Pina N., Paris, E., Solari, L., & Ruiz-Villanueva, V. (2020). Bridge pier shape influence on wood accumulation: Outcomes from flume experiments and numerical modelling. *Journal of Flood Risk Management*, *June 2018*, 1–16. https://doi.org/10.1111/jfr3.12599

De Cicco, Pina Nicoletta, Paris, E., Ruiz-Villanueva, V., Solari, L., & Stoffel, M. (2018). In-channel wood-related hazards at bridges: A review. *River Research and Applications*, *34*(7), 617–628. https://doi.org/10.1002/rra.3300

Deltares. (2019). *3D/2D modelling suite for integral water solutions: Hydro-Morphodynamics*. https://content.oss.deltares.nl/delft3d/manuals/Delft3D-FLOW_User_Manual.pdf

Diehl, T. H. (1997). Potential Drift Accumulation at Bridges. *US Department of Transportation, Federal Highway Administration, Research and Development, Turner-Fairbank Highway Research Center*, *April*, 45.

European Commission 2000/60/EC. (2000). Directive 2000/60/EC of the European Parliament and of the Council. *Official Journal of the European Communities*. https://ec.europa.eu/environment/water/water-framework/index_en.html

Ghamry, H. K., & Steffler, P. M. (2005). Two-dimensional depth-averaged modeling of flow in curved open channels. *Journal of Hydraulic Engineering*, *119*(1), 44–55. https://doi.org/10.1080/00221680509500110

Gippel, C. J., Finlayson, B. L., & O'Neill, I. C. (1996). Distribution and hydraulic significance of large woody debris in a lowland Australian river. *Hydrobiologia*, *318*(3), 179–194. https://doi.org/10.1007/BF00016679

Gippel, Christopher J., O'Neill, I. C., Finlayson, B. L., & Schnatz, I. (1996). Hydraulic guidelines for the re-introduction and management of large woody debris in lowland rivers. *Regulated Rivers: Research and Management*, *12*(2–3), 223–236. https://doi.org/10.1002/(SICI)1099-1646(199603)12:2/33.0.CO;2-

Gregory, V., Meleason, M. A., & Sobota, D. J. (2003). Modeling the Dynamics of Wood in Streams and Rivers History of Wood Models. In *The Ecology and Management of Wood in World Rivers* (pp. 315–335).

Gurnell, A. M. (2003). Wood storage and mobility. In S. Gregory, K. Boyer, & A. Gurnell (Eds.), *The Ecology and Management of Wood in World Rivers* (pp. 75–91). American Fisheries Society.

Gurnell, A. M. (2013). Wood in Fluvial Systems. In J. F. Shroder (Ed.), *Treatise on geomorphology* (pp. 163–188). https://doi.org/10.1016/B978-0-12-374739-6.00236-0

Gurnell, A. M., Piégay, H., Swanson, F. J., & Gregory, S. V. (2002). Large wood and fluvial processes. *Freshwater Biology*, *47*(4), 601–619. https://doi.org/10.1046/j.1365-2427.2002.00916.x

Haga, H., Kumagai, T., Otsuki, K., & Ogawa, S. (2002). Transport and retention of coarse woody debris in mountain streams: An in situ field experiment of log transport and a field survey of coarse woody debris distribution. In *Water Resources Research* (Vol. 38, Issue 8, pp. 1-1-1–16). https://doi.org/10.1029/2001WR001123

Hickin, E. J. (1984). Vegetation and River Channel Dynamics. *Canadian Geographer / Le Géographe Canadien*, *28*(2), 111–126. https://doi.org/10.1111/j.1541-0064.1984.tb00779.x

Hygelund, B., & Manga, M. (2003). *Hygelund and Manga 2003 drag coeff of wood*. *51*, 1–11. papers2://publication/doi/10.1016/S0169-555X(02)00335-5

Iroumé, A., Ruiz-Villanueva, V., Mao, L., Barrientos, G., Stoffel, M., & Vergara, G. (2018). Geomorphic and stream flow influences on large wood dynamics and displacement lengths in high gradient mountain streams (Chile). *Hydrological Processes*, *32*(17), 2636–2653. https://doi.org/10.1002/hyp.13157

Jagers, H. R. A. (2003). *Modelling planform changes of braided rivers*.

Kalkwijk, J. P. T., & Booij, R. (1986). Adaptation of secondary flow in nearly-horizontal flow. *Journal of Hydraulic Research*, *24*(1), 19–37. https://doi.org/10.1080/00221688609499330

Kang, T., & Kimura, I. (2018). Computational modeling for large wood dynamics with root wad and anisotropic bed friction in shallow flows. *Advances in Water Resources*, *121*(September), 419–431. https://doi.org/10.1016/j.advwatres.2018.09.006

Kramer, N., & Wohl, E. (2014). Estimating fluvial wood discharge using time-lapse photography with varying sampling intervals. *Earth Surface Processes and Landforms*, *39*(6), 844–852. https://doi.org/10.1002/esp.3540

Kramer, N., & Wohl, E. (2017). Rules of the road: A qualitative and quantitative synthesis of large wood transport through drainage networks. *Geomorphology*, *279*, 74–97. https://doi.org/10.1016/j.geomorph.2016.08.026

Kruskal, W. H., & Wallis, W. A. (1952). Use of Ranks in One-Criterion Variance Analysis. *Journal of American Statistical Association*, *47*(260), 583–621.

Lane, S. N., Bradbrook, K. F., Richards, K. S., Biron, P. A., & Roy, A. G. (1999). The application of computational fluid dynamics to natural river channels: Three-dimensional versus two-dimensional approaches. *Geomorphology*, *29*(1–2), 1–20. https://doi.org/10.1016/S0169-555X(99)00003-3

Lienkaemper, G. W., & Swanson, F. J. (1987). Dynamics of large woody debris in streams in old-growth

Douglas-fir forests. *Canadian Journal of Forest Research*, *17*(2), 150–156. https://doi.org/10.1139/x87-027

MacVicar, B. J., Piégay, H., Henderson, A., Comiti, F., Oberlin, C., & Pecorari, E. (2009). Quantifying the temporal dynamics of wood in large rivers: field trials of wood surveying, dating, tracking, and monitoring techniques. *Earth Surface Processes and Landforms*, *34*(November), 2031–2046. https://doi.org/10.1002/esp

MacVicar, B., & Piégay, H. (2012). Implementation and validation of video monitoring for wood budgeting in a wandering piedmont river, the Ain River (France). *Earth Surface Processes and Landforms*, *37*(12), 1272–1289. https://doi.org/10.1002/esp.3240

Manning, R. (1891). On the Flow of water in open channel and pipes. *Transactions of the Institution of Civil Engineers of Ireland*, *20*, 161–207.

Mazzorana, B., Hübl, J., Zischg, A., & Largiader, A. (2011). Modelling woody material transport and deposition in alpine rivers. *Natural Hazards*, *56*(2), 425–449. https://doi.org/10.1007/s11069-009-9492-y

Mazzorana, B., Ruiz-Villanueva, V., Marchi, L., Cavalli, M., Gems, B., Gschnitzer, T., Mao, L., Iroumé, A., & Valdebenito, G. (2018). Assessing and mitigating large wood-related hazards in mountain streams: recent approaches. *Journal of Flood Risk Management*, *11*(2), 207–222. https://doi.org/10.1111/jfr3.12316

Meninno, S., Persi, E., Petaccia, G., Sibilla, S., & Armanini, A. (2020). An experimental and theoretical analysis of floating wood diffusion coefficients. *Environmental Fluid Mechanics*, *20*(3), 593–617. https://doi.org/10.1007/s10652-019-09693-x

Millington, C. E., & Sear, D. A. (2007). Impacts of river restoration on small-wood dynamics in a low-gradient headwater stream. *Earth Surface Processes and Landforms*, *32*(July), 1204–1218. https://doi.org/10.1002/esp1552

Nabi, M., Ottevanger, W., & Giri, S. (2016). Computational modelling of secondary flow on unstructured grids. *River Sedimentation - Proceedings of the 13th International Symposium on River Sedimentation, ISRS 2016*, 719–726.

Nakamura, F., & Swanson, F. J. (1994). Distribution of coarse woody debris in a mountain stream, western Cascase Range, Oregon. *Canadian Journal of Forest Research*, *24*(12), 2395–2403. https://doi.org/10.1139/x94-309

Nanson, G. C., & Croke, J. C. (1992). A genetic classification of floodplains. *Geomorphology*, *4*(6), 459–486. https://doi.org/10.1016/0169-555X(92)90039-Q

Nanson, G. C., & Hickin, E. J. (1986). A statistical analysis of bank erosion and channel migration in

western Canada. *Geological Society of America Bulletin*, *97*(4), 497–504. https://doi.org/10.1130/0016-7606(1986)97<497:ASAOBE>2.0.CO;2

Nash, J., & Sutcliffe, J. (1970). River flow forecasting through conceptual models part I — A discussion of principles. *Journal of Hydrology*, *10*(3), 282–290. https://doi.org/10.1016/0022-1694(70)90255-6

Odgaard, A. J. (1986). Meander flow model. I: Development. *Journal of Hydraulic Engineering*, *12*(12), 1117–1135.

Paris, E., & Settesoldi, D. (1999). SULLA ROTTA DEL F. VERSILIA DEL 19 giugno 1996. *Giornate Di Studio Su "Difesa Idraulica Del Territorio", Trieste, 23-24 Settembre 1999*.

Persi, E., Petaccia, G., & Sibilla, S. (2018). Large wood transport modelling by a coupled Eulerian–Lagrangian approach. *Natural Hazards*, *91*(s1), 59–74. https://doi.org/10.1007/s11069-017-2891-6

Persi, E., Petaccia, G., Sibilla, S., Brufau, P., & García-Navarro, P. (2019). Calibration of a dynamic Eulerian-lagrangian model for the computation of wood cylinders transport in shallow water flow. *Journal of Hydroinformatics*, *21*, 164–179. https://doi.org/10.2166/hydro.2018.085

Rastogi, A. K., & Rodi, W. (1978). Prediction of heat and mass transfer in open channels. *Journal of Hydraulics Division*, *104*(3), 397–420.

Rinaldi, M., Mengoni, B., Luppi, L., Darby, S. E., & Mosselman, E. (2008). Numerical simulation of hydrodynamics and bank erosion in a river bend. *Water Resources Research*, *44*(9), 1–17. https://doi.org/10.1029/2008WR007008

Rozovskii, I. L. (1957). *Flow of water in bends of open channels*. Academy of Sciences of the Ukrainian SSR, Kiev, 1957; Israel Program for Scientific Translations, Jerusalem, 1961.

Ruiz-Villanueva, V., Gamberini, C., Bladé, E., Stoffel, M., & Bertoldi, W. (2020). Numerical Modeling of Instream Wood Transport, Deposition, and Accumulation in Braided Morphologies Under Unsteady Conditions: Sensitivity and High-Resolution Quantitative Model Validation. *Water Resources Research*, *56*(7), 1–22. https://doi.org/10.1029/2019WR026221

Ruiz-Villanueva, Virginia, Bladé, E., Sánchez-Juny, M., Marti-Cardona, B., Díez-Herrero, A., & Bodoque, J. M. (2014). Two-dimensional numerical modeling of wood transport. *Journal of Hydroinformatics*, *16*(5), 1077–1096. https://doi.org/10.2166/hydro.2014.026

Ruiz-Villanueva, Virginia, Wyżga, B., Mikuś, P., Hajdukiewicz, M., & Stoffel, M. (2017). Large wood clogging during floods in a gravel-bed river: the Długopole bridge in the Czarny Dunajec River, Poland. *Earth Surface Processes and Landforms*, *42*(3), 516–530. https://doi.org/10.1002/esp.4091

Ruiz-Villanueva, Virginia, Wyżga, B., Zawiejska, J., Hajdukiewicz, M., & Stoffel, M. (2016). Factors controlling large-wood transport in a mountain river. *Geomorphology*, *272*, 21–31.

https://doi.org/10.1016/j.geomorph.2015.04.004

Ruiz Villanueva, V., Bladé Castellet, E., Díez-Herrero, A., Bodoque, J. M., & Sánchez-Juny, M. (2014). Two-dimensional modelling of large wood transport during flash floods. *Earth Surface Processes and Landforms*, *39*(4), 438–449. https://doi.org/10.1002/esp.3456

Saffman, P. G. (1965). The lift on a small sphere in a slow shear flow. *Journal of Fluid Mechanics*, *22*(2), 385–400. https://doi.org/10.1017/S0022112065000824

Schalko, I., Schmocker, L., Weitbrecht, V., & Boes, R. M. (2018). Backwater Rise due to Large Wood Accumulations. *Journal of Hydraulic Engineering*, *144*(9), 04018056. https://doi.org/10.1061/(asce)hy.1943-7900.0001501

Schenk, E. R., Moulin, B., Hupp, C. R., & Richter, J. M. (2014). Large wood budget and transport dynamics on a large river using radio telemetry. *Earth Surface Processes and Landforms*, *39*(4), 487–498. https://doi.org/10.1002/esp.3463

Schmocker, L., & Hager, W. H. (2011). Probability of Drift Blockage at Bridge Decks. *Journal of Hydraulic Engineering*, *137*(4), 470–479. https://doi.org/10.1061/(asce)hy.1943-7900.0000319

Schmocker, L., & Hager, W. H. (2013). Scale Modeling of Wooden Debris Accumulation at a Debris Rack. *Journal of Hydraulic Engineering*, *139*(8), 827–836. https://doi.org/10.1061/(asce)hy.1943-7900.0000714

Schmocker, L., & Weitbrecht, V. (2013). Driftwood: Risk Analysis and Engineering Measures. *Journal of Hydraulic Engineering*, *139*(7), 683–695. https://doi.org/10.1061/(asce)hy.1943-7900.0000728

Shields, F. D., & Alonso, C. V. (2012). Assessment of flow forces on large wood in rivers. *Water Resources Research*, *48*(4), 1–16. https://doi.org/10.1029/2011WR011547

Song, C. G., Seo, I. W., & Kim, Y. Do. (2012). Analysis of secondary current effect in the modeling of shallow flow in open channels. *Advances in Water Resources*, *41*, 29–48. https://doi.org/10.1016/j.advwatres.2012.02.003

Swanson, F. J., Gregory, S. V, Iroumé, A., Ruiz-villanueva, V., & Wohl, E. (2020). *Reflections on the history of research on large wood in rivers*. https://doi.org/10.1002/esp.4814

Vasquez, J. A., Millar, R. G., & Steffler, P. M. (2005). Vertically-averaged and moment of momentum model for alluvial bend morphology. *River,Coastal and Estuarine Morphodynamics:RCEM 2005*, 711–718.

Wallerstein, N., & Thorne, C. R. (1997). *Impacts of woody debris on fluvial processes and channel morphology in stable and unstable streams*.

Welber, M., Bertoldi, W., & Tubino, M. (2013). Wood dispersal in braided streams: Results from physical

modeling. *Water Resources Research*, *49*(11), 7388–7400. https://doi.org/10.1002/2013WR014046

Wohl, E. (2011). Threshold-induced complex behavior of wood in mountain streams. *Geology*, *39*(6), 587–590. https://doi.org/10.1130/G32105.1

Wohl, E., Bledsoe, B. P., Fausch, K. D., Kramer, N., Bestgen, K. R., & Gooseff, M. N. (2016). Management of Large Wood in Streams: An Overview and Proposed Framework for Hazard Evaluation. *Journal of the American Water Resources Association*, *52*(2), 315–335. https://doi.org/10.1111/1752-1688.12388

Wohl, E., & Goode, J. R. (2008). Wood dynamics in headwater streams of the Colorado Rocky Mountains. *Water Resources Research*, *44*(9), 1–14. https://doi.org/10.1029/2007WR006522

Wohl, E., Kramer, N., Ruiz-Villanueva, V., Scott, D. N., Comiti, F., Gurnell, A. M., Piegay, H., Lininger, K. B., Jaeger, K. L., Walters, D. M., & Fausch, K. D. (2019). The natural wood regime in rivers. *BioScience*, *69*(4), 259–273. https://doi.org/10.1093/biosci/biz013

Wyzga, B., & Zawiejska, J. (2005). Wood storage in a wide mountain river: Case study of the Czarny Dunajec, Polish Carpathians. *Earth Surface Processes and Landforms*, *30*(12), 1475–1494. https://doi.org/10.1002/esp.1204

Zaid, B. A. (2017). *Development of Design Guidelines for Shallow Groynes* (Issue April). https://doi.org/https://doi.org/10.24355/dbbs.084-201804100941

Zischg, A. P., Galatioto, N., Deplazes, S., Weingartner, R., & Mazzorana, B. (2018). Modelling spatiotemporal dynamics of large wood recruitment, transport, and deposition at the river reach scale during extreme floods. *Water*, *10*(9). https://doi.org/10.3390/w10091134

Appendices

A. Experimental flow patterns

The complete flow field measurements collected by Zaid (2017) are reported in Figs. A.1 and A.2. Figure A.1 visualizes the velocity magnitude in planes parallel to the bed, while Fig. A.2 shows the flow field within the cross-sections defined along the curve, CS1 – CS9 (see Fig. 3.2). From z = 7 cm to z = 9 cm, the velocities were similar along the verticals, with a difference of 2÷4%. For this reason, and to avoid possible errors arising from the measurements with the side-looking probe close to the surface, the velocities at the surface were approximated with the velocities at z = 7 cm and the corresponding results for these layers are not shown.

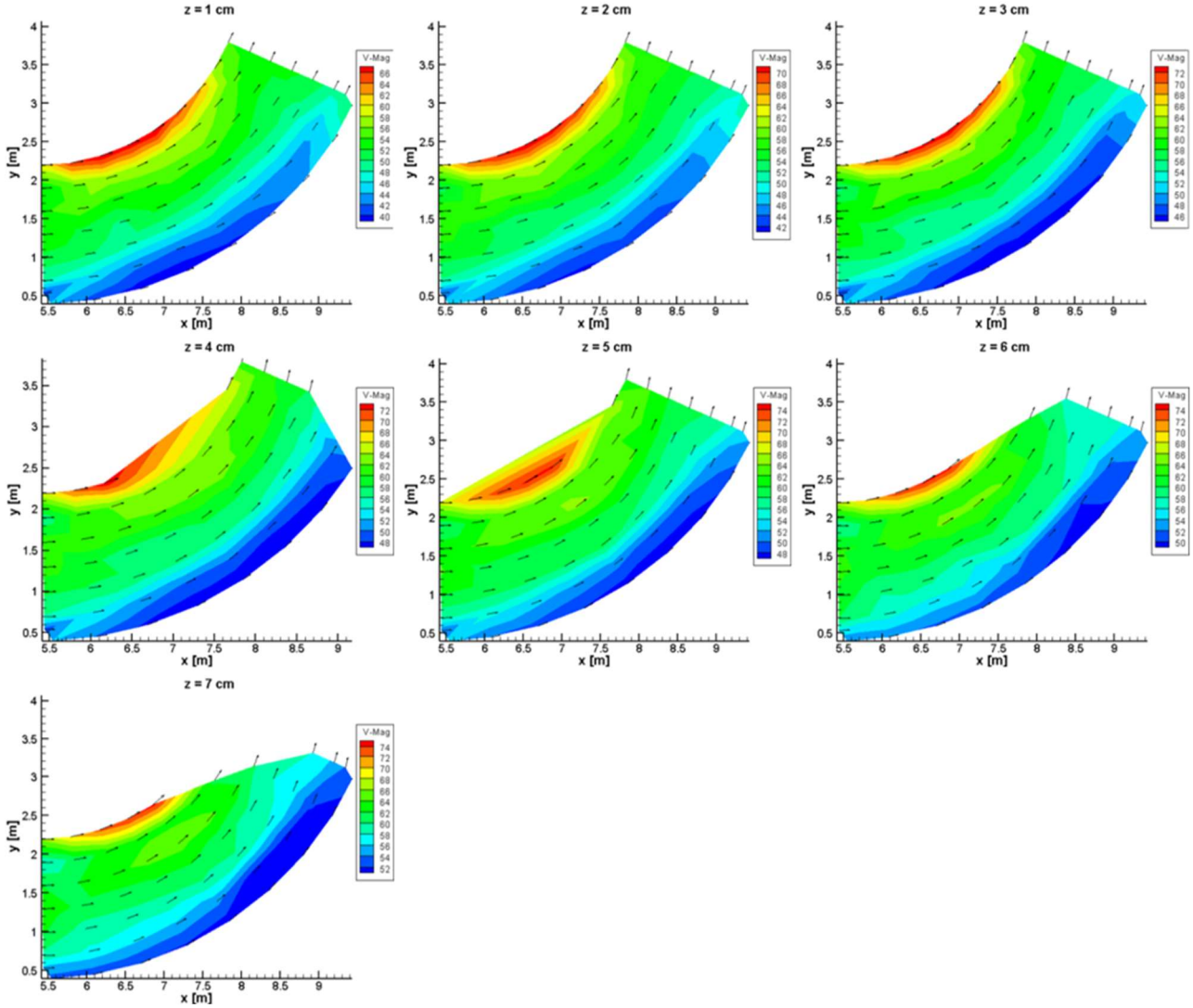

Figure A.1 2D flow field. The velocity magnitude (V-mag) is reported for different levels of water depth, z indicates the height of the plan above the bottom of the channel (redrawn from Zaid, 2017). V-mag is expressed in cm s^{-1}.

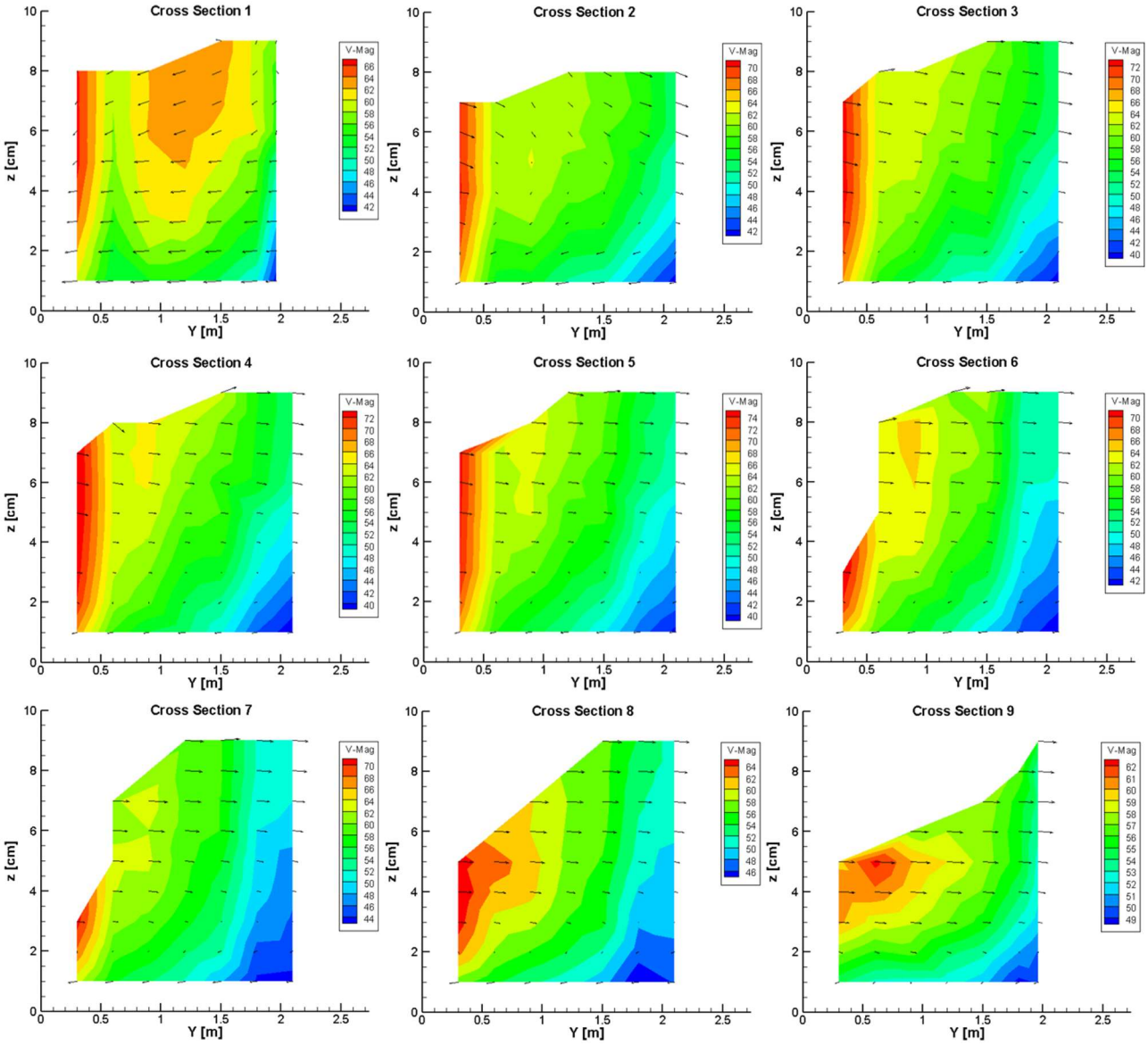

Figure A.2 The 2D flow field at cross-sections CS1 – CS9, V-Mag is the velocity magnitude expressed in cm s^{-1} (redrawn from Zaid, 2017).

B. Experimental dowel trajectories

The results of the twenty-four experimental configurations are reported below.

- Table B.1 reports for each experimental configuration the values of (i) the mean travel time (T), (ii) the mean distance from the left wall of the channel at CS1 – CS9 (d), and the coefficient of variation at CS1 – CS9 (C_v); for each configuration twenty runs were considered.
- Figures B.1 – B.4 report dowel trajectories and boxplots for the twenty-four experimental configurations. B.1 shows results of dowel type I, B.2 of dowel type II, B.3 of dowel type III, and B.4 of dowel type IV.
- Figure B.5 reports the comparison between the two considered dowel initial orientation (i.e., parallel and perpendicular) for each dowel type.
- Figures B.6 – B.9 report the comparison between flow streamlines and experimental dowel trajectories. B.6 shows results of dowel type I, B.7 of dowel type II, B.8 of dowel type III, and B.9 of dowel type IV.

Table B.1 Summary of the twenty-four experimental configurations. The table reports values of the mean travel time (T), the mean distance from the left wall (d), and the coefficient of variation (C_v).

	Cross section								
	CS1	CS2	CS3	CS4	CS5	CS6	CS7	CS8	CS9
Dowel I - I_1 – parallel [T=11.8s]									
d [m]	0.213	0.213	0.225	0.225	0.245	0.270	0.303	0.346	0.408
C_v [-]	0.166	0.180	0.179	0.169	0.164	0.150	0.136	0.137	0.137
Dowel I - I_1 – perpendicular [T=12.2s]									
d [m]	0.370	0.375	0.398	0.429	0.462	0.498	0.541	0.595	0.680
C_v [-]	0.088	0.098	0.103	0.109	0.113	0.121	0.122	0.122	0.124
Dowel I - I_2 – parallel [T=15.1s]									
d [m]	1.097	1.087	1.099	1.130	1.161	1.211	1.278	1.366	1.475
C_v [-]	0.052	0.064	0.076	0.082	0.085	0.090	0.094	0.095	0.094
Dowel I - I_2 – perpendicular [T=14.6s]									
d [m]	1.041	1.030	1.039	1.062	1.091	1.130	1.177	1.239	1.329
C_v [-]	0.035	0.043	0.050	0.056	0.062	0.066	0.069	0.072	0.072
Dowel I - I_3 – parallel [T=20.3s]									
d [m]	2.009	2.021	2.044	2.070	2.094	2.117	2.140	2.163	2.186

C_v [-]	0.047	0.056	0.062	0.063	0.061	0.057	0.050	0.044	0.035
Dowel I - I_3 – perpendicular [T=21.0s]									
d [m]	2.025	2.056	2.094	2.137	2.174	2.204	2.221	2.229	2.240
C_v [-]	0.029	0.033	0.037	0.038	0.036	0.032	0.028	0.024	0.023
Dowel II - I_1 – parallel [T=12.5s]									
d [m]	0.289	0.295	0.309	0.323	0.344	0.373	0.413	0.474	0.557
C_v [-]	0.231	0.233	0.233	0.228	0.225	0.215	0.213	0.202	0.185
Dowel II - I_1 – perpendicular [T=12.5s]									
d [m]	0.277	0.284	0.301	0.321	0.349	0.381	0.424	0.487	0.577
C_v [-]	0.172	0.185	0.184	0.188	0.186	0.187	0.183	0.170	0.159
Dowel II - I_2 – parallel [T=15.8s]									
d [m]	1.069	1.055	1.064	1.088	1.121	1.157	1.213	1.290	1.396
C_v [-]	0.055	0.060	0.062	0.064	0.065	0.067	0.071	0.071	0.069
Dowel II - I_2 – perpendicular [T=15.4s]									
d [m]	1.085	1.073	1.081	1.102	1.128	1.166	1.221	1.294	1.397
C_v [-]	0.052	0.058	0.067	0.075	0.081	0.088	0.092	0.095	0.096
Dowel II - I_3 – parallel [T=20.8s]									
d [m]	1.958	1.974	2.002	2.025	2.044	2.062	2.069	2.075	2.104
C_v [-]	0.034	0.046	0.057	0.063	0.065	0.063	0.059	0.049	0.043
Dowel II - I_3 – perpendicular [T=19.9s]									
d [m]	1.902	1.906	1.936	1.982	2.032	2.079	2.116	2.147	2.167
C_v [-]	0.026	0.037	0.045	0.050	0.050	0.044	0.032	0.025	0.030
Dowel III - I_1 – parallel [T=12.3s]									
d [m]	0.269	0.277	0.292	0.311	0.336	0.367	0.405	0.458	0.537
C_v [-]	0.191	0.196	0.193	0.191	0.194	0.194	0.197	0.196	0.189
Dowel III - I_1 – perpendicular [T=12.4s]									
d [m]	0.242	0.250	0.266	0.285	0.310	0.342	0.383	0.443	0.528
C_v [-]	0.196	0.198	0.201	0.200	0.197	0.185	0.179	0.169	0.155
Dowel III - I_2 – parallel [T=15.3s]									
d [m]	1.078	1.071	1.087	1.119	1.157	1.203	1.260	1.333	1.432
C_v [-]	0.044	0.053	0.058	0.064	0.068	0.070	0.072	0.073	0.072

Dowel III - I_2 – perpendicular [T=15.1s]									
d [m]	1.072	1.060	1.067	1.092	1.122	1.160	1.212	1.281	1.380
C_v [-]	0.031	0.039	0.044	0.050	0.058	0.063	0.067	0.067	0.067
Dowel III - I_3 – parallel [T=20.6s]									
d [m]	2.069	2.067	2.083	2.100	2.113	2.124	2.139	2.155	2.187
C_v [-]	0.058	0.072	0.081	0.084	0.080	0.071	0.060	0.048	0.039
Dowel III - I_3 – perpendicular [T=19.5s]									
d [m]	2.022	2.029	2.054	2.094	2.125	2.148	2.171	2.183	2.192
C_v [-]	0.040	0.042	0.043	0.044	0.044	0.044	0.043	0.041	0.041
Dowel IV - I_1 – parallel [T=13.7s]									
d [m]	0.322	0.323	0.335	0.351	0.374	0.404	0.441	0.495	0.571
C_v [-]	0.091	0.103	0.113	0.122	0.137	0.147	0.155	0.162	0.168
Dowel IV - I_1 – perpendicular [T=13.1s]									
d [m]	0.283	0.298	0.321	0.349	0.384	0.428	0.483	0.557	0.657
C_v [-]	0.099	0.106	0.113	0.121	0.126	0.133	0.136	0.139	0.136
Dowel IV – I_2 – parallel [T=16.1s]									
d [m]	1.093	1.094	1.110	1.140	1.180	1.227	1.289	1.367	1.474
C_v [-]	0.033	0.036	0.039	0.046	0.049	0.053	0.057	0.060	0.064
Dowel IV - I_2 – perpendicular [T=16.8s]									
d [m]	1.109	1.103	1.119	1.148	1.187	1.236	1.301	1.384	1.493
C_v [-]	0.045	0.054	0.062	0.068	0.074	0.079	0.085	0.089	0.091
Dowel IV - I_3 – parallel [T=20.1s]									
d [m]	1.889	1.889	1.898	1.910	1.925	1.938	1.957	1.988	2.040
C_v [-]	0.055	0.072	0.088	0.099	0.107	0.107	0.101	0.089	0.075
Dowel IV - I_3 – perpendicular [T=19.7s]									
d [m]	1.952	1.918	1.914	1.934	1.971	2.020	2.076	2.136	2.184
C_v [-]	0.020	0.024	0.027	0.029	0.034	0.038	0.035	0.033	0.033

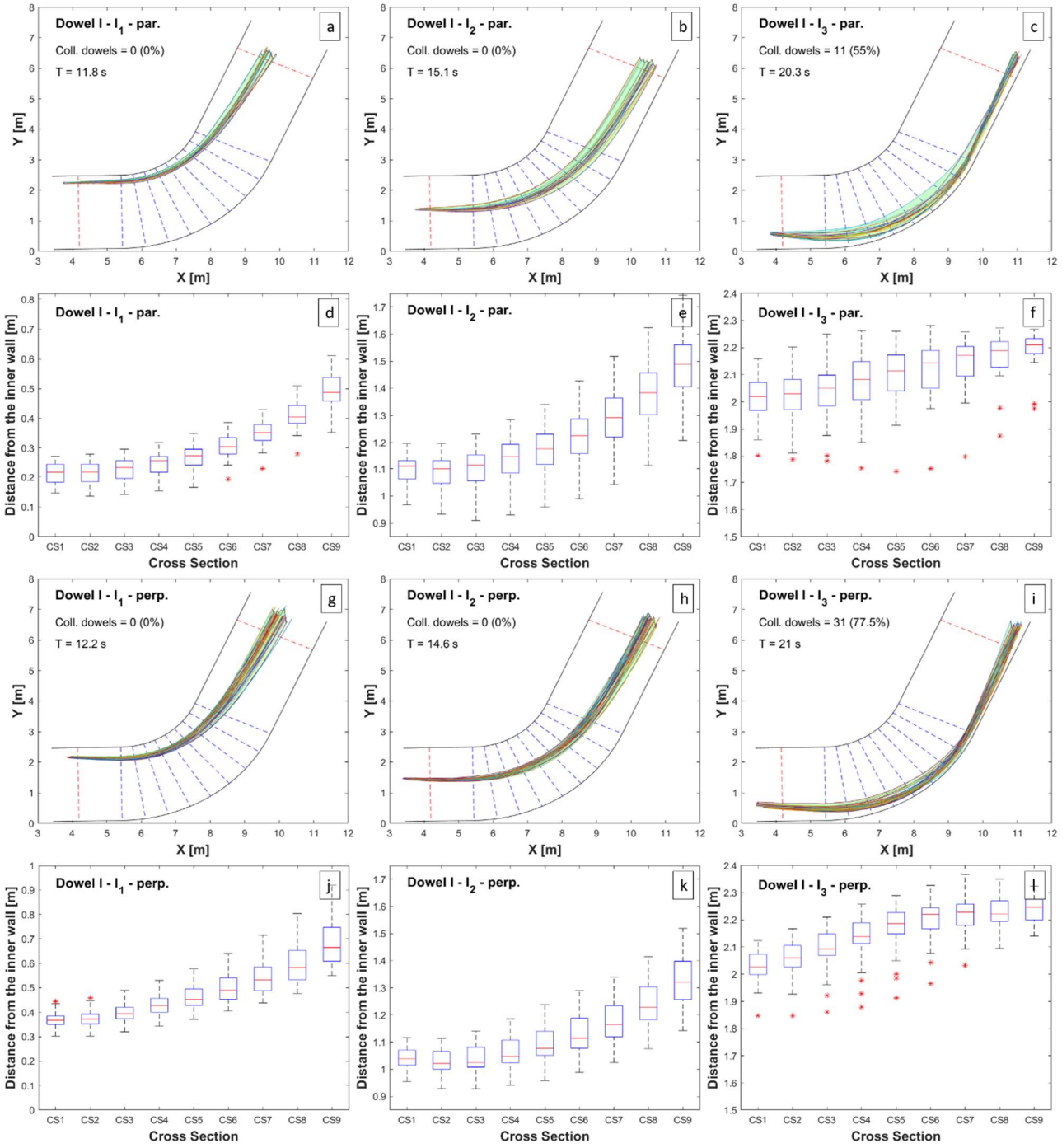

Figure B.1 Trajectories and boxplots of the six experimental configurations for dowel type I.

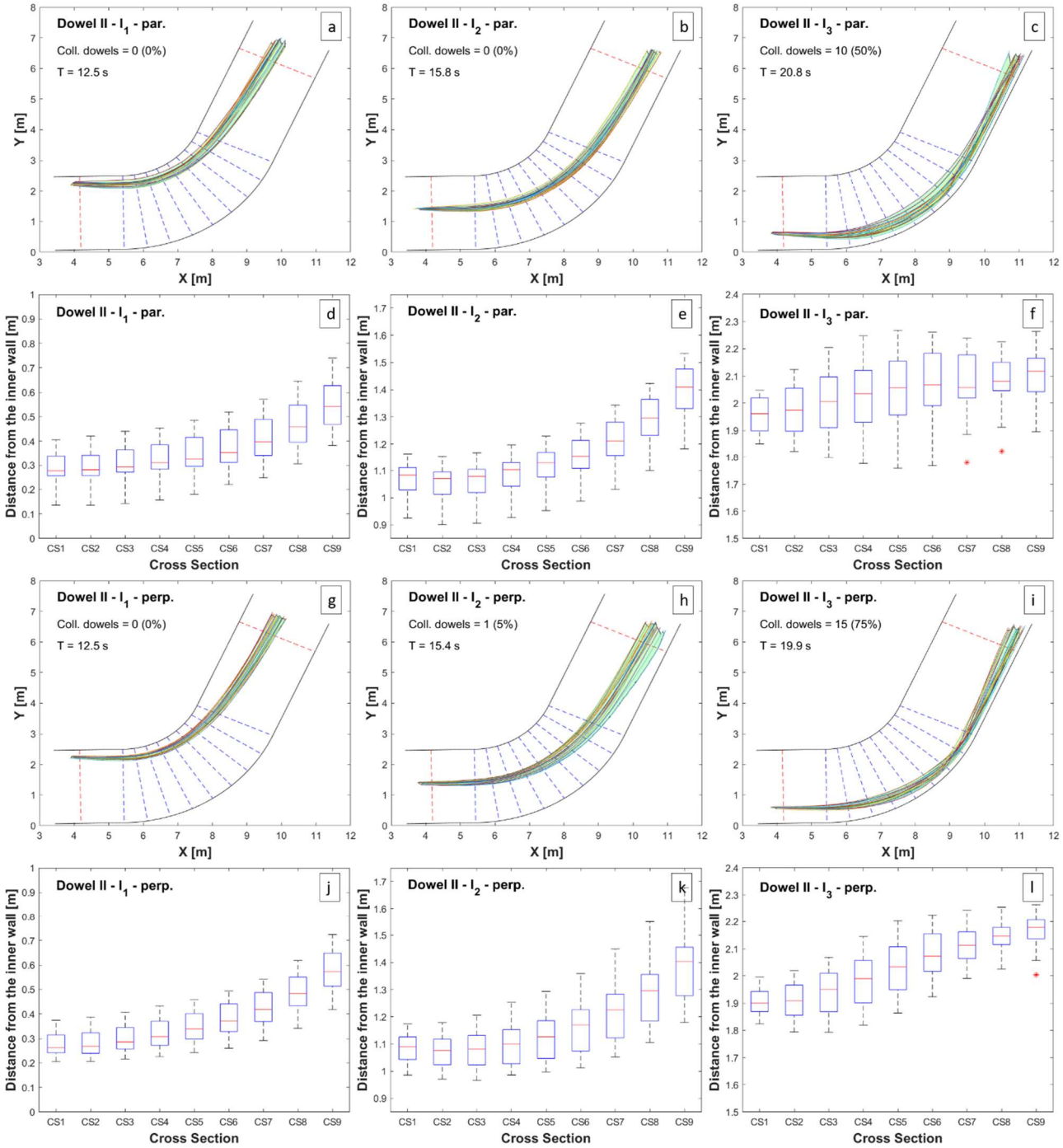

Figure B.2 Trajectories and boxplots of the six experimental configurations for dowel type II.

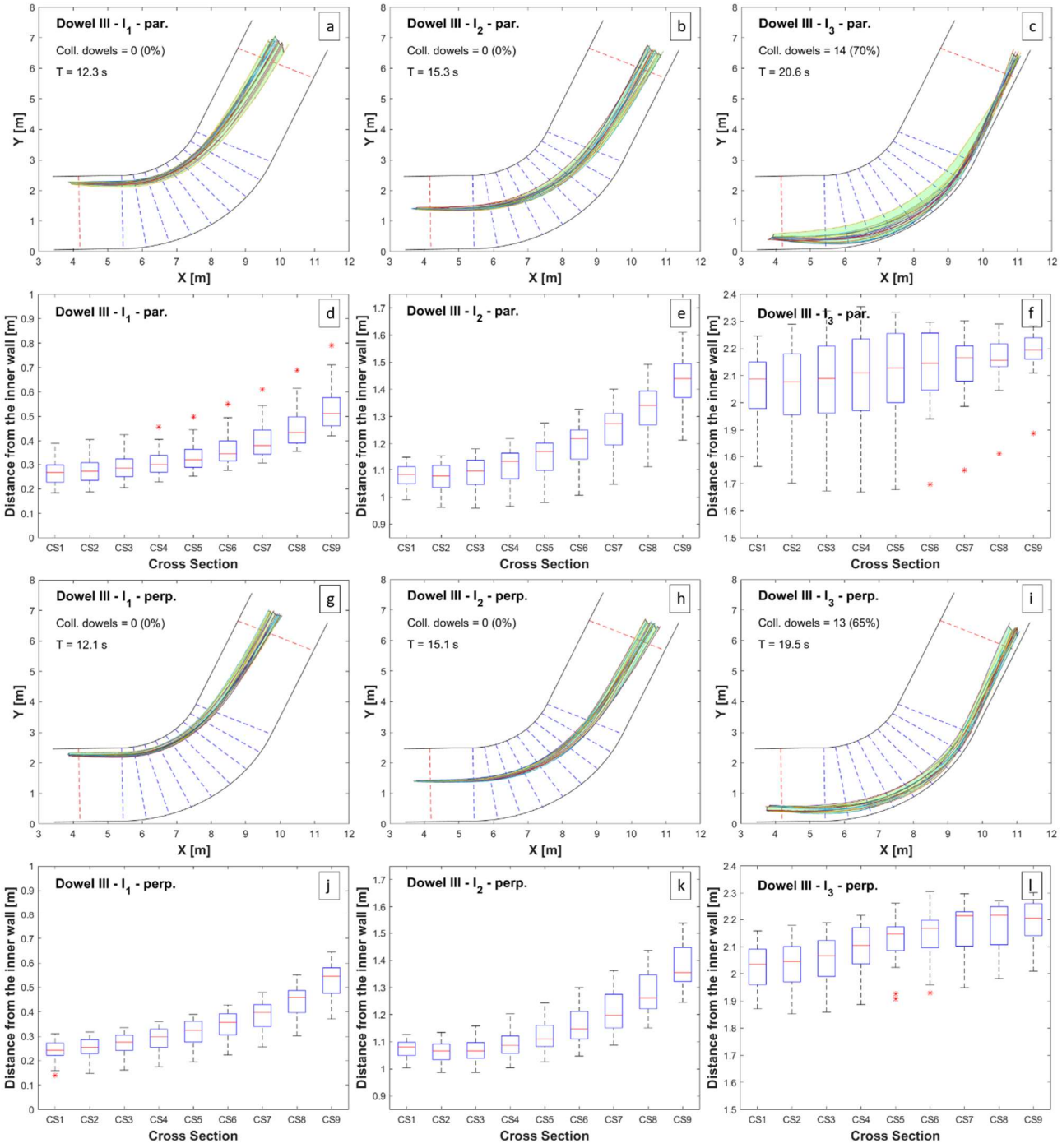

Figure B.3 Trajectories and boxplots of the six experimental configurations for dowel type III.

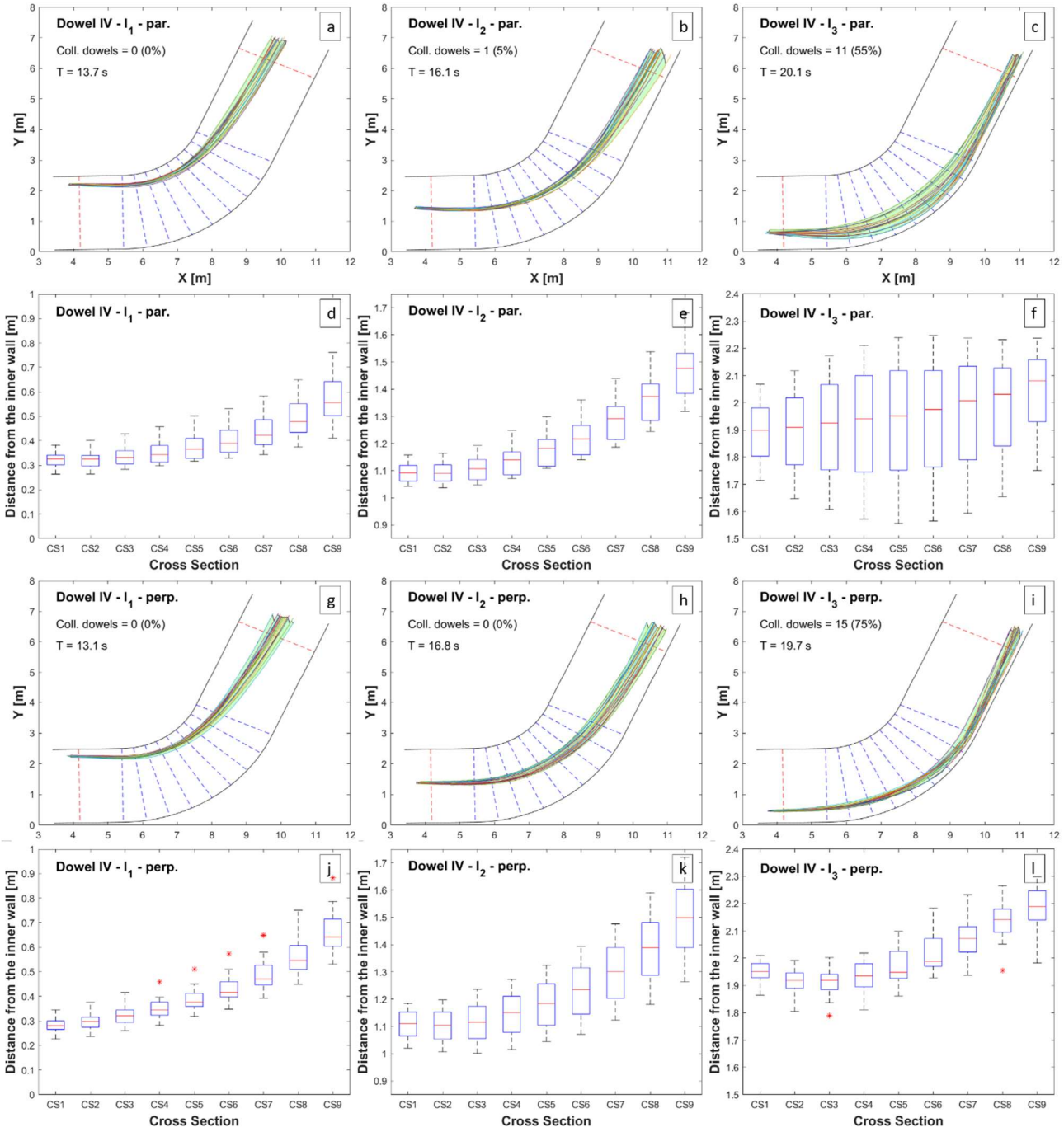

Figure B.4 Trajectories and boxplots of the six experimental configurations for dowel type IV.

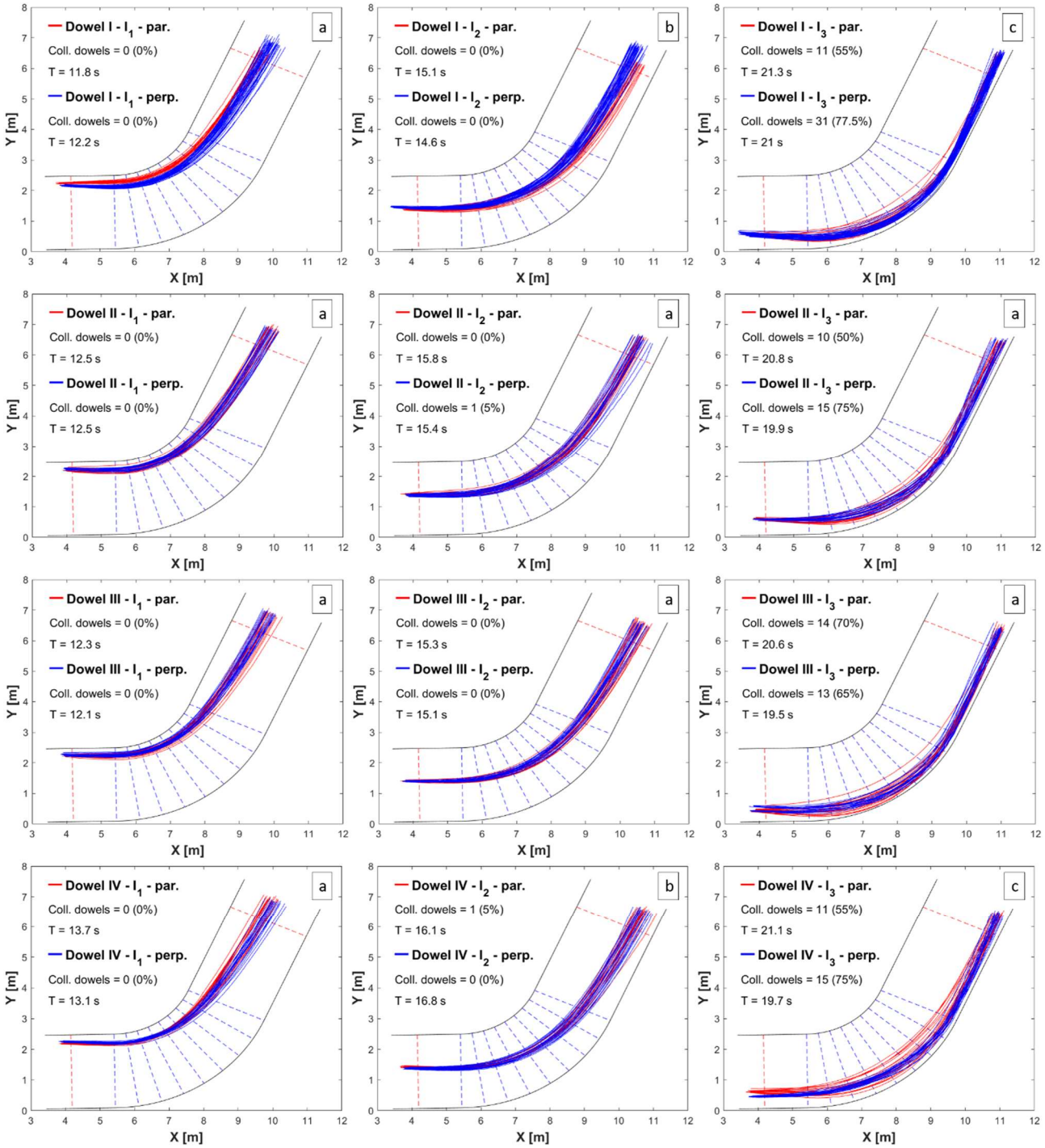

Figure B.5 Trajectories of experiments with all the dowel types. The two considered initial orientations (parallel or perpendicular) of the dowel are reported in each subplot for the three inlet points.

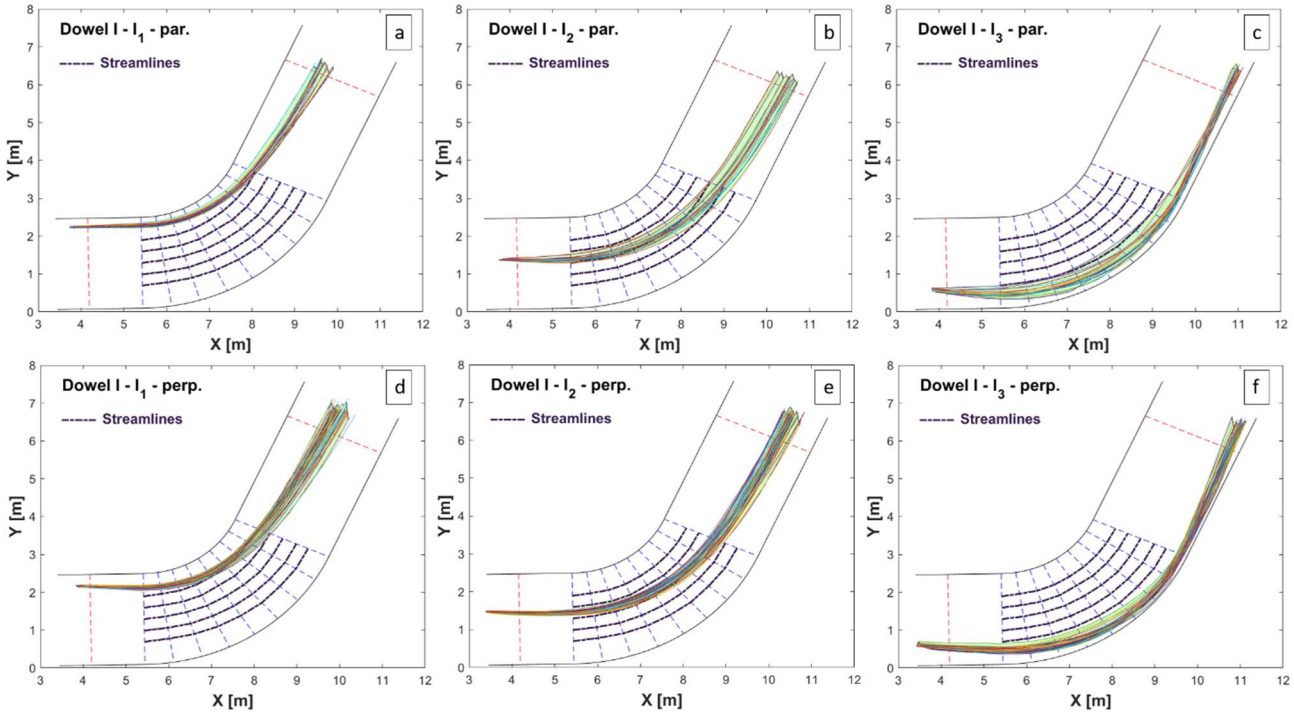

Figure B.6 Comparison between flow streamlines and experimental dowel trajectories for dowel type I.

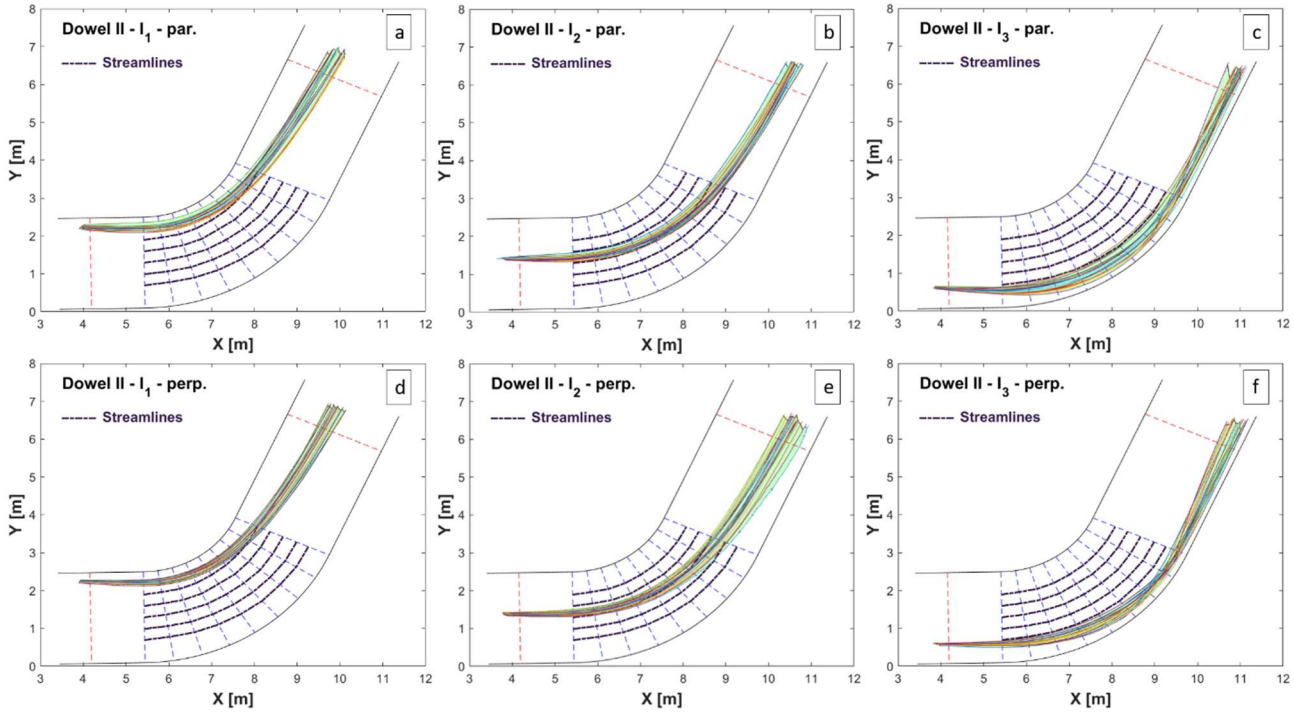

Figure B.7 Comparison between flow streamlines and experimental dowel trajectories for dowel type II.

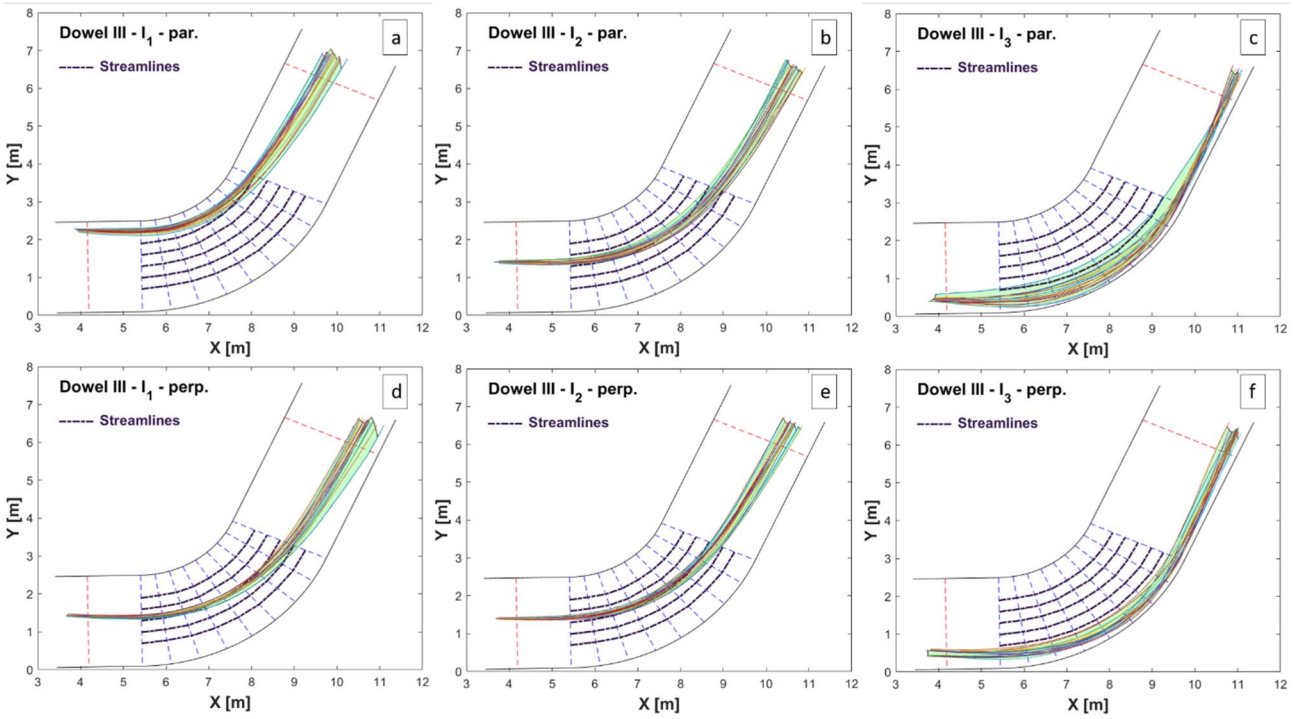

Figure B.8 Comparison between flow streamlines and experimental dowel trajectories for dowel type III.

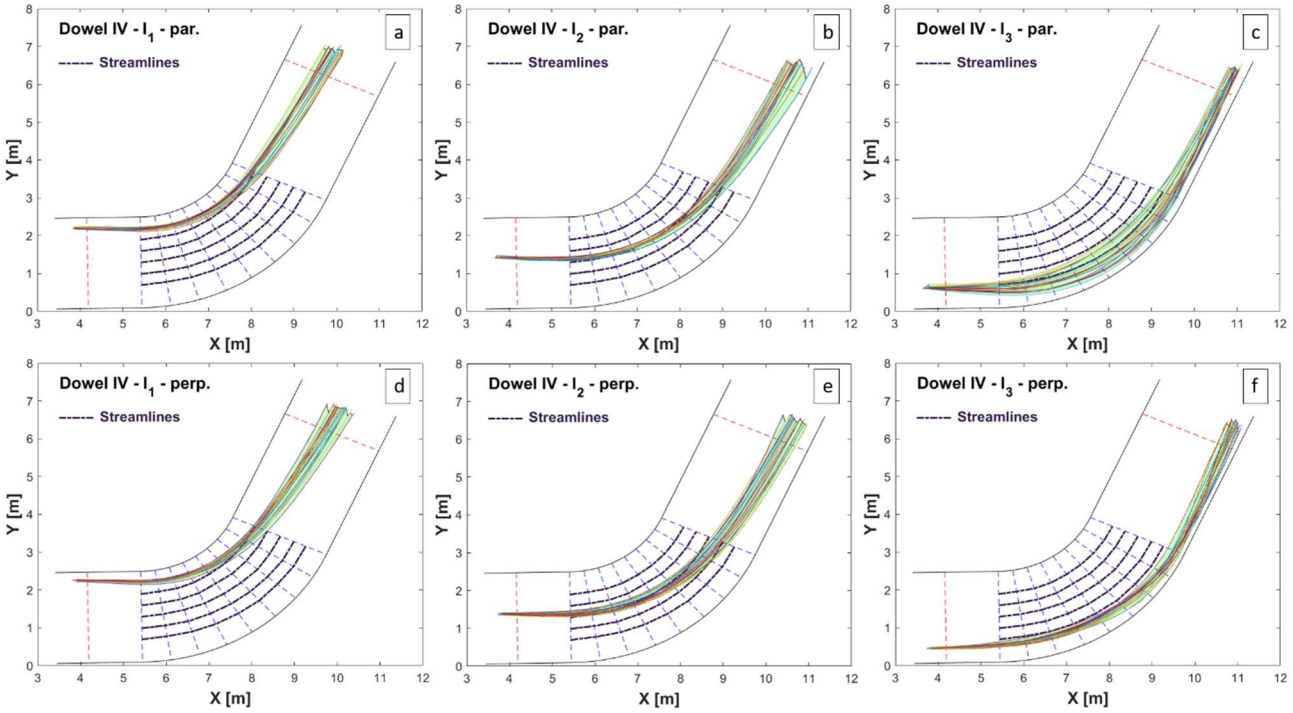

Figure B.9 Comparison between flow streamlines and experimental dowel trajectories for dowel type IV.

C. Iber-Wood: governing equation for wood transport

The two dimensional numerical model for wood transport was developed and proposed by Ruiz-Villanueva et al (2014a) and it was implemented as a new module (Iber-Wood) into the 2D hydrodynamic software Iber (Bladé et al., 2014).

Iber-Wood allows to choose between kinetic and dynamic approaches for modelling the transport of wood pieces. In the present thesis only the kinetic approach was used. All the steps involved in the kinetic analysis are reported in Fig. C.1, the first step is the definition of the dowel velocity that was derived by the balance of the forces acting on a wood in water (see section 2.2). Ruiz-Villanueva et al. (2014a) used the definition of Mazzorana et al. (2011) for defining the dowel velocity:

$$U_{wood} = (1 - C^*) \cdot U_w \quad \text{(C-1)}$$

in which, C^* is the transport inhibition parameter ($C^* = 0$ for dowel in floating condition; $C^* = 1$ for resting condition; $C^* = 1 - (h/D_{wood})$ for sliding or rolling condition).

The authors modified the parameter C^* introducing the relative flow velocity U_r:

$$U_r = U_w - U_{wood} \quad \text{(C-2)}$$

Equation C-2 can be also written as:

$$U_{wood} = U_w - U_{lim} \quad \text{(C-3)}$$

In which, U_{lim} is the threshold velocity for wood incipient motion Mazzorana et al. (2011).

In floating conditions $U_{lim} = 0$ and $U_{wood} = U_w$, it means that the dowel moves with the same velocity of the flow (Haga et al., 2002).

Determined the flow and dowel velocities, the motion of the dowel is modelled at each timestep by:

$$x'^{CM}_{wood} = x^{CM}_{wood} + \Delta t \cdot U^{CM}_{wood} \quad \text{(C-4)}$$

in which, "CM" means center of mass, and x indicates the position.

The velocities at the dowel extremities is defined as:

$$U^1_{wood} = U^{CM}_{wood} + \frac{\partial U_w}{\partial x} \cdot \left(x^1_{wood} - x^{CM}_{wood}\right) \quad \text{(C-5)}$$

$$U^2_{wood} = U^{CM}_{wood} + \frac{\partial U_w}{\partial x} \cdot \left(x^2_{wood} - x^{CM}_{wood}\right) \quad \text{(C-6)}$$

in which, U^{CM}_{wood} is the velocity of the dowel center of mass, and 1 and 2 apexes indicates the two dowel extremities.

Then, the new position of the dowel extremities is calculated as:

$$x'^{1}_{wood} = x^{1}_{wood} + \Delta t \cdot U^{1}_{wood} \quad \text{(C-7)}$$

$$x'^{2}_{wood} = x^{2}_{wood} + \Delta t \cdot U^{2}_{wood} \quad \text{(C-7)}$$

The dowel orientation is determined as:

$$\theta' = \tan^{-1}\left(\frac{x'^{2}_{wood\_t2} - x'^{1}_{wood\_t2}}{x'^{2}_{wood\_t1} - x'^{1}_{wood\_t1}}\right) \quad \text{(C-8)}$$

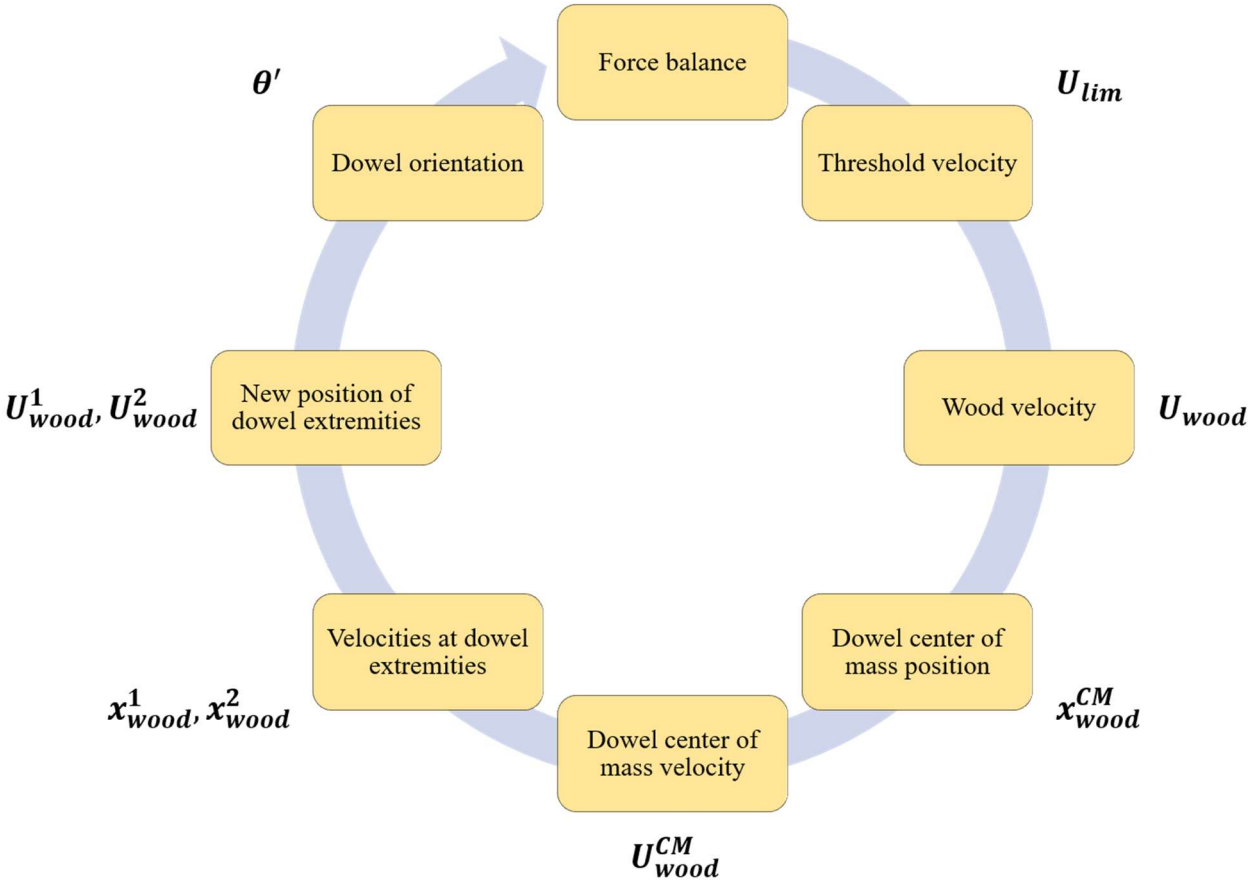

Figure C.1 Scheme of the steps for the kinetic analysis implemented in Iber-Wood.

D. Additional numerical results

Tables D.1 reports the performances of the implemented methods in simulating Leichtweiß Institute laboratory experiments.

Table D.1 Performances of the methods implemented to simulate Leichtweiß Institute experiments. The reported values represent the value of RMSE, RSE, and NSE, for water depth and water surface velocity in simulating the flow at the channel curve. M0 means the model without any correction for secondary current effects, while M1, M2, and M3 refer to the three implemented methods.

RMSE [mm]								
	Water depth				*Water surface velocity*			
CS	M0	M1	M2	M3	M0	M1	M2	M3
1	1.8	0.8	1.7	2.0	38.4	35.7	38.3	39.0
2	-	-	-	-	30.6	30.1	30.9	31.3
3	-	-	-	-	28.1	28.3	28.6	28.8
4	-	-	-	-	26.3	25.9	27.0	26.9
5	2.4	1.1	2.2	2.5	27.1	26.3	27.8	27.3
6	-	-	-	-	27.1	31.4	28.7	27.3
7	-	-	-	-	28.0	33.1	29.5	28.0
8	-	-	-	-	29.4	34.2	30.7	29.9
9	1.6	2.1	1.6	1.6	28.1	28.3	28.6	28.8
RSE [%]								
	Water depth				*Water surface velocity*			
CS	M0	M1	M2	M3	M0	M1	M2	M3
1	1.89	0.85	1.76	2.09	5.61	5.29	5.55	5.74
2	-	-	-	-	4.63	4.44	4.59	4.80
3	-	-	-	-	4.06	3.95	4.02	4.21
4	-	-	-	-	3.83	3.67	3.86	3.94
5	2.36	1.05	2.17	2.42	3.91	3.73	3.95	3.97
6	-	-	-	-	4.02	4.51	4.11	4.02
7	-	-	-	-	3.93	4.51	4.12	3.93
8	-	-	-	-	4.01	4.36	4.22	4.10

9	1.26	2.06	1.36	1.37	3.00	2.78	3.11	3.12

NSE

	Water depth				*Water surface velocity*			
CS	M0	M1	M2	M3	M0	M1	M2	M3
1	0.78	0.95	0.81	0.73	0.15	0.26	0.15	0.12
2	-	-	-	-	0.72	0.73	0.72	0.71
3	-	-	-	-	0.84	0.84	0.84	0.83
4	-	-	-	-	0.88	0.88	0.87	0.88
5	0.94	0.99	0.95	0.94	0.88	0.89	0.87	0.88
6	-	-	-	-	0.86	0.81	0.84	0.86
7	-	-	-	-	0.81	0.73	0.79	0.81
8	-	-	-	-	0.60	0.45	0.56	0.58
9	0.91	0.83	0.91	0.90	-0.24	-0.44	-0.33	-0.31

E. Breach definition in Versilia River model

The breach formation during the simulation was implemented in the model using the specific tool of Iber. This tool allows one to make a mesh deformation in order to reproduce the outflow through the breach.

Table E.1 reports the main characteristics of the breach provided by Paris & Settesoldi (1999). The authors described the breach as a trapezoidal shape with a length of 70 m at the top and 60 m at the bottom. According to the field observation, a trapezoidal shape breach was defined in the model. Figure E.1 shows the schematization of the trapezoidal breach and the parameters needed to reproduce the breach formation during the simulation. Firstly, two points needed to be identified for the definition of the breach line axis (Fig. E.1b), than all the required parameters (Fig. E.1c) were set according to the event reconstruction provided by Paris & Settesoldi (1999). These parameters were: the starting time of the breach, the top and bottom elevations, the top and bottom widths, and the breaching time that defines the time needed for the breach formation; Fig. E.1c shows the parameters used in the model.

Table E.1 Main characteristics of the breach.

Breach shape	trapezoidal
Breaching time	40 min
Top breach length	70 m
Bottom breach length	60 m
Initial levee elevation	17.4 m a.s.l.
Final levee elevation	12.5 m a.s.l.

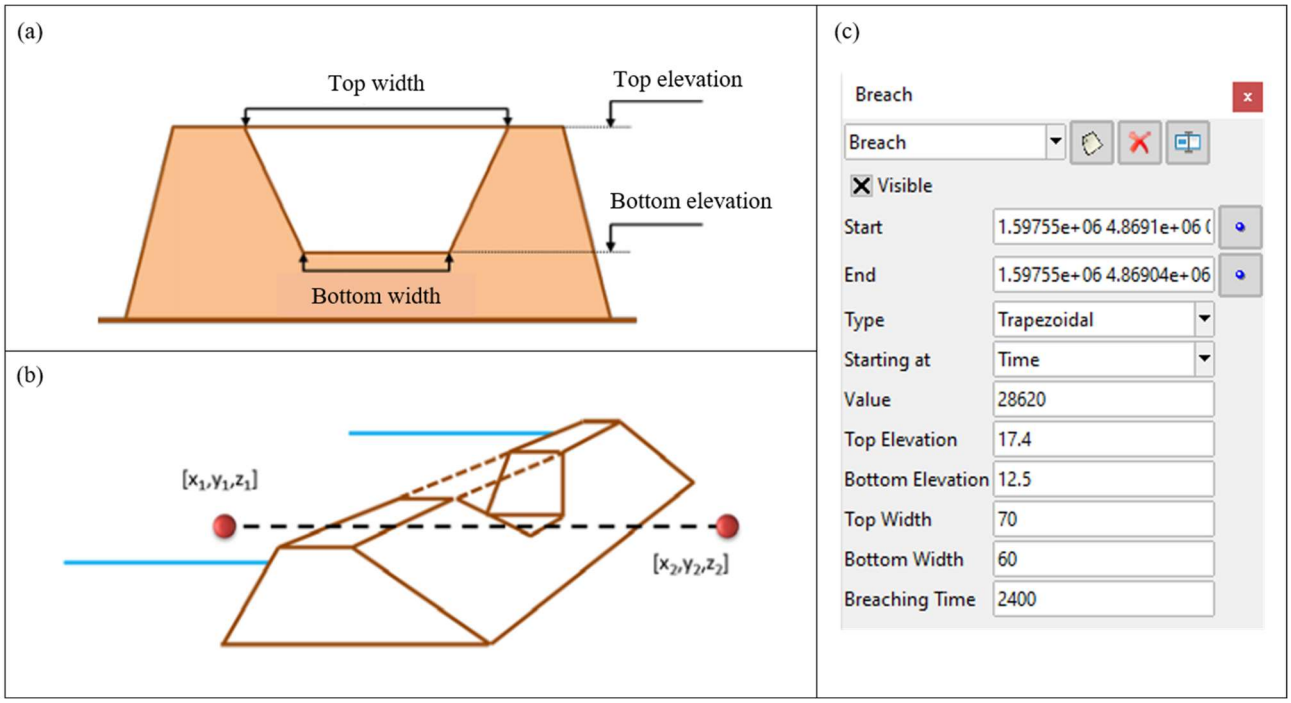

Figure E.1 Breach definition: schematic representation of the breach (a and b) and the breach window with the needed parameters (c). Time values are expressed in seconds while elevations and widths are expressed in meters.